

Measurement of the CKM angle γ using $B_s^0 \rightarrow D_s K \pi\pi$ decays

P. d'Argent¹, E. Gersabeck², M. Kecke¹, M. Schiller³

¹*Physikalisches Institut, Ruprecht-Karls-Universität Heidelberg, Heidelberg, Germany*

²*School of Physics and Astronomy, University of Manchester, Manchester, United Kingdom*

³*School of Physics and Astronomy, University of Glasgow, Glasgow, United Kingdom*

Abstract

We present the first measurement of the weak phase $2\beta + \gamma$ obtained from a time-dependent (amplitude) analysis of $B_s^0 \rightarrow D_s K \pi\pi$ decays using proton-proton collision data corresponding to an integrated luminosity of xxx fb^{-1} recorded by the LHCb detector.

Contents

1	Introduction	1
2	Formalism	2
2.1	Decay rates and CP-observables	2
2.2	Amplitude model	3
2.2.1	Form Factors and Resonance Lineshapes	4
2.2.2	Spin Densities	5
2.3	Validation	8
3	Selection	12
3.1	Cut-based selection	12
3.2	Multivariate stage	13
4	Fits to invariant mass distributions of signal and normalization channel	16
4.1	Signal models for $m(D_s\pi\pi\pi)$ and $m(D_sK\pi\pi)$	16
4.2	Background models for $m(D_s\pi\pi\pi)$	17
4.3	Background models for $m(D_sK\pi\pi)$	17
4.4	Fit to $B_s^0 \rightarrow D_s\pi\pi\pi$ candidates	19
4.5	Fit to $B_s^0 \rightarrow D_sK\pi\pi$ candidates	19
4.6	Extraction of signal weights	19
5	Flavour Tagging	21
5.1	OS tagging calibration	22
5.2	SS tagging calibration	22
5.3	Tagging performance comparison between the signal and normalization channel	22
5.4	Combination of OS and SS taggers	23
6	Acceptance	26
6.1	MC corrections	26
6.1.1	Truth matching of simulated candidates	26
6.1.2	PID efficiencies	27
6.1.3	BDT efficiencies	28
6.1.4	Tracking efficiencies	29
6.2	Decay-time acceptance	30
6.2.1	Comparison of acceptance in subsamples	31
6.2.2	Results	33
6.3	Phasespace acceptance	37
7	Decay-time Resolution	38
7.1	Calibration for Run-I data	39
7.2	Calibration for Run-II data	40
7.3	Cross-checks	43
7.3.1	Kinematic dependence	43
7.3.2	DTF constraints	43

8 Production and Detection Asymmetries	44
8.1 B_s Production Asymmetry	44
8.2 $K^-\pi^+$ Detection Asymmetry	44
9 Time dependent fit	48
9.1 sFit to $B_s^0 \rightarrow D_s\pi\pi\pi$ data	48
9.2 sFit to $B_s^0 \rightarrow D_sK\pi\pi$ data	48
10 Time dependent amplitude fit	50
10.1 Signal Model Construction	50
10.2 Results	51
A Details of multivariate classifier	52
B Detailed mass fits	53
C Decay-time Resolution fits	57
D Spin Amplitudes	61
E Considered Decay Chains	62
F MC corrections	63
G Data distributions	68
G.1 Comparison of signal and calibration channel	68
G.2 Comparison of Run-I and Run-II data	70
G.3 Comparison of D_s final states	72
G.4 Comparison of trigger categories	74
G.5 Comparison of B_s and B_d decays	76
References	77

1 Introduction

- The weak phase γ is the least well known angle of the CKM unitary triangle. A key channel to measure γ is the time-dependent analysis of $B_s^0 \rightarrow D_s K$ decays [1], [2].
 The $B_s^0 \rightarrow D_s K\pi\pi$ proceeds at tree level via the transitions shown in Fig. 1.1 a) and b).

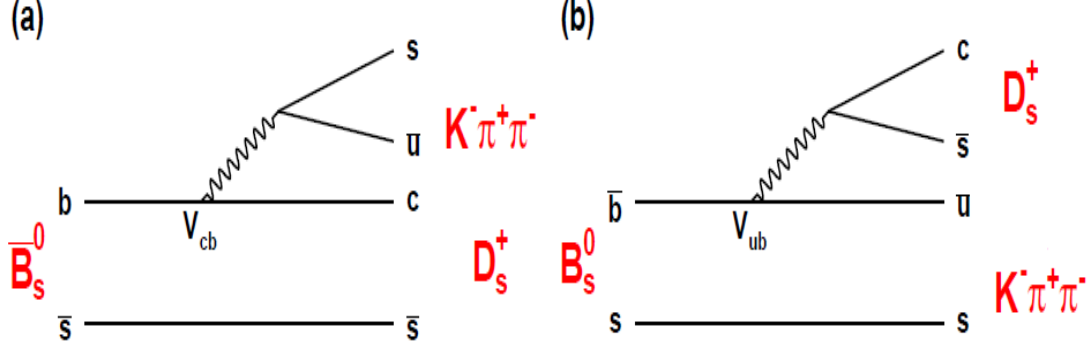


Figure 1.1: Feynman diagram of the $B_s^0 \rightarrow D_s K\pi\pi$ decay, proceeding via a) $b \rightarrow c$ transitions or b) $b \rightarrow u$ transitions.

To measure the weak CKM phase $\gamma \equiv \arg[-(V_{ud}V_{ub}^*)/(V_{cd}V_{cb}^*)]$, a decay with interference between $b \rightarrow c$ and $b \rightarrow u$ transitions at tree level is needed [1]. As illustrated in Fig. 1.1, this is the case for the presented decay mode. A measurement of γ using $B_s^0 \rightarrow D_s K\pi\pi$ decays, where the $K\pi\pi$ subsystem is dominated by excited kaon states such as the $K_1(1270)$ and $K_1(1400)$ resonances, will succeed the branching ratio measurement presented in this note. It is complementary to the above mentioned analysis of $B_s^0 \rightarrow D_s K$, making use of a fully charged final state, where every track is detected in the vertex locator. To account for the non-constant strong phase across the Dalitz plot, one can either develop a time-dependent amplitude model or select a suitable phase-space region and introduce a coherence factor as additional hadronic parameter to the fit.
 This analysis is based on the first observation of the $B_s^0 \rightarrow D_s K\pi\pi$ decay presented in [3] and [4], where its branching ratio is measured relative to $B_s^0 \rightarrow D_s \pi\pi\pi$. The result obtained by the previous analysis is $0.052 \pm 0.005 \pm 0.003$, where the uncertainties are statistical and systematical, respectively. The branching ratio measurement is updated, exploiting the full Run 1 data sample, corresponding to 3 fb^{-1} of integrated luminosity.

20 2 Formalism

21 2.1 Decay rates and CP-observables

22 In the following, we choose a convention in which $\Delta\Gamma_s = \Gamma_L - \Gamma_H < 0$ and $\Delta m_s =$
 23 $m_H - m_L > 0$, where the indices H and L refer to the heavy and light mass eigenstates
 24 of the B_s meson. We assume $|q/p| = 1$ for the complex coefficients p and q which relate
 25 the B_s meson mass eigenstates to the flavour eigenstates.

$$A(B_s^0 \rightarrow D_s^- K^+ \pi\pi) \equiv A(x) = \sum_i a_i A_i(x) \quad (2.1)$$

$$A(B_s^0 \rightarrow D_s^+ K^- \pi\pi) \equiv \bar{A}(\bar{x}) = \sum_i \bar{a}_i \bar{A}_i(\bar{x}) \quad (2.2)$$

$$A(\bar{B}_s^0 \rightarrow D_s^- K^+ \pi\pi) = \bar{A}(x) \text{ (Assuming no direct CPV)} \quad (2.3)$$

$$A(\bar{B}_s^0 \rightarrow D_s^+ K^- \pi\pi) = A(\bar{x}) \text{ (Assuming no direct CPV)} \quad (2.4)$$

26 The full time-dependent amplitude pdf is given by:

$$\begin{aligned} P(x, t, q_t, q_f) \propto & [(|A(x)|^2 + |\bar{A}(x)|^2) \cosh\left(\frac{\Delta\Gamma t}{2}\right) \\ & + q_t q_f (|A(x)|^2 - |\bar{A}(x)|^2) \cos(m_s t) \\ & - 2\text{Re}(A(x)^* \bar{A}(x) e^{-iq_f(\gamma-2\beta_s)}) \sinh\left(\frac{\Delta\Gamma t}{2}\right) \\ & - 2q_t q_f \text{Im}(A(x)^* \bar{A}(x) e^{-iq_f(\gamma-2\beta_s)}) \sin(m_s t)] e^{-\Gamma t} \end{aligned} \quad (2.5)$$

27 where $q_t = +1, -1, 0$ for events tagged as B_s^0 , \bar{B}_s^0 or untagged events and $q_f = +1$ (-1) for
 28 $D_s^- K^+ \pi\pi$ ($D_s^+ K^- \pi\pi$) final states. Integrating over the phasespace, we get

$$\int P(x, t, q_t, q_f) dx \propto [\cosh\left(\frac{\Delta\Gamma t}{2}\right) + q_t q_f C \cos(m_s t) + \kappa D_{q_f} \sinh\left(\frac{\Delta\Gamma t}{2}\right) - q_t \kappa S_{q_f} \sin(m_s t)] e^{-\Gamma t} \quad (2.6)$$

29 where the same convention for the CP coefficients as for the $B_s \rightarrow D_s K$ analysis is used:

$$C = \frac{1 - r^2}{1 + r^2} \quad (2.7)$$

$$D_{q_f} = -\frac{2r \cos(\delta - q_f(\gamma - 2\beta_s))}{1 + r^2} \quad (2.8)$$

$$S_{q_f} = q_f \frac{2r \sin(\delta - q_f(\gamma - 2\beta_s))}{1 + r^2} \quad (2.9)$$

30 The coherence factor κ , the strong phase difference δ and the ratio of the suppressed
 31 ($b \rightarrow u$) over favored ($b \rightarrow c$) decay mode are defined as:

$$\kappa e^{i\delta} \equiv \frac{\int A(x)^* \bar{A}(x) dx}{\sqrt{\int |A(x)|^2 dx} \sqrt{\int |\bar{A}(x)|^2 dx}} \quad (2.10)$$

$$r \equiv \frac{\sqrt{\int |\bar{A}(x)|^2 dx}}{\sqrt{\int |A(x)|^2 dx}}. \quad (2.11)$$

³² In the limit of only one contributing resonance $\kappa \rightarrow 1$.

³³

³⁴ 2.2 Amplitude model

³⁵ The differential decay rate of a B_s meson with mass, m_{B_s} , decaying into four pseudoscalar
³⁶ particles with four-momenta $p_i = (E_i, \vec{p}_i)$ ($i = 1, 2, 3, 4$) is given by

$$d\Gamma = \frac{1}{2m_{B_s}} |A(\mathbf{x})|^2 d\Phi_4, \quad (2.12)$$

³⁷ where the transition amplitude $A(\mathbf{x})$, describes the dynamics of the interaction, $d\Phi_4$
³⁸ is the four-body phase space element [5], and \mathbf{x} represents a unique set of kinematic
³⁹ conditions within the phase space of the decay. Each final state particle contributes three
⁴⁰ observables, manifesting in their three-momentum, summing up to twelve observables in
⁴¹ total. Four of them are redundant due to four-momentum conservation and the overall
⁴² orientation of the system can be integrated out. The remaining five independent degrees
⁴³ of freedom unambiguously determine the kinematics of the decay. Convenient choices
⁴⁴ for the kinematic observables include the invariant mass combinations of the final state
⁴⁵ particles

$$\begin{aligned} m_{ij}^2 &= (p_i + p_j)^2, \\ m_{ijk}^2 &= (p_i + p_j + p_k)^2 \end{aligned} \quad (2.13)$$

⁴⁶ or acoplanarity and helicity angles. It is however important to take into account that,
⁴⁷ while m_{12}^2, m_{23}^2 are sufficient to fully describe a three-body decay, the obvious extension
⁴⁸ to four-body decays with m_{ij}^2, m_{ijk}^2 requires additional care, as these variables alone are
⁴⁹ insufficient to describe the parity-odd moments possible in four-body kinematics.

⁵⁰ In practice, we do not need to choose a particular five-dimensional basis, but use the
⁵¹ full four-vectors of the decay in our analysis. The dimensionality is handled by the phase
⁵² space element which can be written in terms of any set of five independent kinematic
⁵³ observables, $\mathbf{x} = (x_1, \dots, x_5)$, as

$$d\Phi_4 = \phi_4(\mathbf{x}) d^5x, \quad (2.14)$$

⁵⁴ where $\phi_4(\mathbf{x}) = \left| \frac{\partial \Phi_4}{\partial(x_1, \dots, x_5)} \right|$ is the phase space density. In contrast to three-body decays,
⁵⁵ the four-body phase space density function is not flat in the usual kinematic variables.
⁵⁶ Therefore, an analytic expression for ϕ_4 is taken from Ref. [6].

⁵⁷ The total amplitude for the $B_s \rightarrow h_1 h_2 h_3 h_4$ decay is given by the coherent sum
⁵⁸ over all intermediate state amplitudes $A_i(\mathbf{x})$, each weighted by a complex coefficient
⁵⁹ $a_i = |a_i| e^{i\phi_i}$ to be measured from data,

$$A(\mathbf{x}) = \sum_i a_i A_i(\mathbf{x}). \quad (2.15)$$

⁶⁰ To construct $A_i(\mathbf{x})$, the isobar approach is used, which assumes that the decay process
⁶¹ can be factorized into subsequent two-body decay amplitudes [7–9]. This gives rise to
⁶² two different decay topologies; quasi two-body decays $B_s \rightarrow (R_1 \rightarrow h_1 h_2) (R_2 \rightarrow h_3 h_4)$

63 or cascade decays $B_s \rightarrow h_1$ [$R_1 \rightarrow h_2$ ($R_2 \rightarrow h_3 h_4$)]. In either case, the intermediate state
 64 amplitude is parameterized as a product of form factors B_L , included for each vertex
 65 of the decay tree, Breit-Wigner propagators T_R , included for each resonance R , and an
 66 overall angular distribution represented by a spin factor S ,

$$A_i(\mathbf{x}) = B_{L_{B_s}}(\mathbf{x}) [B_{L_{R_1}}(\mathbf{x}) T_{R_1}(\mathbf{x})] [B_{L_{R_2}}(\mathbf{x}) T_{R_2}(\mathbf{x})] S_i(\mathbf{x}). \quad (2.16)$$

67 2.2.1 Form Factors and Resonance Lineshapes

68 To account for the finite size of the decaying resonances, the Blatt-Weisskopf penetration
 69 factors, derived in Ref. [10] by assuming a square well interaction potential with radius
 70 r_{BW} , are used as form factors, B_L . They depend on the breakup momentum q , and the
 71 orbital angular momentum L , between the resonance daughters. Their explicit expressions
 72 are

$$\begin{aligned} B_0(q) &= 1, \\ B_1(q) &= 1/\sqrt{1 + (q r_{\text{BW}})^2}, \\ B_2(q) &= 1/\sqrt{9 + 3(q r_{\text{BW}})^2 + (q r_{\text{BW}})^4}. \end{aligned} \quad (2.17)$$

73 Resonance lineshapes are described as function of the energy-squared, s , by Breit-Wigner
 74 propagators

$$T(s) = \frac{1}{M^2(s) - s - i m_0 \Gamma(s)}, \quad (2.18)$$

75 featuring the energy-dependent mass $M(s)$ (defined below), and total width, $\Gamma(s)$. The
 76 latter is normalized to give the nominal width, Γ_0 , when evaluated at the nominal mass
 77 m_0 , *i.e.* $\Gamma_0 = \Gamma(s = m_0^2)$.

78 For a decay into two stable particles $R \rightarrow AB$, the energy dependence of the decay
 79 width can be described by

$$\Gamma_{R \rightarrow AB}^{(2)}(s) = \Gamma_0 \frac{m_0}{\sqrt{s}} \left(\frac{q}{q_0} \right)^{2L+1} \frac{B_L(q)^2}{B_L(q_0)^2}, \quad (2.19)$$

80 where q_0 is the value of the breakup momentum at the resonance pole [11].

81 The energy-dependent width for a three-body decay $R \rightarrow ABC$, on the other hand, is
 82 considerably more complicated and has no analytic expression in general. However, it can
 83 be obtained numerically by integrating the transition amplitude-squared over the phase
 84 space,

$$\Gamma_{R \rightarrow ABC}^{(3)}(s) = \frac{1}{2\sqrt{s}} \int |A_{R \rightarrow ABC}|^2 d\Phi_3, \quad (2.20)$$

85 and therefore requires knowledge of the resonant substructure. The three-body amplitude
 86 $A_{R \rightarrow ABC}$ can be parameterized similarly to the four-body amplitude in Eq. (2.16). In
 87 particular, it includes form factors and propagators of intermediate two-body resonances.

88 Both Eq. (2.19) and Eq. (2.20) give only the partial width for the decay into a specific
 89 channel. To obtain the total width, a sum over all possible decay channels has to be
 90 performed,

$$\Gamma(s) = \sum_i g_i \Gamma_i(s), \quad (2.21)$$

91 where the coupling strength to channel i , is given by g_i . Branching fractions \mathcal{B}_i are related
 92 to the couplings g_i via the equation [12]

$$\mathcal{B}_i = \int_{s_{min}}^{\infty} \frac{g_i m_0 \Gamma_i(s)}{|M^2(s) - s - i m_0 \sum_j g_j \Gamma_j(s)|^2} ds. \quad (2.22)$$

93 As experimental values are usually only available for the branching fractions, Eq. (2.22)
 94 needs to be inverted to obtain values for the couplings. In practice, this is solved by
 95 minimizing the quantity $\chi^2(g) = \sum_i [\mathcal{B}_i - \mathcal{I}_i(g)]^2 / \Delta \mathcal{B}_i^2$, where $\mathcal{I}_i(g)$ denotes the right-
 96 hand side of Eq. (2.22).

97 The treatment of the lineshape for various resonances considered in this analysis is
 98 described in what follows. The nominal masses and widths of the resonances are taken
 99 from the PDG [12] with the exceptions described below.

100 For the broad scalar resonance σ , the model from Bugg is used [13]. Besides $\sigma \rightarrow \pi\pi$
 101 decays, it includes contributions from the decay modes $\sigma \rightarrow KK$, $\sigma \rightarrow \eta\eta$ and $\sigma \rightarrow \pi\pi\pi\pi$
 102 as well as dispersive effects due to the channel opening of the latter. We use the Gournaris-
 103 Sakurai parametrization for the $\rho(770)^0 \rightarrow \pi\pi$ propagator which provides an analytical
 104 description of the dispersive term, $M^2(s)$ [14]. The energy-dependent width of the $f_0(980)$
 105 resonance is given by the sum of the partial widths into the $\pi\pi$ and KK channels [15],

$$\Gamma_{f_0(980)}(s) = g_{\pi\pi} \Gamma_{f_0(980) \rightarrow \pi\pi}^{(2)}(s) + g_{KK} \Gamma_{f_0(980) \rightarrow KK}^{(2)}(s), \quad (2.23)$$

106 where the coupling constants $g_{\pi\pi}$ and g_{KK} , as well as the mass and width are taken from
 107 a measurement performed by the BES Collaboration [16]. The total decay widths for
 108 both the $f_2(1270)$ and the $f_0(1370)$ meson take the channels $\pi\pi$, KK , $\eta\eta$ and $\pi\pi\pi\pi$ into
 109 account. While the two-body partial widths are described by Eq. (2.19), a model for
 110 the partial width for a decay into four pions is taken from Ref. [17]. The corresponding
 111 branching fractions are taken from the PDG [12]. The nominal mass and width of the
 112 $f_0(1370)$ resonance are taken from an LHCb measurement [18]. Equation (2.19) is used
 113 for all other resonances decaying into a two-body final state.

114 Some particles may not originate from a resonance but are in a state of relative orbital
 115 angular momentum. We denote such non-resonant states by surrounding the particle
 116 system with brackets and indicate the partial wave state with an subscript; for example
 117 $(\pi\pi)_S$ refers to a non-resonant di-pion S -wave. The lineshape for non-resonant states is
 118 set to unity.

119 2.2.2 Spin Densities

120 The spin amplitudes are phenomenological descriptions of decay processes that are required
 121 to be Lorentz invariant, compatible with angular momentum conservation and, where
 122 appropriate, parity conservation. They are constructed in the covariant Zemach (Rarita-
 123 Schwinger) tensor formalism [19–21]. At this point, we briefly introduce the fundamental
 124 objects of the covariant tensor formalism which connect the particle’s four-momenta to
 125 the spin dynamics of the reaction and give a general recipe to calculate the spin factors
 126 for arbitrary decay trees. Further details can be found in Refs. [22, 23].

127 A spin- S particle with four-momentum p , and spin projection λ , is represented by the
 128 polarization tensor $\epsilon_{(S)}(p, \lambda)$, which is symmetric, traceless and orthogonal to p . These
 129 so-called Rarita-Schwinger conditions reduce the a priori 4^S elements of the rank- S tensor

¹³⁰ to $2S + 1$ independent elements in accordance with the number of degrees of freedom of a
¹³¹ spin- S state [20, 24].

¹³² The spin projection operator $P_{(S)}^{\mu_1 \dots \mu_S \nu_1 \dots \nu_S}(p_R)$, for a resonance R , with spin $S =$
¹³³ $\{0, 1, 2\}$, and four-momentum p_R , is given by [23]:

$$\begin{aligned} P_{(0)}^{\mu\nu}(p_R) &= 1 \\ P_{(1)}^{\mu\nu}(p_R) &= -g^{\mu\nu} + \frac{p_R^\mu p_R^\nu}{p_R^2} \\ P_{(2)}^{\mu\nu\alpha\beta}(p_R) &= \frac{1}{2} \left[P_{(1)}^{\mu\alpha}(p_R) P_{(1)}^{\nu\beta}(p_R) + P_{(1)}^{\mu\beta}(p_R) P_{(1)}^{\nu\alpha}(p_R) \right] - \frac{1}{3} P_{(1)}^{\mu\nu}(p_R) P_{(1)}^{\alpha\beta}(p_R), \end{aligned} \quad (2.24)$$

¹³⁴ where $g^{\mu\nu}$ is the Minkowski metric. Contracted with an arbitrary tensor, the projection
¹³⁵ operator selects the part of the tensor which satisfies the Rarita-Schwinger conditions.

¹³⁶ For a decay process $R \rightarrow AB$, with relative orbital angular momentum L , between
¹³⁷ particle A and B , the angular momentum tensor is obtained by projecting the rank- L
¹³⁸ tensor $q_R^{\nu_1} q_R^{\nu_2} \dots q_R^{\nu_L}$, constructed from the relative momenta $q_R = p_A - p_B$, onto the spin- L
¹³⁹ subspace,

$$L_{(L)\mu_1 \dots \mu_L}(p_R, q_R) = (-1)^L P_{(L)\mu_1 \dots \mu_L \nu_1 \dots \nu_L}(p_R) q_R^{\nu_1} \dots q_R^{\nu_L}. \quad (2.25)$$

¹⁴⁰ Their $|\vec{q}_R|^L$ dependence accounts for the influence of the centrifugal barrier on the transition
¹⁴¹ amplitudes. For the sake of brevity, the following notation is introduced,

$$\begin{aligned} \varepsilon_{(S)}(R) &\equiv \varepsilon_{(S)}(p_R, \lambda_R), \\ P_{(S)}(R) &\equiv P_{(S)}(p_R), \\ L_{(L)}(R) &\equiv L_{(L)}(p_R, q_R). \end{aligned} \quad (2.26)$$

¹⁴² Following the isobar approach, a four-body decay amplitude is described as a product
¹⁴³ of two-body decay amplitudes. Each sequential two-body decay $R \rightarrow A B$, with relative
¹⁴⁴ orbital angular momentum L_{AB} , and total intrinsic spin S_{AB} , contributes a term to the
¹⁴⁵ overall spin factor given by

$$\begin{aligned} S_{R \rightarrow AB}(\mathbf{x}|L_{AB}, S_{AB}; \lambda_R, \lambda_A, \lambda_B) &= \varepsilon_{(S_R)}(R) X(S_R, L_{AB}, S_{AB}) L_{(L_{AB})}(R) \\ &\times \Phi(\mathbf{x}|S_{AB}; \lambda_A, \lambda_B), \end{aligned} \quad (2.27)$$

¹⁴⁶ where

$$\Phi(\mathbf{x}|S_{AB}; \lambda_A, \lambda_B) = P_{(S_{AB})}(R) X(S_{AB}, S_A, S_B) \varepsilon_{(S_A)}^*(A) \varepsilon_{(S_B)}^*(B). \quad (2.28)$$

¹⁴⁷ Here, a polarization vector is assigned to the decaying particle and the complex conjugate
¹⁴⁸ vectors for each decay product. The spin and orbital angular momentum couplings are
¹⁴⁹ described by the tensors $P_{(S_{AB})}(R)$ and $L_{(L_{AB})}(R)$, respectively. Firstly, the two spins S_A
¹⁵⁰ and S_B , are coupled to a total spin- S_{AB} state, $\Phi(\mathbf{x}|S_{AB})$, by projecting the corresponding
¹⁵¹ polarization vectors onto the spin- S_{AB} subspace transverse to the momentum of the
¹⁵² decaying particle. Afterwards, the spin and orbital angular momentum tensors are
¹⁵³ properly contracted with the polarization vector of the decaying particle to give a Lorentz
¹⁵⁴ scalar. This requires in some cases to include the tensor $\varepsilon_{\alpha\beta\gamma\delta} p_R^\delta$ via

$$X(j_a, j_b, j_c) = \begin{cases} 1 & \text{if } j_a + j_b + j_c \text{ even} \\ \varepsilon_{\alpha\beta\gamma\delta} p_R^\delta & \text{if } j_a + j_b + j_c \text{ odd} \end{cases}, \quad (2.29)$$

155 where $\varepsilon_{\alpha\beta\gamma\delta}$ is the Levi-Civita symbol and j refers to the arguments of X defined in
 156 Eqs. 2.27 and 2.28. Its antisymmetric nature ensures the correct parity transformation
 157 behavior of the amplitude. The spin factor for a whole decay chain, for example $R \rightarrow$
 158 $(R_1 \rightarrow AB)(R_2 \rightarrow CD)$, is obtained by combining the two-body terms and performing a
 159 sum over all unobservable, intermediary spin projections

$$\sum_{\lambda_{R_1}, \lambda_{R_2}} S_{R \rightarrow R_1 R_2}(\mathbf{x}|L_{R_1 R_2}; \lambda_{R_1}, \lambda_{R_2}) S_{R_1 \rightarrow AB}(\mathbf{x}|L_{AB}; \lambda_{R_1}) S_{R_2 \rightarrow CD}(\mathbf{x}|L_{CD}; \lambda_{R_2}), \quad (2.30)$$

160 where $\lambda_R = \lambda_A = \lambda_B = \lambda_C = \lambda_D = 0$, $S_{AB} = S_{CD} = 0$ and $S_{R_1 R_2} = L_{R_1 R_2}$, as only
 161 pseudoscalar initial/final states are involved.

162 The spin factors for all decay topologies considered in this analysis are explicitly given
 163 in Appendix D.

164 2.3 Validation

165 The amplitude fit is performed by using the amplitude analysis tool **MINT2**. It was
 166 previously applied to analyze $D^0 \rightarrow 4\pi$ and $D^0 \rightarrow KK\pi\pi$ decays [25] which have an
 167 identical general spin structure (*i.e.* scalar to four scalar decay) then $B_s \rightarrow D_s K\pi\pi$ decays.
 168 In the course of the $D^0 \rightarrow hhhh$ analysis, the implementation of the amplitudes were
 169 extensively cross-checked against other available tool such as **qft++** [26], **AmpGen** [27] and
 170 were possible **EVTGEN** [28]. Since no additional line shapes or spin factors are needed for
 171 this analysis, we consider the amplitude calculation as fully validated.

172 This does, however, not apply to the full time-dependent amplitude pdf which is newly
 173 implemented for this analysis. To cross-check it, we use **EVTGEN** to generate toy events
 174 with time-dependent CP violation according to the **SSD_CP** event model [28]. Since this
 175 event model does not allow for multiple interfering resonances, we generate only the decay
 176 chain $B_s \rightarrow D_s (K_1(1400) \rightarrow K^*(892)\pi)$. Table 2.1 lists the generated input parameters.
 177 The toy data set is fitted with our **MINT2** implementation of the full time-dependent
 178 amplitude pdf and the phasespace-integrated pdf.

179 The CP coefficients $C, D, \bar{D}, S, \bar{S}$ are the fit parameters in case of the phasespace-
 180 integrated pdf, while the full pdf determines $x_{\pm} = r \cos(\delta \pm (\gamma - 2\beta_s))$ and $y_{\pm} = r \sin(\delta \pm$
 181 $(\gamma - 2\beta_s))$. The fit parameters are converted to the physical observables $r, \kappa, \delta, \gamma$ using
 182 the **GammaCombo** package [29]. As shown in Tab. 2.2, 2.3 and 2.4, the fit results are
 183 in excellent agreement with the generated input values. The 1-CL contours are shown
 184 in Figs. 2.1 and 2.2. The phasespace-integrated fit is, in addition, performed with the
 185 **B2DX** fitter used for the $B_s \rightarrow D_s K$ analysis yielding identical results. Note though that
 186 some parts of the **B2DX** fitter have been taken over to our **MINT2** fitter, such that the
 187 implementations are not fully independent.

Table 2.1: Input values used to generate **EVTGEN** toy events according to the **SSD_CP** event model.

τ	1.5 ps
$\Delta\Gamma$	-0.1 ps^{-1}
Δm_s	17.757 ps^{-1}
r	0.37
κ	1
δ	10.0°
γ	71.1°
β_s	0.0°

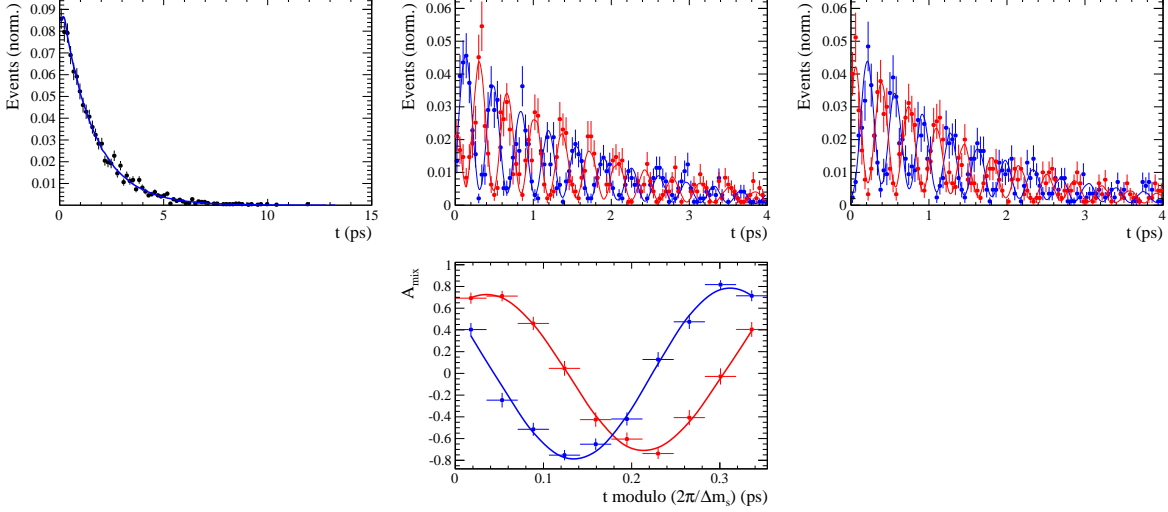


Figure 2.1: Time distribution of $B_s \rightarrow D_s K \pi\pi$ events generated with EVTGEN (points with error bars) and MINT2 fit projections (blue solid line).

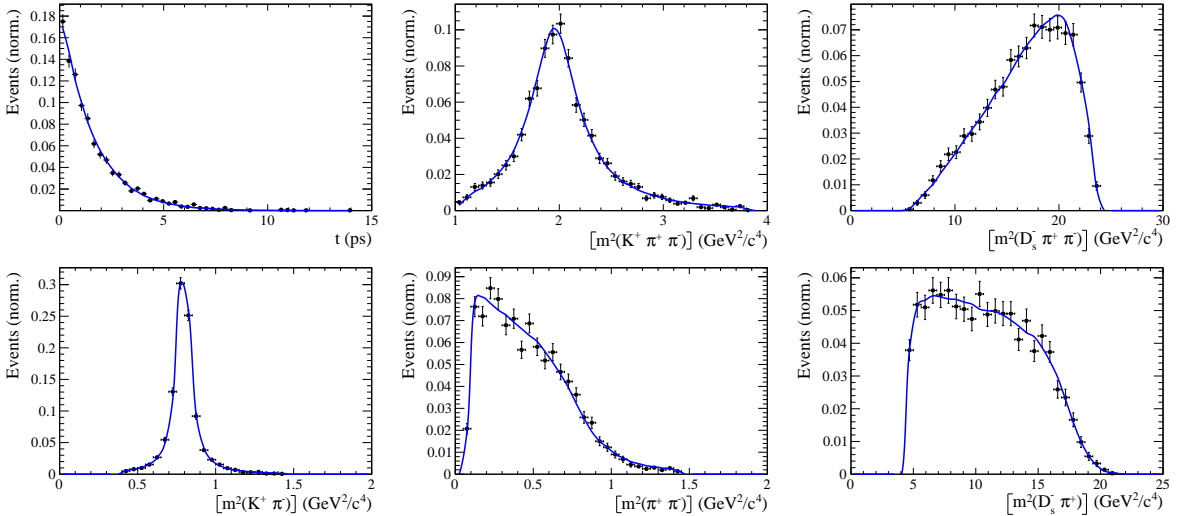


Figure 2.2: Time and invariant mass distributions of $B_s \rightarrow D_s K \pi\pi$ events generated with EVTGEN (points with error bars) and MINT2 fit projections (blue solid line).

Table 2.2: Result of the phasespace-integrated fit to EVTGEN toy events.

	Generated	Fit result	Pull(σ)
C	0.759	0.763 ± 0.026	0.2
D	-0.314	-0.376 ± 0.227	-0.3
\bar{D}	-0.101	-0.261 ± 0.246	-0.7
S	-0.570	-0.626 ± 0.035	1.6
\bar{S}	-0.643	-0.669 ± 0.035	-0.7

Table 2.3: Result of the time-dependent amplitude fit to EVTGEN toy events.

	Generated	Fit result	Pull(σ)
x_-	0.179	0.135 ± 0.050	-0.9
y_-	-0.324	-0.307 ± 0.022	0.8
x_+	0.057	0.102 ± 0.065	0.6
y_+	0.366	0.394 ± 0.023	1.3

Table 2.4: Results for the physical observables obtained from fits to EVTGEN toy events.

	Generated	Full PDF	Phasespace integrated
r	0.370	0.379 ± 0.021	0.379 ± 0.017
κ	1.0	1.0	1.000 ± 0.059
δ	10.0°	9.0 ± 5.1	5.9 ± 6.0
γ	71.1°	67.3 ± 5.9	75.1 ± 6.9

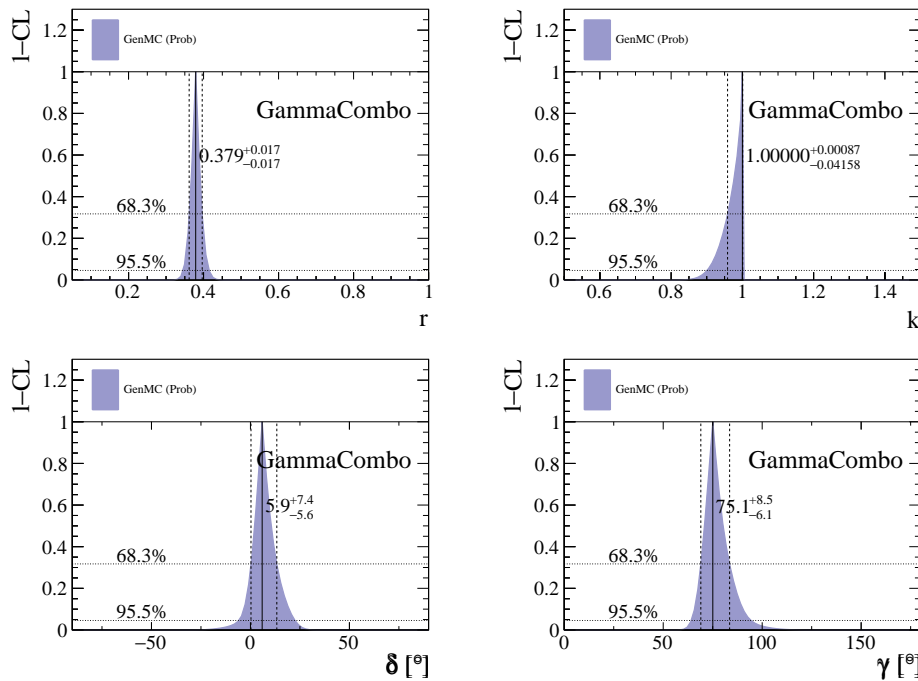


Figure 2.3: The 1-CL contours for the physical observable $r, \kappa, \delta, \gamma$ obtained with the phasespace integrated fit to the EVTGEN toy sample.

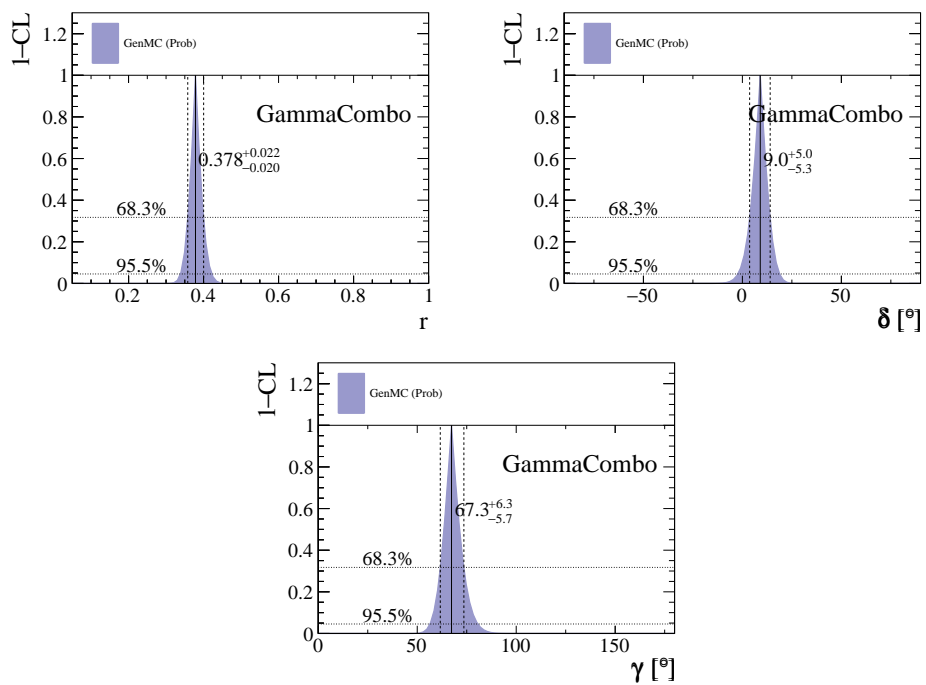


Figure 2.4: The 1-CL contours for the physical observable r, δ, γ obtained with the time-dependent amplitude fit fit to the **EVTGEN** toy sample.

188 **3 Selection**

189 For the presented analysis, we reconstruct the $B_s^0 \rightarrow D_s K\pi\pi$ decay through two different
190 final states of the D_s meson, $D_s \rightarrow KK\pi$ and $D_s \rightarrow \pi\pi\pi$. Of those two final states
191 $D_s \rightarrow KK\pi$ is the most prominent one, while $\mathcal{BR}(D_s \rightarrow \pi\pi\pi) \approx 0.2 \cdot \mathcal{BR}(D_s \rightarrow KK\pi)$
192 holds for the other one.

193 A two-fold approach is used to isolate the $B_s^0 \rightarrow D_s K\pi\pi$ candidates from data passing
194 the stripping line. First, further one-dimensional cuts are applied to reduce the level of
195 combinatorial background and to veto some specific physical background. This stage is
196 specific to the respective final state in which the D_s meson is reconstructed, since different
197 physical backgrounds, depending on the respective final state, have to be taken into
198 account. After that, a multivariate classifier is trained which combines the information
199 of several input variables, including their correlation, into one powerful discriminator
200 between signal and combinatorial background. For this stage, all possible D_s final states
201 are treated equally.

202 **3.1 Cut-based selection**

203 In order to minimize the contribution of combinatorial background to our samples, we
204 apply the following cuts to the b hadron:

- 205 • DIRA > 0.99994
- 206 • min IP $\chi^2 < 20$ to any PV,
- 207 • FD $\chi^2 > 100$ to any PV,
- 208 • Vertex $\chi^2/\text{nDoF} < 8$,
- 209 • $(Z_{D_s} - Z_{B_s^0}) > 0$, where Z_M is the z-component of the position \vec{x} of the decay vertex
210 for the B_s^0/D_s meson.

211 Additionally, we veto various physical backgrounds, which have either the same final
212 state as our signal decay, or can contribute via a single misidentification of $K \rightarrow \pi$ or
213 $K \rightarrow p$. In the following, the vetoes are ordered by the reconstructed D_s final state they
214 apply to:

215 1. All:

- 216 (a) $B_s^0 \rightarrow D_s^+ D_s^- : |M(K\pi\pi) - m_{D_s}| > 20 \text{ MeV}/c^2$.
- 217 (b) $B_s^0 \rightarrow D_s^- K^+ K^- \pi^+ : \text{possible with single missID of } K^- \rightarrow \pi^-$, rejected by
218 requiring π^- to fulfill $\text{DLL}_{K\pi} < 5$.

219 2. $D_s \rightarrow KK\pi$

- 220 (a) $B^0 \rightarrow D^+(\rightarrow K^+\pi^-\pi^+) K\pi\pi : \text{possible with single missID of } \pi^+ \rightarrow K^+$, vetoed
221 by changing particle hypothesis and recompute $|M(K^+\pi^-\pi^+) - m_{D_p}| > 30$
222 MeV/ c^2 , or the K^+ has to fulfill $\text{DLL}_{K\pi} > 10$.

- 223 (b) $\Lambda_b^0 \rightarrow \Lambda_c^+ (\rightarrow p K^- \pi^+) K \pi \pi$: possible with single missID of $p \rightarrow K^+$, vetoed by
 224 changing particle hypothesis and recompute $M(p K^- \pi^+) - m_{\Lambda_c^+} > 30 \text{ MeV}/c^2$,
 225 or the K^+ has to fulfill $(\text{DLL}_{K\pi} - \text{DLL}_{p\pi}) > 5$.
 226 (c) $D^0 \rightarrow KK$: D^0 combined with a random π can fake a $D_s \rightarrow KK\pi$ decay and
 227 be a background to our signal, vetoed by requiring $M(KK) < 1840 \text{ MeV}/c^2$.

228 3. $D_s \rightarrow \pi\pi\pi$

- 229 (a) $D^0 \rightarrow \pi\pi$: combined with a random π can fake a $D_s \rightarrow \pi\pi\pi$ decay and be a
 230 background to our signal, vetoed by requiring both possible combinations to
 231 have $M(\pi\pi) < 1700 \text{ MeV}/c^2$.

232 The most prominent final state used in this analysis is $B_s^0 \rightarrow D_s (\rightarrow KK\pi) K \pi \pi$, where
 233 the D_s decay can either proceed via the narrow ϕ resonance, the broader K^{*0} resonance, or
 234 non resonant. Depending on the decay process being resonant or not, we apply additional
 235 PID requirements on this final state:

- 236 • resonant case:
 - 237 – $D_s^+ \rightarrow \phi \pi^+$, with $|M(K^+ K^-) - m_\phi| < 20 \text{ MeV}/c^2$: no additional requirements,
 238 since ϕ is narrow and almost pure $K^+ K^-$.
 - 239 – $D_s^+ \rightarrow \bar{K}^{*0} K^+$, with $|M(K^- \pi^+) - m_{K^{*0}}| < 75 \text{ MeV}/c^2$: $\text{DLL}_{K\pi} > 0$ for kaons,
 240 since this resonance is more than ten times broader than ϕ .
- 241 • non resonant case: $\text{DLL}_{K\pi} > 5$ for kaons, since the non resonant category has
 242 significant charmless contributions.

243 For the $D_s \rightarrow \pi\pi\pi$ final state, we apply global PID requirements:

- 244 • $\text{DLL}_{K\pi} < 10$ for all pions.
- 245 • $\text{DLL}_{p\pi} < 10$ for all pions.

246 3.2 Multivariate stage

247 We use TMVA [30] to train a multivariate discriminator, which is used to further improve
 248 the signal to background ratio. The following variables are used for the training:

- 249 • $\max(\text{ghostProb})$ over all tracks
- 250 • $\text{cone}(p_T)$ asymmetry of every track, which is defined to be the difference between the
 251 p_T of the π/K and the sum of all other p_T in a cone of radius $r = \sqrt{(\Delta\Phi)^2 + (\Delta\eta)^2}$
 252 $< 1 \text{ rad}$ around the signal π/K track.
- 253 • $\min(\text{IP}\chi^2)$ over the X_s daughters
- 254 • $\max(\text{DOCA})$ over all pairs of X_s daughters
- 255 • $\min(\text{IP}\chi^2)$ over the D_s daughters

- 256 • D_s and B_s^0 DIRA
 257 • D_s FD significance
 258 • $\max(\cos(D_s h_i))$, where $\cos(D_s h_i)$ is the cosine of the angle between the D_s and
 259 another track i in the plane transverse to the beam
 260 • B_s^0 IP χ^2 , FD χ^2 and Vertex χ^2

261 Various classifiers were investigated in order to select the best performing discriminator.
 262 Consequently, a boosted decision tree with gradient boost (BDTG) is chosen as nominal
 263 classifier. We use truth-matched MC as signal input. Simulated signal candidates are
 264 required to pass the same trigger, stripping and preselection requirements, that were
 265 used to select the data samples. For the background we use events from the high mass
 266 sideband ($m_{B_s^0 \text{candidate}} > 5600 \text{ MeV}/c^2$) of our data samples. As shown in Fig. 3.1,
 267 this mass region is sufficiently far away from signal structures and is expected to be
 268 dominantly composed of combinatorial background. For completeness, the mass distribu-
 269 tion of preselected $D_s \rightarrow hh$ candidates (where $h = \pi$ or $h = K$) is also shown in Fig. 3.1.

270

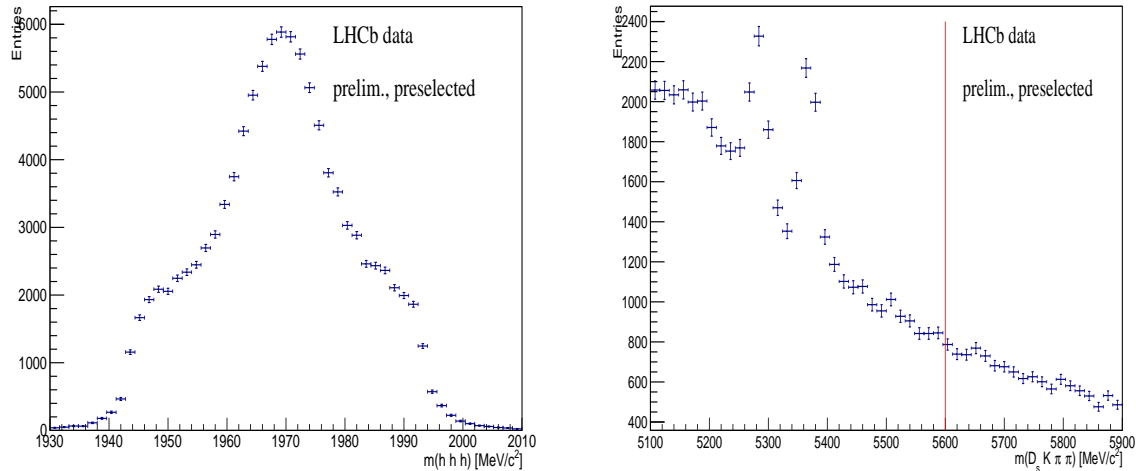


Figure 3.1: Invariant mass distribution of preselected (left) $D_s \rightarrow hhh$ and (right) $B_s^0 \rightarrow D_s K\pi\pi$ candidates. For the $B_s^0 \rightarrow D_s K\pi\pi$ candidates, the region right from the red colored line with $m_{B_s^0 \text{candidate}} > 5600 \text{ MeV}/c^2$ is used as background input for the boosted decision tree.

271 The distributions of the input variables for signal and background and the BDTG
 272 output distribution are shown in the appendix.

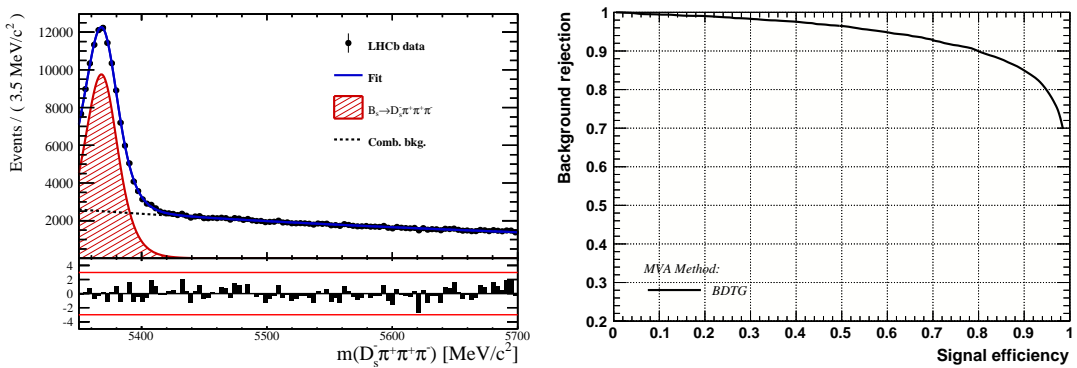


Figure 3.2

273 **4 Fits to invariant mass distributions of signal and**
 274 **normalization channel**

275 In order to properly model the invariant mass distribution of $B_s^0 \rightarrow D_s K\pi\pi$ and $B_s^0 \rightarrow$
 276 $D_s \pi\pi\pi$ candidates, the expected signal shape, as well as the expected shape for the
 277 combinatorial and physical background has to be known. This model can then be used to
 278 fit the distributions and obtain signal sWeights [31], which are employed to suppress the
 279 residual background that is still left in the sample, for the time-dependent amplitude fit.

280 **4.1 Signal models for $m(D_s \pi\pi\pi)$ and $m(D_s K\pi\pi)$**

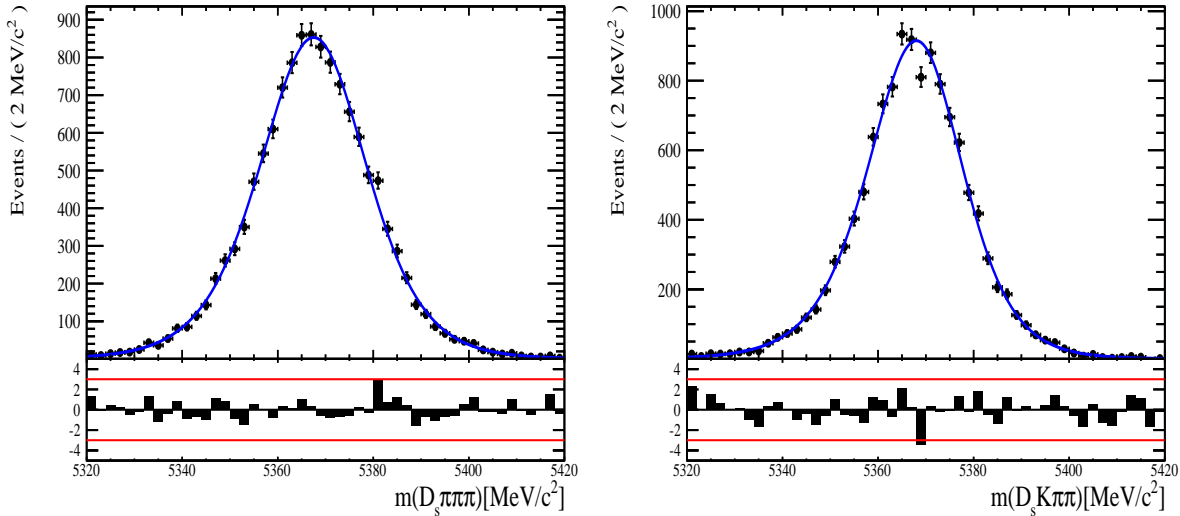


Figure 4.1: Invariant mass distributions of simulated (left) $B_s^0 \rightarrow D_s \pi\pi\pi$ and (right) $B_s^0 \rightarrow D_s K\pi\pi$ events. A fit of a RooJohnsonSU function to each distribution is overlaid.

281 The mass distribution of $B_s^0 \rightarrow D_s K\pi\pi$ signals is modeled using a Johnson SU
 282 function [32], which is a gaussian function with a Landau-like tail on one side,

$$J(m_{B_s^0}; \mu, \sigma, \gamma, \delta) = \frac{\delta}{\sigma 2\pi \sqrt{1 + (\frac{m_{B_s^0} - \mu}{\sigma})^2}} \exp\left(-\frac{1}{2}[\gamma + \delta \operatorname{Argsh}(\frac{m_{B_s^0} - \mu}{\sigma})]^2\right). \quad (4.1)$$

283 The sign of γ in Eq. 4.1 determines whether the tail is located at lower ($\gamma > 0$)
 284 or higher ($\gamma < 0$) invariant mass values than the mean μ of the gaussian function and
 285 δ describes the (a)symmetry of the fitted distribution. Higher values of δ result in a
 286 more symmetric, gaussian-like function. Another Johnson SU function function is used
 287 to account for the contribution of the $B^0 \rightarrow D_s K\pi\pi$ decay, which is also present in
 288 the $m(D_s K\pi\pi)$ spectrum. The width, as well as the tail parameters are fixed to values
 289 obtained by a fit to the invariant mass distribution of simulated events shown in Fig 4.1.
 290 A linear scaling factor for the mean μ and width σ is floated in the fit to account for
 291 possible differences between the simulation and real data.

292 The same approach is used to describe the invariant mass distribution of $B_s^0 \rightarrow D_s \pi\pi\pi$

293 candidates. A Johnson SU function is used to model the signal, the parameters are
294 determined by a fit to the invariant mass of simulated $B_s^0 \rightarrow D_s\pi\pi\pi$ decays, shown in
295 Fig 4.1. A scale factor for the width and the mean is floated to account for differences
296 between data and MC.

297 4.2 Background models for $m(D_s\pi\pi\pi)$

298 Different background sources arise in the invariant mass spectrum of candidates in the
299 normalization mode.

300 The following backgrounds have to be accounted for:

- 301 • Combinatorial background: This contribution arises from either a real D_s , which is
302 paired with random tracks to form the B_s^0 candidates, or via real X_d 's, which are
303 combined with three tracks that fake a D_s candidate to form a fake B_s^0 .
- 304 • Partially reconstructed $B^0/B_s^0 \rightarrow D_s^*\pi\pi\pi$ decays, with $D_s^* \rightarrow D_s\gamma$ or $D_s^* \rightarrow D_s\pi^0$,
305 where the γ/π^0 is not reconstructed in the decay chain.

306 In both cases of combinatorial background, the distribution in the invariant mass of
307 B_s^0 candidates is expected to be smooth and decrease with higher masses. Therefore, one
308 exponential function is used to model these contributions.

309 The shape of the $B_s^0 \rightarrow D_s^*\pi\pi\pi$ contribution is expected to be peaking in the $m(D_s\pi\pi\pi)$
310 spectrum, with large tails due to the missing momentum, which is carried away by the π^0
311 or γ . The pion or photon from $D_s^* \rightarrow D_s(\gamma/\pi^0)$ is excluded from the reconstruction. We
312 model the shape of this contribution using the sum of three bifurcated Gaussian functions.
313 The shape parameters, as well as the yield of this contribution, are directly determined
314 on data from a fit to the $m(D_s\pi\pi\pi)$ invariant mass distribution.

315 4.3 Background models for $m(D_sK\pi\pi)$

316 For the signal channel, the following background sources have to be considered:

- 317 • Combinatorial background: same contributions as discussed in Sec. 4.2.
- 318 • Partially reconstructed $B_s^0 \rightarrow D_s^*K\pi\pi$ decays, with $D_s^* \rightarrow D_s\gamma$ or $D_s^* \rightarrow D_s\pi^0$,
319 where the γ/π^0 is not reconstructed in the decay chain.
- 320 • Partially reconstructed $B^0 \rightarrow D_s^*K\pi\pi$ decays, with $D_s^* \rightarrow D_s\gamma$ or $D_s^* \rightarrow D_s\pi^0$,
321 where the γ/π^0 is not reconstructed in the decay chain.
- 322 • Misidentified $B_s^0 \rightarrow D_s\pi\pi\pi$ decays, where one of the pions is wrongly identified as a
323 kaon $\pi \rightarrow K$.
- 324 • Misidentified, partially reconstructed $B_s^0 \rightarrow D_s^*\pi\pi\pi$ decays, where one of the pions
325 is wrongly identified as a kaon $\pi \rightarrow K$ and the γ/π^0 from $D_s^* \rightarrow D_s\gamma/\pi^0$ is not
326 reconstructed.

327 The combinatorial background is expected to be non-peaking in the spectrum of the
328 invariant mass of $B_s^0 \rightarrow D_sK\pi\pi$ candidates. An exponential function is used to model
329 this contribution.

330 The shape of the partially reconstructed background without misID is taken from our
 331 normalization channel, where it can be directly fitted by the sum of three bifurcated
 332 Gaussian functions as described above. In the signal mass fit, all shape parameters for
 333 the $B_s^0 \rightarrow D_s^* K\pi\pi$ background are fixed to the input values from our normalization fit.

334 For the contribution of the $B^0 \rightarrow D_s^* K\pi\pi$ background, the same shape is used but
 335 the means μ_i of the bifurcated gaussians are shifted down by $m_{B_s^0} - m_{B^0}$ [?]. The yields
 336 of both contributions are directly determined in the nominal fit.

337 To determine the shape of misidentified $B_s^0 \rightarrow D_s\pi\pi\pi$ candidates in the $m(D_s K\pi\pi)$
 338 spectrum, we take a truth-matched signal MC sample of our normalization channel. We
 339 then use the PIDCalib package to determine the $\pi \rightarrow K$ fake rate. For every candidate
 340 in our MC sample, a (momentum) p and (pseudorapidity) η -dependent event weight is
 341 computed and assigned. We flip the particle hypothesis from pion to kaon for the π with
 342 the biggest miss-ID weight for each event and recompute the invariant B_s^0 mass. This
 343 distribution is then modeled using two Crystal Ball functions. The distribution and the
 344 fit are shown in Fig. 4.2(left).

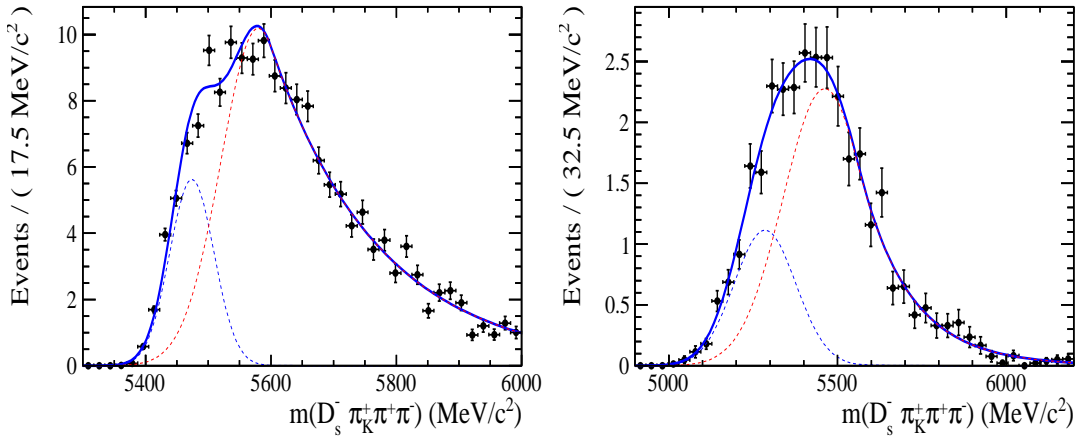


Figure 4.2: Invariant mass distribution of (left) simulated $B_s^0 \rightarrow D_s\pi\pi\pi$ events, where one of the π 's is reconstructed as a K and the misID probability for each event is taken into account. The corresponding distribution for simulated $B_s^0 \rightarrow D_s^*\pi\pi\pi$ events, where the γ/π^0 from the D_s^* is excluded from reconstruction, is shown on the right. The solid, black curve on each plot corresponds to the fit consisting of two Crystal Ball functions.

345 The expected yield of misidentified $B_s^0 \rightarrow D_s\pi\pi\pi$ candidates in the $m(D_s K\pi\pi)$ spec-
 346 trum is computed by multiplying the fake probability of $\propto 3.2\%$, which is derived from
 347 PIDCalib, by the yield of $B_s^0 \rightarrow D_s\pi\pi\pi$ signal candidates, determined in the nominal
 348 mass fit of our normalization channel.

349 In the same way as mentioned above, we can determine the rate of misidentified, partially
 350 reconstructed $B_s^0 \rightarrow D_s^*\pi\pi\pi$ decays in our sample of $B_s^0 \rightarrow D_s K\pi\pi$ decays using PIDCalib
 351 and a MC sample of $B_s^0 \rightarrow D_s^*\pi\pi\pi$ events. The invariant mass distribution we obtain
 352 when we exclude the γ/π^0 , flip the the particle hypothesis $\pi \rightarrow K$ and apply the event
 353 weights given by the fake rate, is shown in Fig. 4.2 (right). The fit of two Crystal Ball
 354 functions to this distribution is overlaid. The yield of this contribution is determined
 355 from the yield of $B_s^0 \rightarrow D_s^*\pi\pi\pi$ candidates in the nominal mass fit of our normalization
 356 channel, multiplied by the misID probability of $\propto 3.6\%$.

357 **4.4 Fit to $B_s^0 \rightarrow D_s\pi\pi\pi$ candidates**

358 An unbinned maximum likelihood fit is performed simultaneously to the invariant mass
 359 distribution of $B_s^0 \rightarrow D_s\pi\pi\pi$ candidates. As discussed in Sec. ??, the fit is given
 360 as a Johnson SU signal model for the B_s^0 and B^0 signal, the sum of three bifurcated
 361 Gaussian functions to model the partially reconstructed $B_s^0 \rightarrow D_s^*\pi\pi\pi$ background and
 362 an Exponential function to account for combinatorial background. The invariant mass
 363 distribution and the fit is shown in Fig. 4.3. All simultaneously performed fits to the
 364 $m(D_s\pi\pi\pi)$ distribution, ordered by the respective D_s final state, can be found in the
 365 Appendix ???. The obtained yields are summarized in Table 4.1.

366 **4.5 Fit to $B_s^0 \rightarrow D_sK\pi\pi$ candidates**

367 The shape of the invariant mass distribution of $B_s^0 \rightarrow D_sK\pi\pi$ candidates is described by
 368 Johnson SU functions for the B^0 and B_s^0 signal, two sums of three bifurcated Gaussians
 369 for the $B_s^0/B^0 \rightarrow D_s^*K\pi\pi$ partially reconstructed background contributions and two
 370 sums of double Crystal Ball functions for the single misID $B_s^0 \rightarrow D_s\pi\pi\pi$ and the partially
 371 reconstructed, misidentified $B_s^0 \rightarrow D_s^*\pi\pi\pi$ decays. A simultaneous unbinned maximum
 372 likelihood fit is performed and the result is shown in Fig. 4.3. All simultaneously performed
 373 fits to the $m(D_sK\pi\pi)$ distribution, ordered by the respective D_s final state, can be found
 374 in the Appendix ???. The obtained yields are summarized in Table 4.1.

375 **4.6 Extraction of signal weights**

376 The sPlot technique [31] is used to extract signal weights from the fits to the invariant
 377 mass distributions of our signal and normalization channel. This statistical tool assigns
 378 a weight to every event, according to its position in the respective mass distribution,
 379 given the fitted signal and background models. The weights can then be used to suppress
 380 the background components in every other observable distribution of interest. Figure ??
 381 shows the distribution of weights across the invariant mass spectra of $B_s^0 \rightarrow D_s\pi\pi\pi$ and
 382 $B_s^0 \rightarrow D_sK\pi\pi$ candidates.

fit component	yield 2011	yield 2012	yield 2015	yield 2016
$m(D_sK\pi\pi)$				
$B_s^0 \rightarrow D_sK\pi\pi$	392 ± 25	860 ± 38	309 ± 21	1984 ± 55
$B^0 \rightarrow D_sK\pi\pi$	276 ± 26	692 ± 41	261 ± 23	1385 ± 58
$B^0/B_s^0 \rightarrow D_s^*K\pi\pi$	7 ± 25	171 ± 75	114 ± 25	893 ± 84
$B_s^0 \rightarrow D_s^{(*)}\pi\pi\pi$	63 ± 0	158 ± 0	53 ± 0	314 ± 0
combinatorial	1482 ± 53	2884 ± 100	605 ± 43	4261 ± 133
$m(D_s\pi\pi\pi)$				
$B_s^0 \rightarrow D_s\pi\pi\pi$	9183 ± 105	22083 ± 166	7574 ± 95	43773 ± 245
$B^0 \rightarrow D_s\pi\pi\pi$	289 ± 58	716 ± 95	229 ± 54	968 ± 147
$B_s^0 \rightarrow D_s^*\pi\pi\pi$	3640 ± 130	9086 ± 232	3047 ± 110	17827 ± 421
combinatorial	4991 ± 154	11127 ± 271	3728 ± 126	24589 ± 500

Table 4.1: Summary of yields obtained from the fits to Run1 and Run2 data.

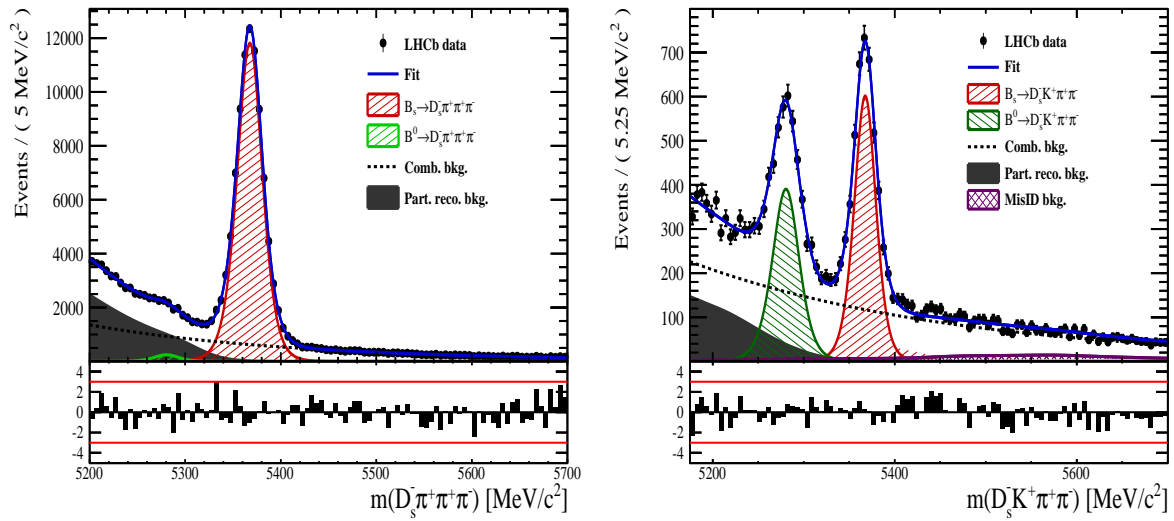


Figure 4.3: Invariant mass distribution of (left) $B_s^0 \rightarrow D_s \pi \pi \pi$ and (right) $B_s^0 \rightarrow D_s K \pi \pi$ candidates for Run1 and Run2 data. The respective fit described in the text is overlaid.

383 5 Flavour Tagging

384 To successfully perform a time- and amplitude-dependent measurement of γ , the identifi-
 385 cation of the initial state flavour of the B_s^0 meson is crucial. In the presented analysis,
 386 a number of flavour tagging algorithms are used that either determine the flavour of
 387 the non-signal b-hadron produced in the event (opposite site, OS), or they use particles
 388 produced in the fragmentation of the signal candidate B_s^0/\bar{B}_s^0 (same side, SS).
 389 For the same side, the algorithm searching for the charge of an additional kaon that accom-
 390 panies the fragmentation of the signal candidate is used (SS-nnetKaon). For the opposite
 391 site, four different taggers are chosen: The Two algorithms that use the charge of an
 392 electron or a muon from semileptonic B decays (OS- e,μ), the tagger that uses the charge
 393 of a kaon from a $b \rightarrow c \rightarrow s$ decay chain (OS-nnetKaon) and the algorithm that determines
 394 the B_s^0/\bar{B}_s^0 candidate flavour from the charge of a secondary vertex, reconstructed from
 395 the OS b decay product (OS-VtxCharge). All four taggers are then combined into a signal
 396 OS tagger.
 397 Every single tagging algorithm is prone to misidentify the signal candidate at a certain
 398 mistag rate $\omega = (\text{wrongtags})/(\text{alltags})$. This might be caused by particle misidentifica-
 399 tion, flavour oscillation of the neutral opposite site B-meson or by tracks that are wrongly
 400 picked up from the underlying event. For every signal B_s^0/\bar{B}_s^0 candidate, each tagging
 401 algorithm predicts a mistag probability η , which is calculated using a combination of
 402 inputs such as the kinematics of the tagging particles. The inputs are then combined
 403 to a predicted mistag using neural networks. These are trained on simulated samples
 404 of $B_s^0 \rightarrow D_s^- \pi^+$ (SS algorithm) and $B^+ \rightarrow J/\psi K^+$ (OS algorithms) decays. For the
 405 presented analysis, the measurable CP-violating coefficients are damped by the tagging
 406 dilution D , that depends on the mistag rate:

$$D = 1 - 2\omega. \quad (5.1)$$

407 This means that the statistical precision, with which these coefficients can be measured,
 408 scales as the inverse square root of the effective tagging efficiency,

$$\epsilon_{eff} = \epsilon_{tag}(1 - 2\omega)^2, \quad (5.2)$$

409 where ϵ_{tag} is the fraction of events that have a tagging decision. The flavour
 410 tagging algorithms are optimised for highest ϵ_{eff} on data, using the $B_s^0 \rightarrow D_s^- \pi^+$ and
 411 $B^+ \rightarrow J/\psi K^+$ samples.

412 Utilizing flavour-specific final states, the predicted mistag η of each tagger has to be
 413 calibrated to match the observed mistag ω on the data sample. For the calibration, a
 414 linear model of the form

$$\omega(\eta) = p_0 + p_1 \cdot (\eta - \langle \eta \rangle), \quad (5.3)$$

415 where the values of p_0 and p_1 are determined using the $B_s^0 \rightarrow D_s \pi \pi \pi$ normalization
 416 mode and $\langle \eta \rangle$ is the average estimated mistag probability $\langle \eta \rangle = \sum_{i=1}^{N_{cand}} (\eta_i)/N_{cand}$.
 417 Following this model, a perfectly calibrated tagger would lead to $\omega(\eta) = \eta$ and one would
 418 expect $p_1 = 1$ and $p_0 = \langle \eta \rangle$. Due to the different interaction cross-sections of oppositely
 419 charged particles, the tagging calibration parameters depend on the initial state flavour of
 420 the B_s^0 . Therefore, the flavour asymmetry parameters Δp_0 , Δp_1 and $\Delta \epsilon_{tag}$ are introduced.
 421 For this analysis, the calibrated mistag is treated as per-event variable, giving a larger

weight to events that are less likely to have an incorrect tag. This adds one additional observable to the time- and amplitude-dependent fit.
 The tagging calibration is determined using a time-dependent fit to the full $B_s^0 \rightarrow D_s\pi\pi\pi$ sample, where the mixing frequency Δm_s is fixed to the nominal PDG value [33]. The calibration procedure for the OS tagging algorithms (Sec.5.1) and the SS kaon tagger (Sec.5.2) is applied on the full Run I and 2015 and 2016 Run II $B_s^0 \rightarrow D_s\pi\pi\pi$ data sample, which is selected following the steps described in Sec. 3. The similar selection ensures as close as possible agreement between the $B_s^0 \rightarrow D_s\pi\pi\pi$ and $B_s^0 \rightarrow D_sK\pi\pi$ samples in terms of the decay kinematics, which are crucial for the flavour tagging. Section 5.3 shows the compatibility of both samples. After applying the calibration, the response of the OS and SS taggers are combined, which is shown in Sec. 5.4.

5.1 OS tagging calibration

The responses of the OS electron, muon, neural net kaon and the secondary vertex charge taggers are combined for the mistag calibration. Figure ?? shows the distribution of the predicted OS mistag for signal candidates from $B_s^0 \rightarrow D_s\pi\pi\pi$. The extracted calibration parameters and tagging asymmetries are summarized in Table 5.1 and the measured tagging power for the OS combination is $\epsilon_{eff,OS} = 4.81\%$.

p_0	p_1	$<\eta>$	ϵ_{tag}	Δp_o	Δp_1	ϵ_{eff} [%]
0.025 ± 0.005	0.944 ± 0.048	0.347	0.517 ± 0.002	0.028 ± 0.005	0.037 ± 0.045	4.81 ± 0.04 (stat) ± 0.37 (cal)

Table 5.1: Calibration parameters and tagging asymmetries of the OS tagger extracted from $B_s^0 \rightarrow D_s\pi\pi\pi$ decays.

5.2 SS tagging calibration

The SS neural net kaon tagger can be calibrated using the flavour-specific $B_s^0 \rightarrow D_s\pi\pi\pi$ decay. It's development, performance and calibration is described in detail in [34]. Figure ?? shows the distribution of the predicted mistag of the neural net kaon tagger. The extracted calibration parameters and tagging asymmetries are summarized in Table 5.2 and the measured tagging power for this algorithm is $\epsilon_{eff,SS} = 3.22\%$.

p_0	p_1	$<\eta>$	ϵ_{tag}	Δp_o	Δp_1	ϵ_{eff} [%]
0.008 ± 0.004	1.086 ± 0.059	0.381	0.571 ± 0.002	-0.017 ± 0.004	0.135 ± 0.058	3.22 ± 0.03 (stat) ± 0.26 (cal)

Table 5.2: Calibration parameters and tagging asymmetries of the SS tagger extracted from $B_s^0 \rightarrow D_s\pi\pi\pi$ decays.

5.3 Tagging performance comparison between the signal and normalization channel

To justify the usage of the tagging calibration, obtained using the $B_s^0 \rightarrow D_s\pi\pi\pi$ sample, for our signal decay, the performance of the taggers in the two decay channels needs to be compatible. This is verified using both, simulated signal samples of both decays and

450 sweighted data, to compare the similarity of the mistag probabilities, tagging decisions
 451 and kinematic observables that are correlated with the tagging response, on simulation
 452 and data.

453 The distributions of the predicted mistag probability η for the OS combination and the
 454 SS kaon tagger are shown in Fig. ?? (simulation) and Fig. 5.1 (data).

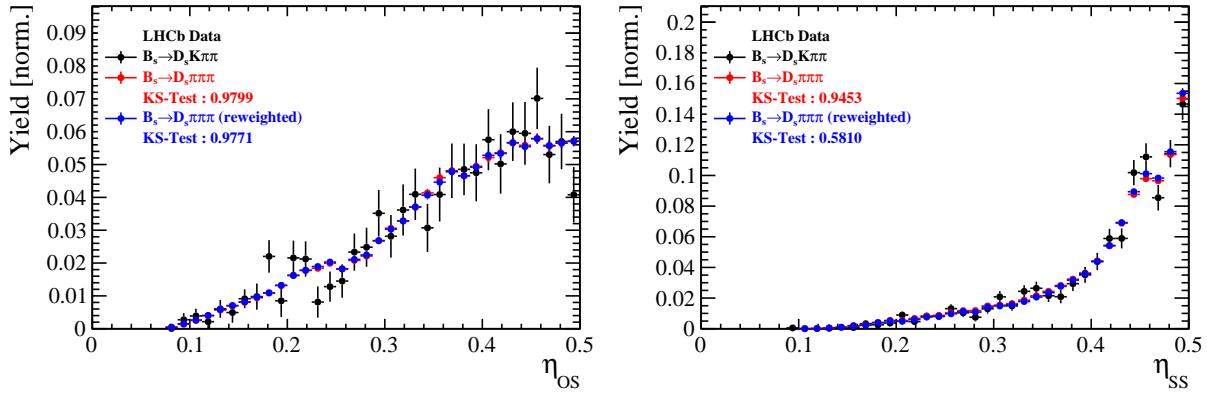


Figure 5.1: Distributions of the predicted mistag η for the OS combination (left) and the SS kaon tagger (right) for signal candidates in the $B_s^0 \rightarrow D_s K\pi\pi$ (black) and $B_s^0 \rightarrow D_s \pi\pi\pi$ (red) data samples.

455 Both, data and simulated samples, show good agreement between the signal and
 456 normalization channel. Compatibility is also seen in Fig. ??, which shows the comparison
 457 of the tagging decision distributions of the OS and SS tagger for sweighted data.

458 Fig. ?? shows the signal data distributions of the transverse B_s^0 momentum p_T , the
 459 pseudorapidity η of the signal candidate and the number of reconstructed tracks per event.
 460 Sufficient agreement is observed.

461 To justify the portability of the flavour tagging calibration obtained from $B_s^0 \rightarrow D_s \pi\pi\pi$
 462 to the $B_s^0 \rightarrow D_s K\pi\pi$ channel, besides the good agreement of the distributions shown
 463 above, the dependence of the measured mistag ω on the predicted mistag η has to be
 464 compatible in both channel. This dependence is shown in Fig. 5.2 for simulated signal
 465 events of both channels, where good agreement is observed.

466 5.4 Combination of OS and SS taggers

467 In the time- and amplitude-dependent fit to $B_s^0 \rightarrow D_s K\pi\pi$ data, the obtained tagging
 468 responses of the OS and SS tagger will be combined after the calibration described in the
 469 previous sections is applied. Events that aquire a mistag probability greater than 0.5 after
 470 the calibration will have their tagging decision flipped. For events where only one of the
 471 two taggers fired, the combination of the tagging decision is trivial. In those events where
 472 both taggers made a decision, we use the standard combination of taggers [35] provided
 473 by the flavour tagging group. In the nominal fit, the calibrated mistags ω are combined
 474 event by event for the OS and SS tager, thus adding one variable to observable to the
 475 fit procedure. This ensures that the uncertainties of the OS and SS tagging calibration
 476 parameters are propagated properly to the combined tagging response for each event.
 477 The taggging performance for the combined tagger in the categories SS tagged only, OS
 478 tagged only and SS+OS tagged, are shown in Tab. ?? for the signal and normalization

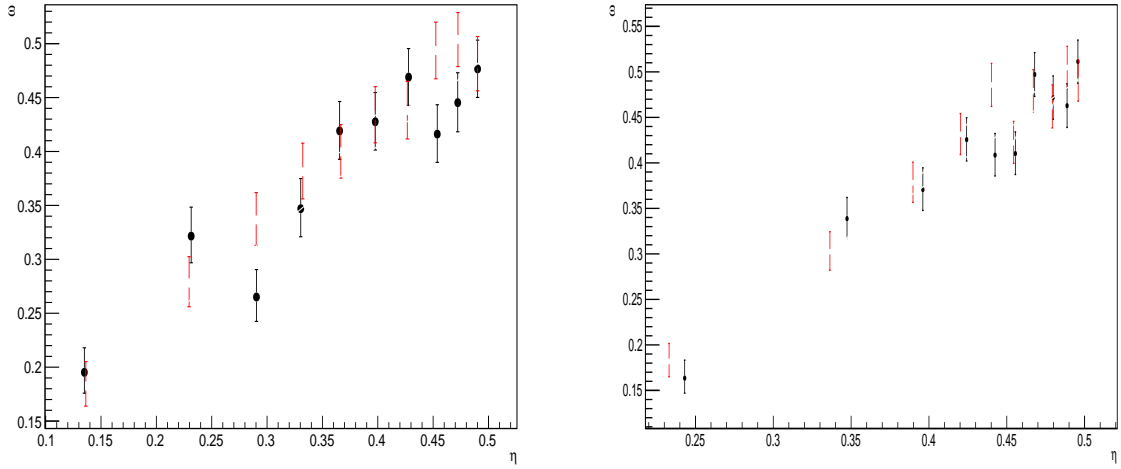


Figure 5.2: Dependence of the observed mistag ω on the predicted mistag η for the (left) OS combination and the (right) SS kaon tagger, found in the simulated $B_s^0 \rightarrow D_s K\pi\pi$ (black) and $B_s^0 \rightarrow D_s \pi\pi\pi$ (red) signal samples.

479 channel. The distribution of the observed mistag ω as a function of the combined mistag
 480 probability η for $B_s^0 \rightarrow D_s \pi\pi\pi$ decays is shown in Fig. 5.3.

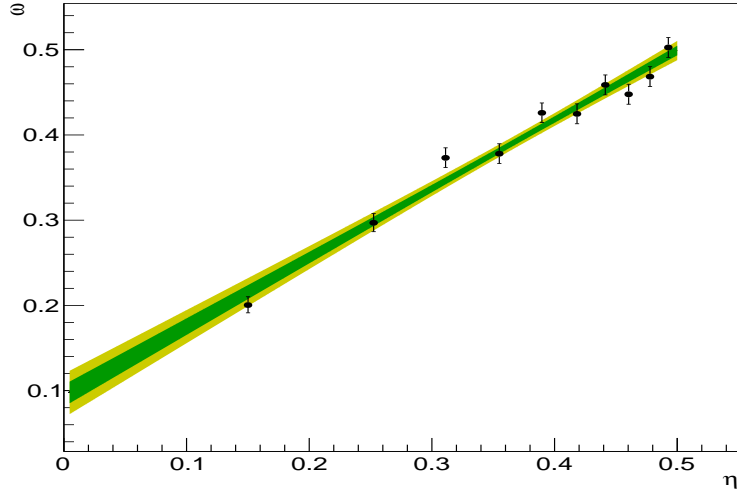


Figure 5.3: Distribution of the predicted combined mistag probability η versus the observed mistag ω for $B_s^0 \rightarrow D_s \pi\pi\pi$ signal candidates. The fit with a linear polynomial, used to determine p_0 and p_1 is overlaid.

$B_s^0 \rightarrow D_s\pi\pi\pi$		ϵ_{tag}	ϵ_{eff}
SS only		$(28.586 \pm 0.165)\%$	$(1.408 \pm 0.018(\text{stat}) \pm 0.082(\text{cal}))\%$
OS only		$(17.221 \pm 0.138)\%$	$(2.027 \pm 0.029(\text{stat}) \pm 0.100(\text{cal}))\%$
SS+OS		$(39.981 \pm 0.179)\%$	$(5.690 \pm 0.047(\text{stat}) \pm 0.196(\text{cal}))\%$
total			
$B_s^0 \rightarrow D_sK\pi\pi$		ϵ_{tag}	ϵ_{eff}
SS only		$(30.094 \pm 0.960)\%$	$(1.379 \pm 0.082(\text{stat}) \pm 0.085(\text{cal}))\%$
OS only		$(18.923 \pm 0.819)\%$	$(1.768 \pm 0.121(\text{stat}) \pm 0.099(\text{cal}))\%$
SS+OS		$(27.277 \pm 0.932)\%$	$(3.914 \pm 0.194(\text{stat}) \pm 0.220(\text{cal}))\%$
total			

Table 5.3: Flavour tagging performances for $B_s^0 \rightarrow D_s\pi\pi\pi$ and $B_s^0 \rightarrow D_sK\pi\pi$ events which are only OS tagged, only SS tagged or tagged by both.

481 6 Acceptance

482 6.1 MC corrections

483 6.1.1 Truth matching of simulated candidates

484 We use the `BackgroundCategory` tool to truth match our simulated candidates. Candidates
 485 with background category (`BKGCAT`) 20 or 50 are considered to be true signal. Background
 486 category 60 is more peculiar since it contains both badly reconstructed signal candidates
 487 and ghost background. This is due to the fact that the classification algorithms identifies
 488 all tracks for which less than 70% of the reconstructed hits are matched to generated
 489 truth-level quantities as ghosts. In particular for signal decays involving many tracks (as
 490 in our case), this arbitrary cutoff is not 100% efficient. Moreover, the efficiency is expected
 491 to depend on the kinematics which would lead to a biased acceptance determination if
 492 candidates with `BKGCAT`= 60 would be removed.

493 We therefore include `BKGCAT`= 60 and statistically subtract the ghost background by
 494 using the `sPlot` technique. The `sWeights` are calculated from a fit to the reconstructed B_s
 495 mass. The signal contribution is modeled as described in Sec. 4.1 and the background
 496 with a polynomial. The fit is performed simultaneously in two categories; the first includes
 497 events with `BKGCAT` = 20 or 50 and the second events with `BKGCAT` = 60. To account
 498 for the different mass resolution we use a different σ for each category, while the mean
 499 and the tail parameters are shared between them. The background component is only
 500 included for the second category.

501 A significant fraction of 8% of the true signal candidates are classified as ghosts, while
 502 only 20% of the events classified with `BKGCAT`= 60 are indeed genuine ghosts.

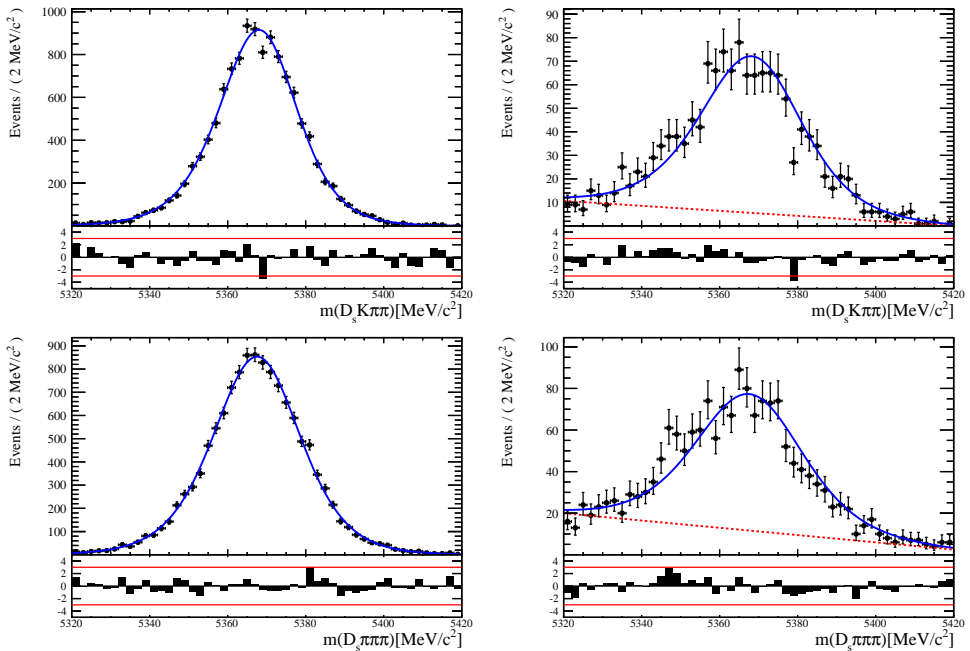


Figure 6.1: The reconstructed B_s mass distribution for simulated $B_s \rightarrow D_s K\pi\pi$ (top) and $B_s \rightarrow D_s \pi\pi\pi$ (bottom) decays classified with `BKGCAT` = 20 or 50 (left) and `BKGCAT` = 60 (right) after the full selection.

503 6.1.2 PID efficiencies

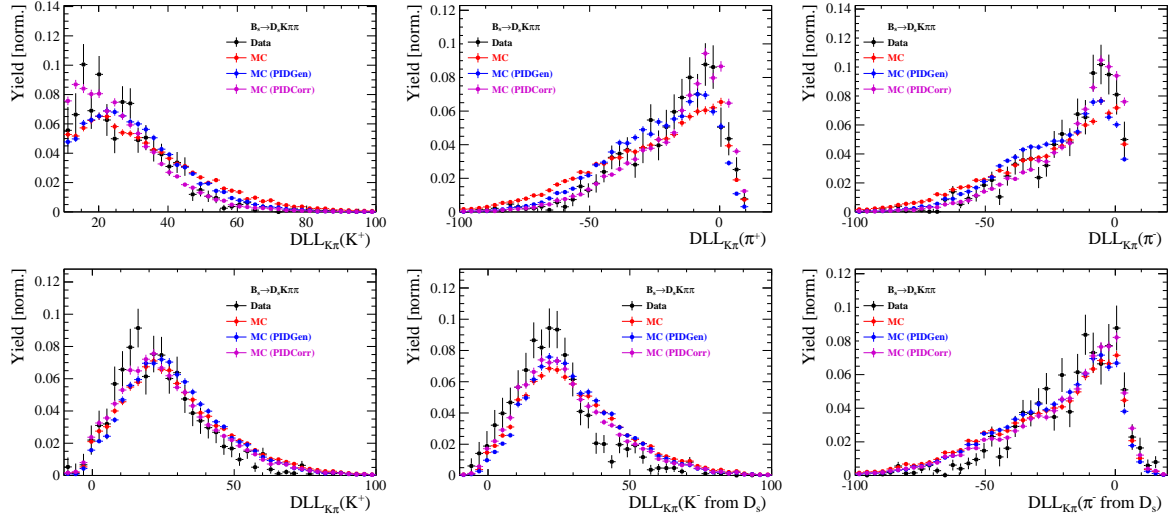


Figure 6.2

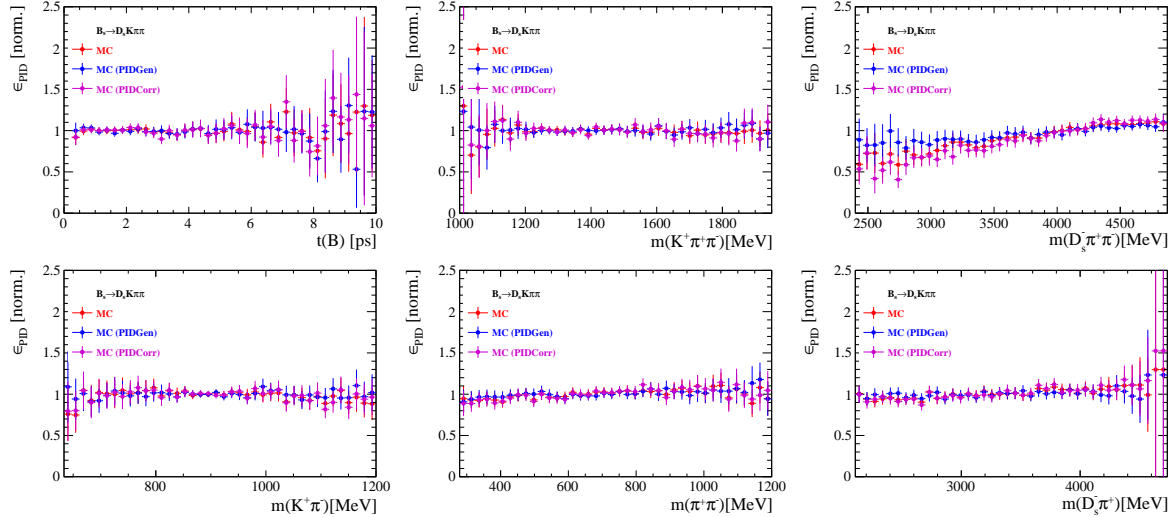


Figure 6.3

504 6.1.3 BDT efficiencies

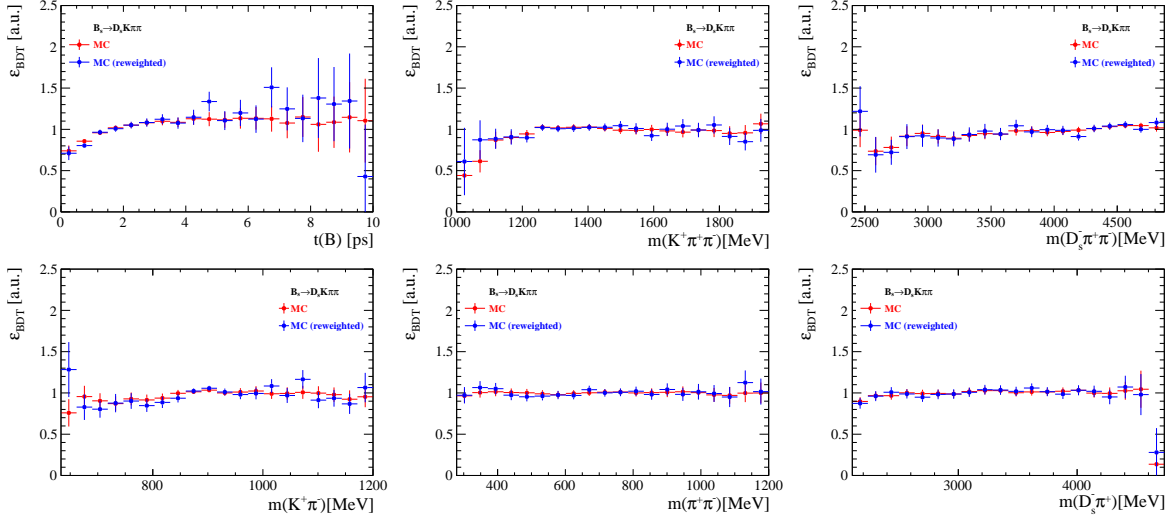


Figure 6.4

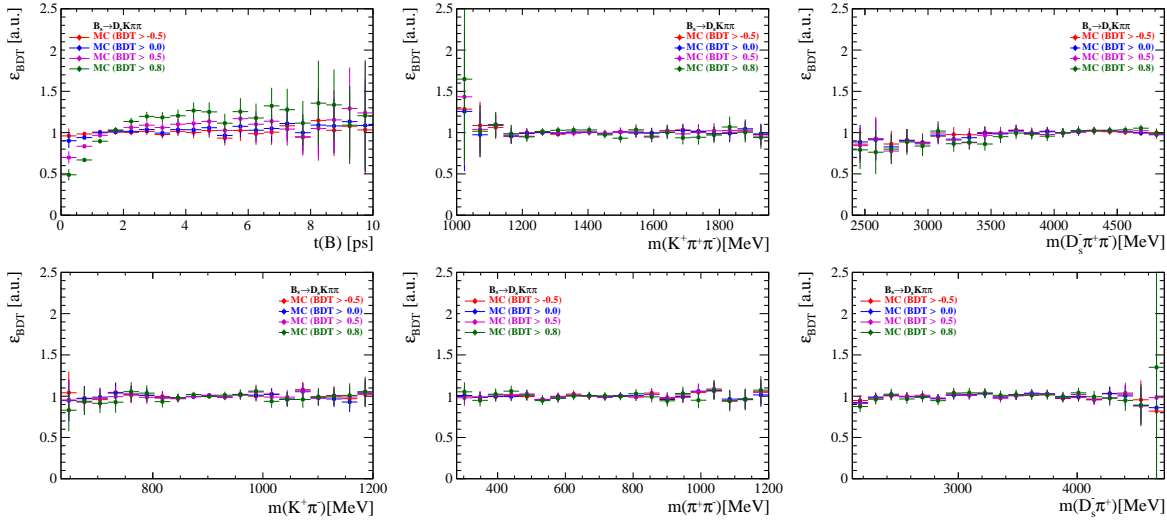


Figure 6.5

505 **6.1.4 Tracking efficiencies**

506 **6.2 Decay-time acceptance**

507 The decay-time distribution of the B_s^0 mesons is sculpted due to the geometry of the LHCb
 508 detector and the applied selection cuts, which are described in Section 3. In particular,
 509 any requirement on the flight distance (FD), the impact parameter (IP) or the direction
 510 angle (DIRA) of the B_s^0 mesons, as well as the direct cut on the lifetime, will lead to a
 511 decay-time dependent efficiency $a(t)$. This efficiency will distort the theoretically expected,
 512 time-dependent decay rate

$$\frac{\Gamma(t)^{observed}}{dt} = \frac{\Gamma(t)^{theory}}{dt} \cdot a(t), \quad (6.1)$$

513 and has to be modelled correctly, in order to describe the observed decay rate. We
 514 use our control channel for this measurement, because for $B_s^0 \rightarrow D_s K\pi\pi$ decays the
 515 decay-time acceptance is correlated with the CP-observables which we aim to measure.
 516 Therefore, floating the CP-observables and the acceptance shape at the same time is
 517 not possible. Hence, a fit to the decay-time distribution of $B_s^0 \rightarrow D_s \pi\pi\pi$ candidates is
 518 performed and the obtained acceptance shape is corrected by the difference in shape found
 519 for the $B_s^0 \rightarrow D_s K\pi\pi$ and $B_s^0 \rightarrow D_s \pi\pi\pi$ MC.

520 A PDF of the form

$$\mathcal{P}(t', \vec{\lambda}) = \left[(e^{\Gamma_s t} \cdot \cosh(\frac{\Delta\Gamma_s t}{2}) \times \mathcal{R}(t - t')) \right] \cdot \epsilon(t', \vec{\lambda}), \quad (6.2)$$

521 is fit to the decay time distribution of $B_s^0 \rightarrow D_s \pi\pi\pi$ candidates in data. Since the
 522 fit is performed untagged, the PDF shown in Eq. 6.2 contains no terms proportional
 523 to Δm_s . The values for Γ_s and $\Delta\Gamma_s$ are fixed to the latest HFAG results [36]. The
 524 decay-time acceptance $\epsilon(t', \vec{\lambda})$ is modelled using the sum of cubic polynomials $v_i(t)$, so
 525 called Splines [37]. The polynomials are parametrised by so-called knots which determine
 526 their boundaries. Knots can be set across the fitted distribution to account for local
 527 changes in the acceptance shape. Using more knots is equivalent to using more base
 528 splines which are defined on a smaller sub-range. In total, $n + 2$ base splines $v_i(t)$ are
 529 needed to describe an acceptance shape which is parametrised using n knots.

530 For fits shown in the following, the knots have been placed at $t = [0.5, 1.0, 1.5, 2.0, 3.0, 9.5] ps$. To accommodate these 6 knot positions, 8 basic splines
 531 v_i , $i = [1, \dots, 8]$ are used. Since a rapid change of the decay time acceptance at low
 532 decay times due to the turn-on effect generated by the lifetime and other selection cuts is
 533 expected, more knots are placed in that regime. At higher decay times we expect linear
 534 behavior, with a possible small effect due to the VELO reconstruction. Therefore fewer
 535 knots are used. Furthermore, v_7 is fixed to 1 in order to normalize the overall acceptance
 536 function. To stabilise the last spline, v_8 is fixed by a linear extrapolation from the two
 537 previous splines:

$$v_N = v_{N-1} + \frac{v_{N-2} - v_{N-1}}{t_{N-2} - t_{N-1}} \cdot (t_N - t_{N-1}). \quad (6.3)$$

538 Here, $N = 8$ and t_{N-1} corresponds to the knot position associated with v_{N-1} .

540 6.2.1 Comparison of acceptance in subsamples

541 It is possible that the decay-time dependent efficiency deviates in different subsamples of
 542 our data. In particular, the acceptance could differentiate in subsamples with different
 543 final state kinematics, such as the run I & run II sample, the various D_s final states and
 544 the ways an event is triggered at the L0 stage. To investigate possible deviations, the
 545 full selected $B_s^0 \rightarrow D_s\pi\pi\pi$ sample is split into subsamples according to the categories
 546 mentioned above (run, D_s state, L0 trigger). For each subsample, the fit procedure
 547 described at the beginning of this chapter, using the pdf given by Eq. 6.2, is repeated
 548 and the obtained values for the spline coefficients v_i are compared. Figure 6.6 shows the
 549 comparison of the obtained spline coefficients for the different D_s final states.

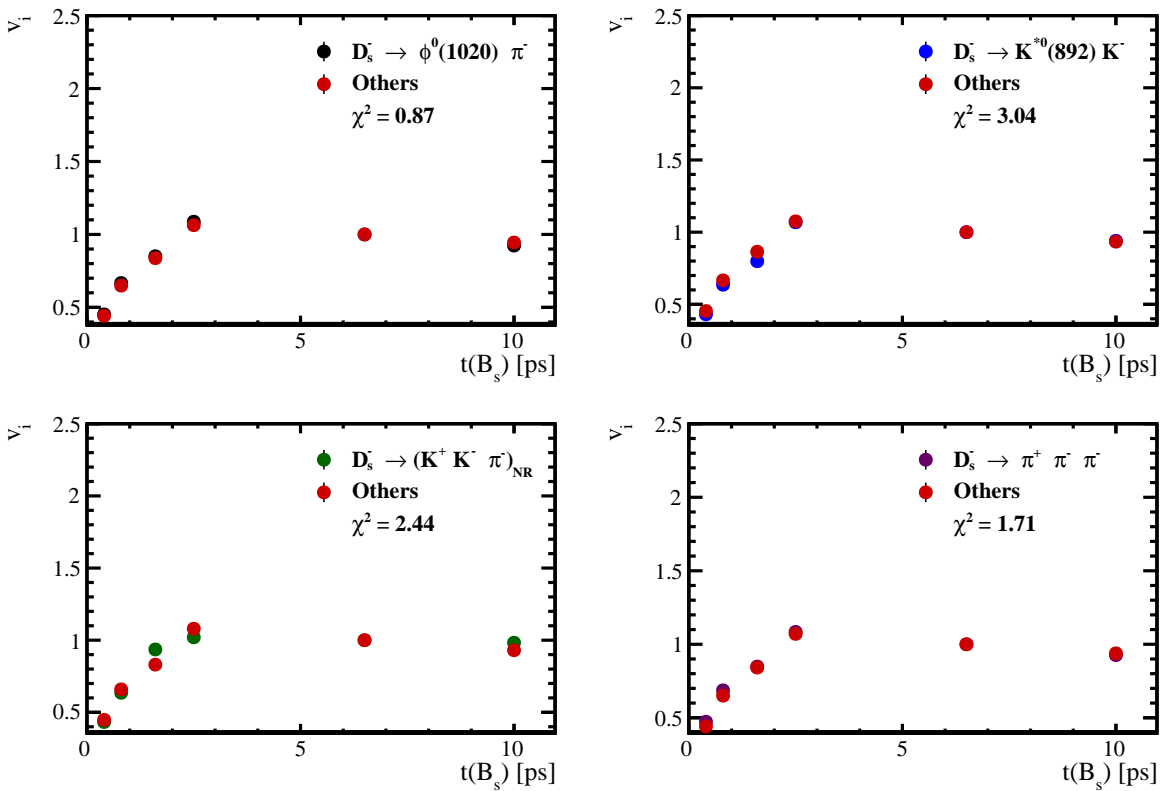


Figure 6.6: Comparison of the spline coefficients obtained from time-dependent fits to the $B_s^0 \rightarrow D_s\pi\pi\pi$ subsamples of different D_s final states. The comparison of one particular D_s state against all other states is shown.

550 Investigating the obtained spline coefficients from different D_s final states, good
 551 agreement is observed between all four channels and no need to distinguish between
 552 different final states in the time-dependent amplitude fit is found.

553 The comparison between spline coefficients for the different runs and L0 trigger categories
 554 is shown in Figure 6.7.

555 Significant deviations between spline coefficients obtained from the two different runs
 556 and L0 trigger categories can be observed. The deviations are most pronounced in the
 557 (0 – 5) ps region, where the majority of statistics is found. Therefore, the time-dependent
 558 efficiency has to be treated separately for the runs and L0 categories. This is achieved by

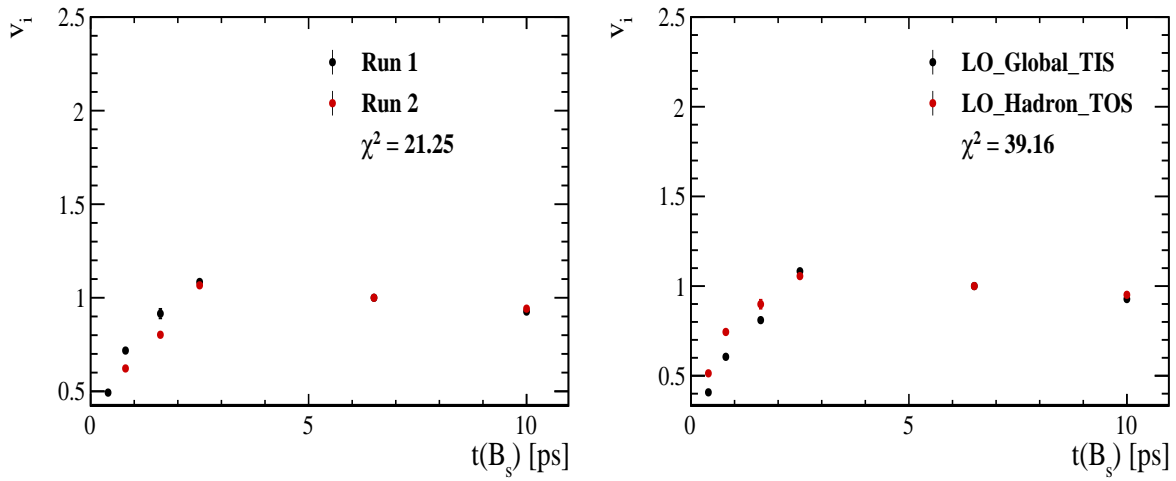


Figure 6.7: Comparison of the spline coefficients obtained from time-dependent fits to the $B_s^0 \rightarrow D_s \pi \pi \pi$ subsamples of (left) the different runs and (right) L0 trigger categories.

559 implementing a simultaneous fit, where the acceptance description is allowed to vary in
 560 the subsamples.

561 **6.2.2 Results**

562 The nominal fit to $B_s^0 \rightarrow D_s\pi\pi\pi$ data using this configuration is shown in Figure ??.
563 Note that the normalization of the splines in the following figures is not in scale. The fit
564 parameters obtained from the described fits to data and simulation are summarised in
565 Table 6.4.

Table 6.1: Time acceptance parameters for events in category [Run-I,L0-TOS].

Knot position	Coefficient	$B_s^0 \rightarrow D_s K\pi\pi$ data	$B_s^0 \rightarrow D_s K\pi\pi$ MC	Ratio
0.4	v_0	0.561 ± 0.038	0.546 ± 0.022	0.953 ± 0.060
0.8	v_1	0.826 ± 0.059	0.785 ± 0.034	0.910 ± 0.066
1.6	v_2	0.843 ± 0.087	0.905 ± 0.056	1.055 ± 0.095
2.5	v_3	1.154 ± 0.036	1.118 ± 0.028	0.930 ± 0.045
6.5	v_4	1.0 (fixed)	1.0 (fixed)	1.0 (fixed)
10.0	v_5	0.866 (interpolated)	0.897 (interpolated)	1.061 (interpolated)

Table 6.2: Time acceptance parameters for events in category [Run-I,L0-TIS].

Knot position	Coefficient	$B_s^0 \rightarrow D_s K\pi\pi$ data	$B_s^0 \rightarrow D_s K\pi\pi$ MC	Ratio
0.4	v_0	0.368 ± 0.031	0.412 ± 0.020	0.955 ± 0.077
0.8	v_1	0.583 ± 0.050	0.648 ± 0.033	0.910 ± 0.074
1.6	v_2	0.939 ± 0.101	0.953 ± 0.061	0.947 ± 0.096
2.5	v_3	1.052 ± 0.054	1.077 ± 0.035	1.003 ± 0.051
6.5	v_4	1.0 (fixed)	1.0 (fixed)	1.0 (fixed)
10.0	v_5	0.954 (interpolated)	0.932 (interpolated)	0.998 (interpolated)

Table 6.3: Time acceptance parameters for events in category [Run-II,L0-TOS].

Knot position	Coefficient	$B_s^0 \rightarrow D_s K\pi\pi$ data	$B_s^0 \rightarrow D_s K\pi\pi$ MC	Ratio
0.4	v_0	0.486 ± 0.009	0.482 ± 0.009	1.000 ± 0.000
0.8	v_1	0.691 ± 0.014	0.707 ± 0.015	1.000 ± 0.000
1.6	v_2	0.851 ± 0.024	0.926 ± 0.026	1.000 ± 0.000
2.5	v_3	1.061 ± 0.017	1.086 ± 0.018	1.000 ± 0.000
6.5	v_4	1.0 (fixed)	1.0 (fixed)	1.0 (fixed)
10.0	v_5	0.946 (interpolated)	0.925 (interpolated)	1.000 (interpolated)

Table 6.4: Time acceptance parameters for events in category [Run-II,L0-TIS].

Knot position	Coefficient	$B_s^0 \rightarrow D_s K\pi\pi$ data	$B_s^0 \rightarrow D_s K\pi\pi$ MC	Ratio
0.4	v_0	0.300 ± 0.007	0.482 ± 0.010	1.000 ± 0.000
0.8	v_1	0.476 ± 0.012	0.707 ± 0.016	1.000 ± 0.000
1.6	v_2	0.725 ± 0.023	0.926 ± 0.026	1.000 ± 0.000
2.5	v_3	1.064 ± 0.019	1.086 ± 0.018	1.000 ± 0.000
6.5	v_4	1.0 (fixed)	1.0 (fixed)	1.0 (fixed)
10.0	v_5	0.944 (interpolated)	0.925 (interpolated)	1.000 (interpolated)

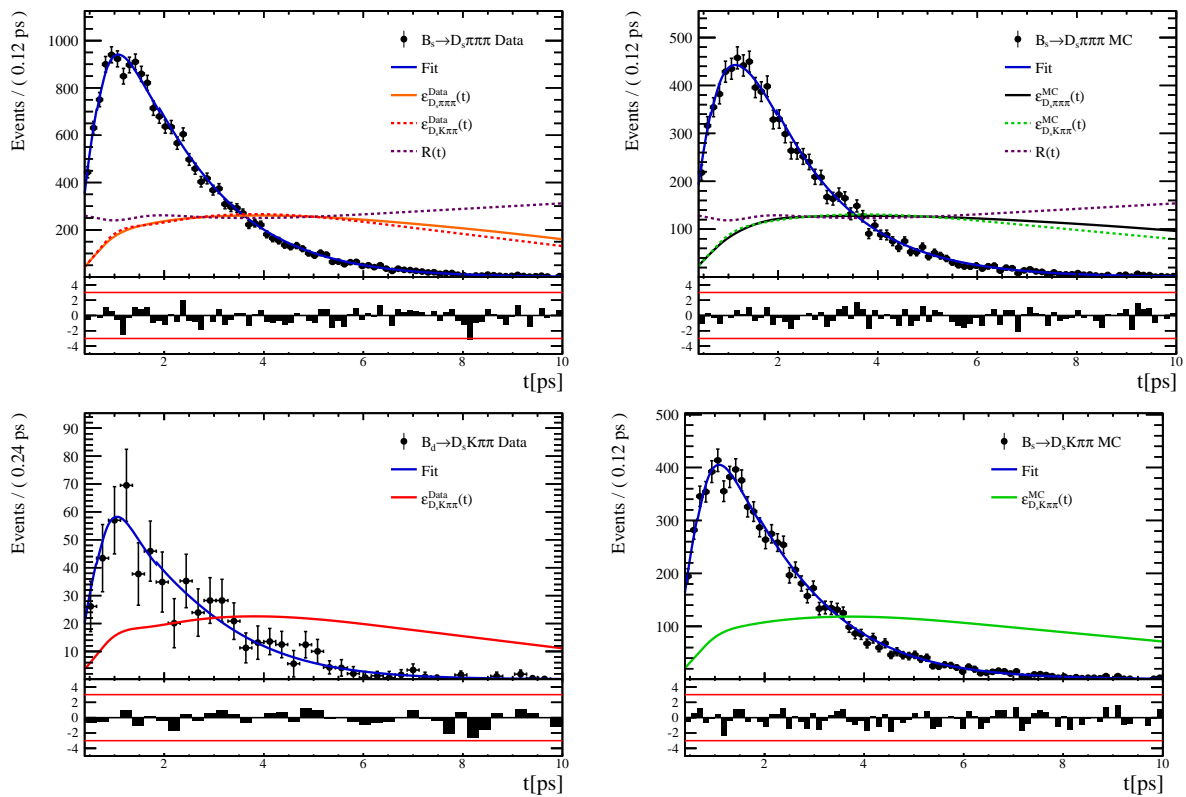


Figure 6.8

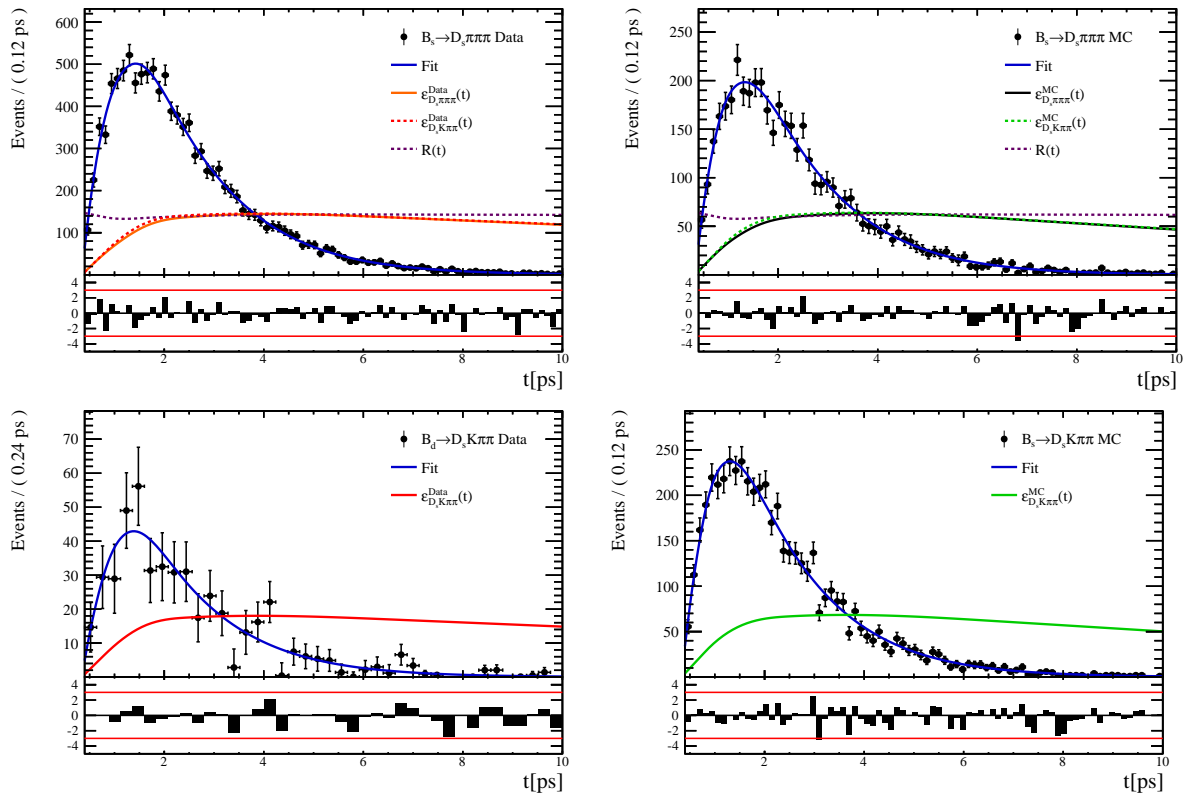


Figure 6.9

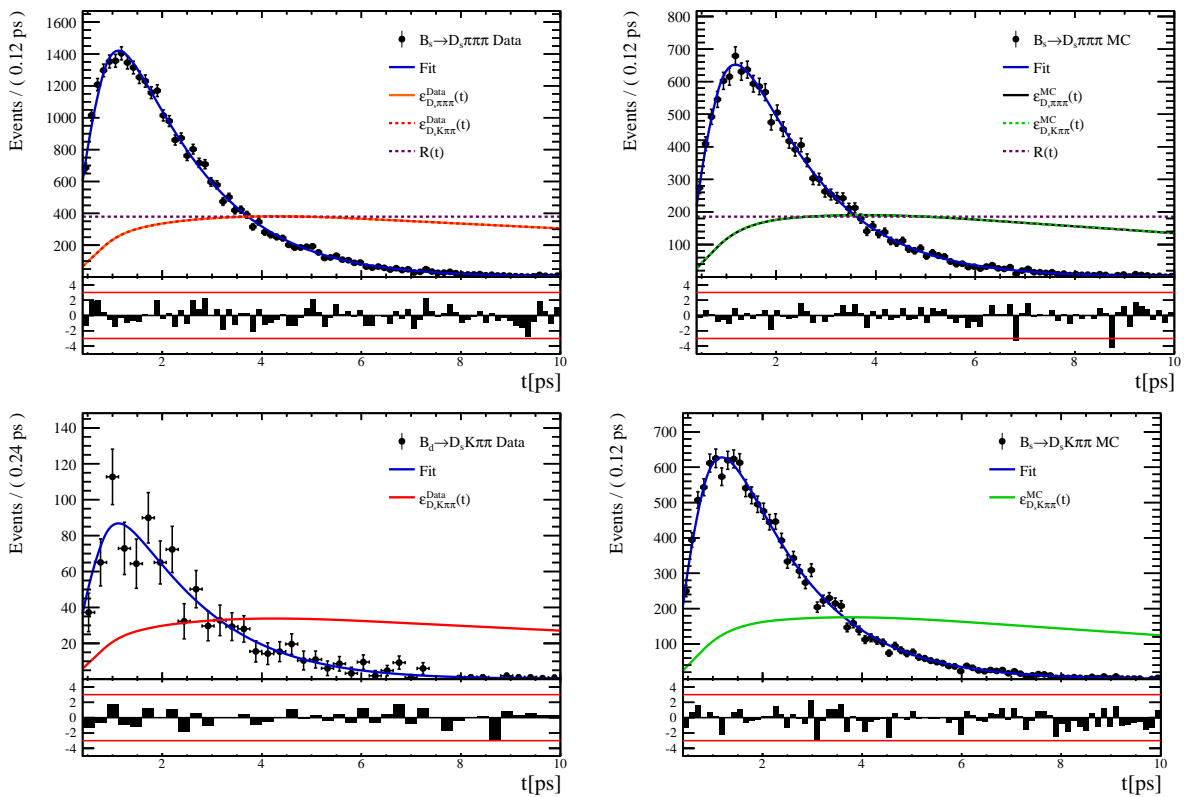


Figure 6.10

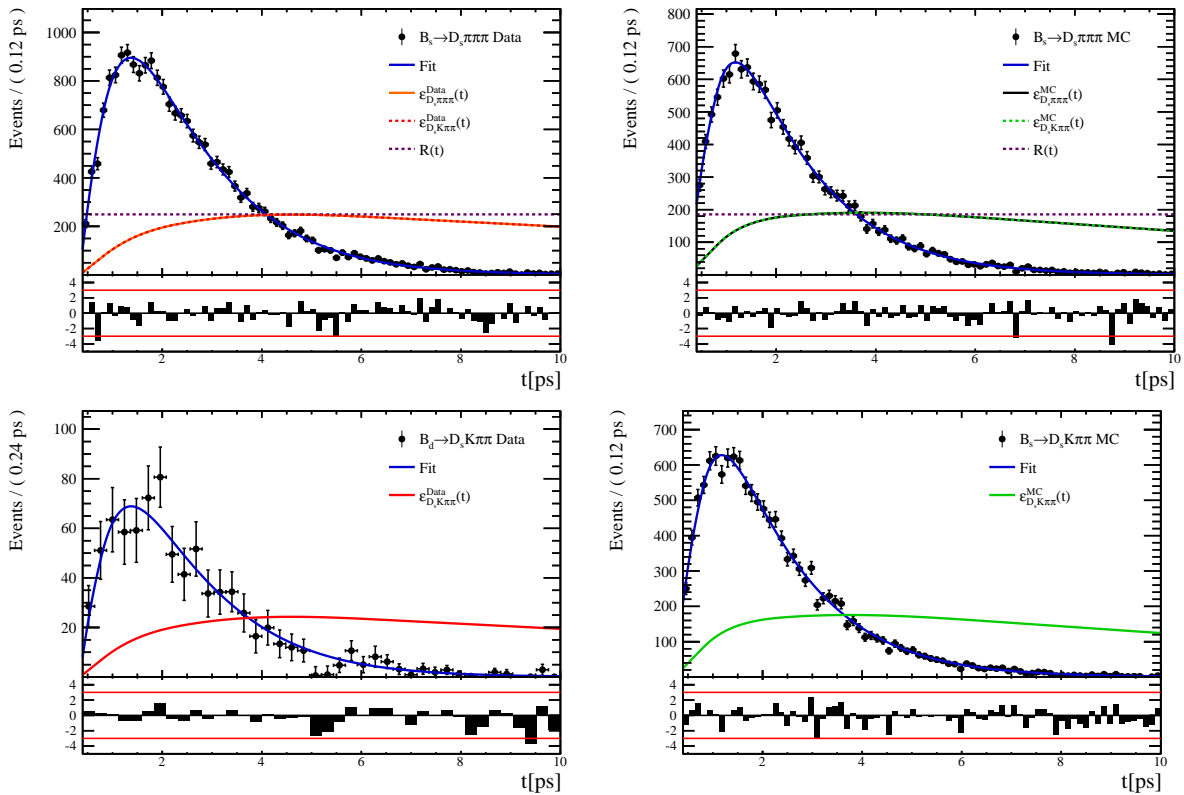


Figure 6.11

566 **6.3 Phasespace acceptance**

567 7 Decay-time Resolution

568 The observed oscillation of B mesons is prone to dilution, if the detector resolution is
 569 of similar magnitude as the oscillation period. In the B_s^0 system, considering that the
 570 measured oscillation frequency of the B_s^0 [33] and the average LHCb detector resolution [38]
 571 are both $\mathcal{O}(50 \text{ fs}^{-1})$, this is the case. Therefore, it is crucial to correctly describe the
 572 decay time resolution in order to avoid a bias on the measurement of time dependent CP
 573 violation. Since the time resolution depends on the particular event, especially the decay
 574 time itself, the sensitivity on γ can be significantly improved by using an event dependent
 575 resolution model rather than an average resolution. For this purpose, we use the per-event
 576 decay time error that is estimated based on the uncertainty obtained from the global
 577 kinematic fit of the momenta and vertex positions (DTF) with additional constraints on
 578 the PV position and the D_s mass. In order to apply it correctly, it has to be calibrated.
 579 The raw decay time error distributions for $B_s^0 \rightarrow D_s\pi\pi\pi$ signal candidates are shown in
 580 Figure 7.1 for Run-I and Run-II data. Significant deviations between the two different
 581 data taking periods are observed due to the increase in center of mass energy from Run-I
 582 to Run-II, as well as (among others) new tunings in the pattern and vertex reconstruction.
 583 The decay time error calibration is consequently performed separately for both data taking
 584 periods.

585 For Run-I data, we use the calibration from the closely related $B_s^0 \rightarrow D_s K$ analysis
 586 which was performed on a data sample of prompt- D_s candidates combined with a random
 587 pion track from the PV. We verify the portability to our decay channel on MC.

588 For Run-II data, a new lifetime unbiased stripping line (LTUB) has been implemented
 589 which selects prompt- D_s candidates combined with random $K\pi\pi$ tracks from the PV.

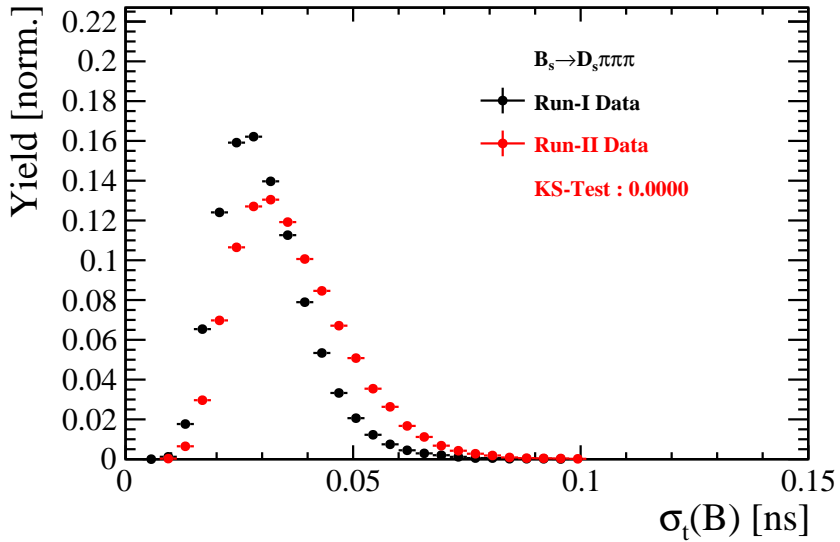


Figure 7.1: Distribution of the decay time error for $B_s^0 \rightarrow D_s\pi\pi\pi$ signal candidates for Run-I (black) and Run-II (red) data (sWeighted).

590 7.1 Calibration for Run-I data

591 For simulated $B_s^0 \rightarrow D_s K \pi\pi$ events, the spread of the differences between reconstructed
 592 decay time and true decay time, $\Delta t = t - t_{true}$, is a direct measure of the decay time
 593 resolution. The sum of two Gaussian pdfs with common mean but different widths is used
 594 to fit the distribution of the decay time difference Δt as shown in Fig. 7.2. The effective
 595 damping of the CP amplitudes due to the finite time resolution is described by the dilution
 596 \mathcal{D} . In the case of infinite precision, there would be no damping and therefore $\mathcal{D} = 1$ would
 597 hold, while for a resolution that is much larger than the B_s^0 oscillation frequency, \mathcal{D} would
 598 approach 0. For a double-Gaussian resolution model, the dilution is given by [39]

$$\mathcal{D} = f_1 e^{-\sigma_1^2 \Delta m_s^2 / 2} + (1 - f_1) e^{-\sigma_2^2 \Delta m_s^2 / 2}, \quad (7.1)$$

599 where σ_1 and σ_2 are the widths of the Gaussians, f_1 is the relative fraction of events
 600 described by the first Gaussian relative to the second and Δm_s is the oscillation frequency
 601 of B_s^0 mesons. An effective single Gaussian width is calculated from the dilution as,

$$\sigma_{eff} = \sqrt{(-2/\Delta m_s^2) \ln \mathcal{D}}, \quad (7.2)$$

602 which converts the resolution into a single-Gaussian function with an effective resolution
 603 that causes the same damping effect on the magnitude of the B_s oscillation. For the Run-I
 604 $B_s^0 \rightarrow D_s K \pi\pi$ MC sample the effective average resolution is found to be $\sigma_{eff} = 39.1 \pm 0.3$ fs.

605 To analyze the relation between the per-event decay time error δ_t and the actual
 606 resolution σ_t , the simulated $B_s^0 \rightarrow D_s K \pi\pi$ sample is divided into equal-statistics slices of
 607 δ_t . For each slice, the effective resolution is determined as described above. Details of the
 608 fit results in each slice are shown in appendix C. Figure 7.2 shows the obtained values
 609 for σ_{eff} as a function of the per-event decay time error σ_t . To account for the variable
 610 binning, the bin values are not placed at the bin center but at the weighted mean of the
 611 respective per-event-error bin. A linear function is used to parametrize the distribution.
 612 The obtained values are

$$\sigma_{eff}^{MC}(\sigma_t) = (0.0 \pm 0.0) \text{ fs} + (1.232 \pm 0.010) \sigma_t \quad (7.3)$$

613 where the offset is fixed to 0. For comparison, the calibration function found for $B_s^0 \rightarrow D_s K$
 614 MC is also shown in Figure 7.2 [39]:

$$\sigma_{eff}^{D_s K, MC}(\sigma_t) = (0.0 \pm 0.0) \text{ fs} + (1.201 \pm 0.013) \sigma_t. \quad (7.4)$$

615 Due to the good agreement between the scale factors for $B_s^0 \rightarrow D_s K$ and $B_s^0 \rightarrow D_s K \pi\pi$
 616 MC, we conclude that the resolution calibration for $B_s^0 \rightarrow D_s K$ data:

$$\sigma_{eff}^{D_s K}(\sigma_t) = (10.26 \pm 1.52) \text{ fs} + (1.280 \pm 0.042) \sigma_t \quad (7.5)$$

617 can be used for our analysis. The following calibration functions were used in the
 618 $B_s^0 \rightarrow D_s K$ analysis to estimate the systematic uncertainty on the decay-time resolution:

$$\sigma_{eff}^{D_s K}(\sigma_t) = (-0.568 \pm 1.570) \text{ fs} + (1.243 \pm 0.044) \sigma_t \quad (7.6)$$

$$\sigma_{eff}^{D_s K}(\sigma_t) = (0.0 \pm 0.0) \text{ fs} + (1.772 \pm 0.012) \sigma_t \quad (7.7)$$

620 The difference of the scale factors observed on $B_s^0 \rightarrow D_s K$ and $B_s^0 \rightarrow D_s K \pi\pi$ MC is
 621 assigned as additional systematic uncertainty.

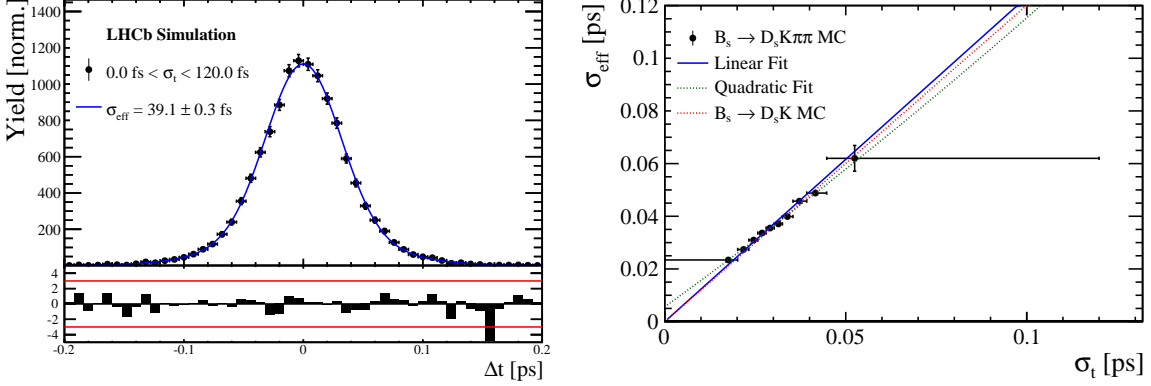


Figure 7.2: (Left) Difference of the true and measured decay time of $B_s^0 \rightarrow D_s K\pi\pi$ MC candidates. (Right) The measured resolution σ_{eff} as function of the per-event decay time error estimate σ_t for $B_s \rightarrow D_s K\pi\pi$ MC (Run-I). The fitted calibration curve is shown in blue.

7.2 Calibration for Run-II data

For the resolution calibration of Run-II data, a sample of promptly produced D_s candidates is selected using the B02DsKPiPiLTUBD2HHHBeauty2CharmLine stripping line. This lifetime-unbiased stripping line does not apply selection requirements related to lifetime or impact parameter, allowing for a study of the resolution. In order to reduce the rate of this sample it is pre-scaled in the stripping. Each D_s candidate is combined with a random kaon track and two random pion tracks which originate from the PV to obtain a sample of fake B_s candidates with a known true decay-time of $t_{true} = 0$. The difference of the measured decay time, t , of these candidates with respect to the true decay time is attributed to the decay time resolution.

The offline selection of the fake B_s candidates is summarized in Tab. 7.1. The selection is similar than the one for real data with the important difference that the D_s candidate is required to come from the PV by cutting on the impact parameter significance. Even after the full selection, a significant number of multiple candidates is observed. These are predominantly fake B_s candidates that share the same D_s candidate combined with different random tracks from the PV. We select one of these multiple candidates randomly which retains approximately 20% of the total candidates. The invariant mass distribution of the selected D_s candidates is shown in Fig. 7.3. To separate true D_s candidates from random combinations, the `sPlot` method is used to statistically subtract combinatorial background from the sample.

Figure 7.4 shows the `sWeighted` decay-time distribution for fake B_s candidates. Similar as in the previous section, the decay-time distribution is fitted with a double-Gaussian resolution model in slices of the per-event decay time error. Since some D_s candidates might actually originate from true B_s decays, the decay-time distribution of the fake B_s candidates might show a bias towards positive decay times. Therefore, we determine the decay-time resolution from the negative decay-time distribution only. Details of the fit results in each slice are shown in appendix C. The resulting calibration function:

$$\sigma_{eff}^{Data}(\sigma_t) = (9.7 \pm 1.7) \text{ fs} + (0.915 \pm 0.040) \sigma_t \quad (7.8)$$

⁶⁴⁹ is in good agreement with the one obtained for the $B_s \rightarrow J/\psi\phi$ (Run-II) analysis.

$$\sigma_{eff}^{J/\psi\phi}(\sigma_t) = (12.25 \pm 0.33) \text{ fs} + (0.8721 \pm 0.0080) \sigma_t \quad (7.9)$$

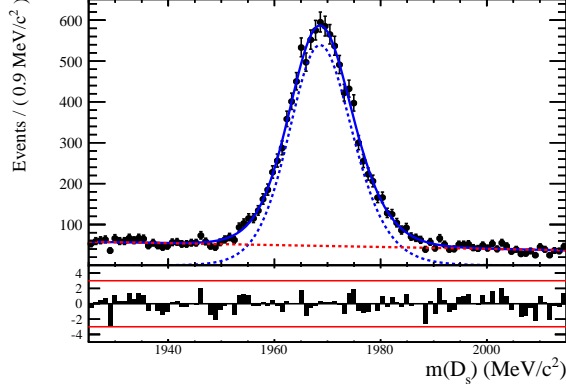


Figure 7.3: The invariant mass distribution for prompt D_s candidates.

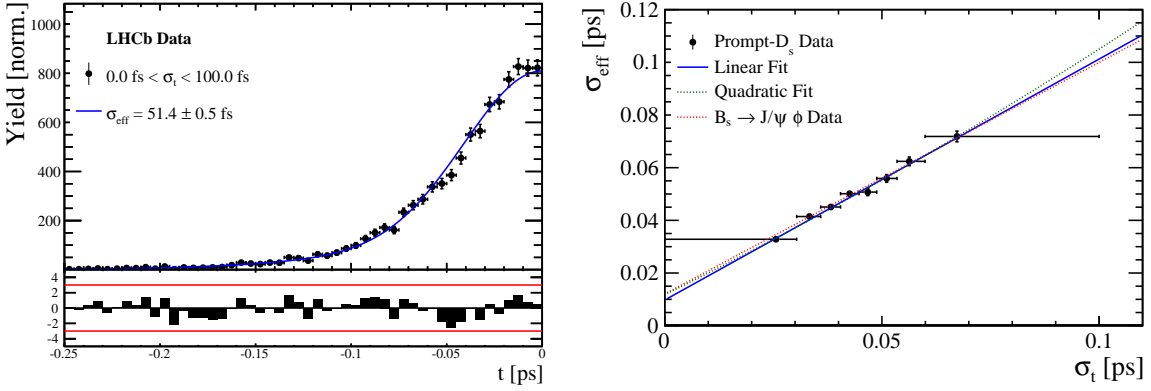


Figure 7.4: (Left) Decay-time distribution for fake B_s candidates from promptly produced D_s candidates, combined with random prompt $K\pi\pi$ bachelor tracks. (Right) The measured resolution σ_{eff} as function of the per-event decay time error estimate σ_t for fake B_s candidates (Run-II data). The fitted calibration curve is shown in blue.

Table 7.1: Offline selection requirements for fake B_s candidates from promptly produced D_s candidates combined with random prompt $K\pi\pi$ bachelor tracks.

	Description	Requirement
$B_s \rightarrow D_s K\pi\pi$	χ^2_{vtx}/ndof	< 8
	χ^2_{DTF}/ndof	< 15
	t	< 0 ps
$D_s \rightarrow hhh$	χ^2_{vtx}/ndof	< 5
	DIRA	> 0.99994
	χ^2_{FD}	> 9
	p_T	> 1800 MeV
	χ^2_{IP}	< 9
	$\chi^2_{IP}(h)$	> 5
	Wrong PV veto	$nPV = 1 \parallel \min(\Delta\chi^2_{IP}) > 20$
$D_s^- \rightarrow KK\pi^-$	D^0 veto	$m(KK) < 1840$ MeV
	D^- veto	$m(K^+K_\pi^-\pi^-) \neq m(D^-) \pm 30$ MeV
	Λ_c veto	$m(K^+K_p^-\pi^-) \neq m(\Lambda_c) \pm 30$ MeV
$D_s^- \rightarrow \phi\pi^-$	$m(KK)$	$= m_\phi \pm 20$ MeV
	PIDK(K^+)	> -10
	PIDK(K^-)	> -10
	PIDK(π^-)	< 20
$D_s^- \rightarrow K^*(892)K^-$	$m(KK)$	$\neq m_\phi \pm 20$ MeV
	$m(K^+\pi^-)$	$= m_{K^*(892)} \pm 75$ MeV
	PIDK(K^+)	> -10
	PIDK(K^-)	> -5
	PIDK(π^-)	< 20
$D_s^- \rightarrow (KK\pi^-)_{NR}$	$m(KK)$	$\neq m_\phi \pm 20$ MeV
	$m(K^+\pi^-)$	$\neq m_{K^*(892)} \pm 75$ MeV
	PIDK(K^+)	> 5
	PIDK(K^-)	> 5
	PIDK(π^-)	< 10
$D_s \rightarrow \pi\pi\pi$	PIDK(h)	< 10
	PIDp(h)	< 10
	D^0 veto	$m(\pi^+\pi^-) < 1700$ MeV
$X_s \rightarrow K\pi\pi$	$\chi^2_{IP}(h)$	< 40
	PIDK(K)	> 10
	PIDK(π)	< 5
	isMuon(h)	False
All tracks	p_T	> 500 MeV

650 7.3 Cross-checks

651 7.3.1 Kinematic dependence

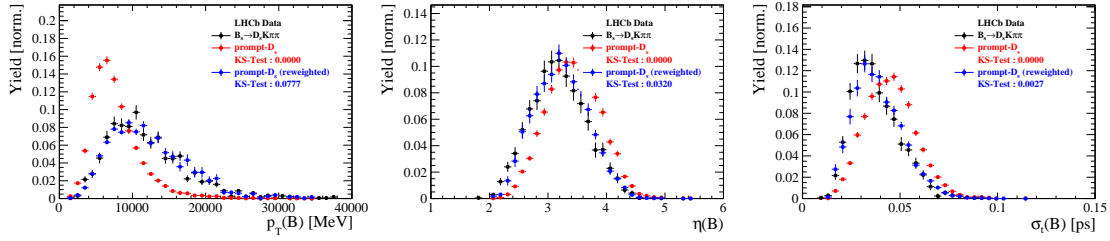


Figure 7.5

652 7.3.2 DTF constraints

653 8 Production and Detection Asymmetries

654 8.1 B_s Production Asymmetry

Table 8.1: B_s production asymmetry for 2011 data.

p_T [GeV/c]	y	$A_P(B_s^0)_{\sqrt{s}=7 \text{ TeV}}$
(2.00, 7.00)	(2.10, 3.00)	$0.0166 \pm 0.0632 \pm 0.0125$
(2.00, 7.00)	(3.00, 3.30)	$0.0311 \pm 0.0773 \pm 0.0151$
(2.00, 7.00)	(3.30, 4.50)	$-0.0833 \pm 0.0558 \pm 0.0132$
(7.00, 9.50)	(2.10, 3.00)	$0.0364 \pm 0.0479 \pm 0.0068$
(7.00, 9.50)	(3.00, 3.30)	$0.0206 \pm 0.0682 \pm 0.0127$
(7.00, 9.50)	(3.30, 4.50)	$0.0058 \pm 0.0584 \pm 0.0089$
(9.50, 12.00)	(2.10, 3.00)	$-0.0039 \pm 0.0456 \pm 0.0121$
(9.50, 12.00)	(3.00, 3.30)	$0.1095 \pm 0.0723 \pm 0.0179$
(9.50, 12.00)	(3.30, 4.50)	$0.1539 \pm 0.0722 \pm 0.0212$
(12.00, 30.00)	(2.10, 3.00)	$-0.0271 \pm 0.0336 \pm 0.0061$
(12.00, 30.00)	(3.00, 3.30)	$-0.0542 \pm 0.0612 \pm 0.0106$
(12.00, 30.00)	(3.30, 4.50)	$-0.0586 \pm 0.0648 \pm 0.0150$

Table 8.2: B_s production asymmetry for 2012 data.

p_T [GeV/c]	y	$A_P(B_s^0)_{\sqrt{s}=8 \text{ TeV}}$
(2.00, 7.00)	(2.10, 3.00)	$0.0412 \pm 0.0416 \pm 0.0150$
(2.00, 7.00)	(3.00, 3.30)	$-0.0241 \pm 0.0574 \pm 0.0079$
(2.00, 7.00)	(3.30, 4.50)	$0.0166 \pm 0.0391 \pm 0.0092$
(7.00, 9.50)	(2.10, 3.00)	$0.0482 \pm 0.0320 \pm 0.0067$
(7.00, 9.50)	(3.00, 3.30)	$0.0983 \pm 0.0470 \pm 0.0155$
(7.00, 9.50)	(3.30, 4.50)	$-0.0430 \pm 0.0386 \pm 0.0079$
(9.50, 12.00)	(2.10, 3.00)	$0.0067 \pm 0.0303 \pm 0.0063$
(9.50, 12.00)	(3.00, 3.30)	$-0.1283 \pm 0.0503 \pm 0.0171$
(9.50, 12.00)	(3.30, 4.50)	$-0.0500 \pm 0.0460 \pm 0.0104$
(12.00, 30.00)	(2.10, 3.00)	$-0.0012 \pm 0.0222 \pm 0.0050$
(12.00, 30.00)	(3.00, 3.30)	$0.0421 \pm 0.0416 \pm 0.0162$
(12.00, 30.00)	(3.30, 4.50)	$0.0537 \pm 0.0447 \pm 0.0124$

655 8.2 $K^- \pi^+$ Detection Asymmetry

656 The presented measurement of the CKM-angle γ using $B_s^0 \rightarrow D_s K \pi \pi$ decays is sensitive
 657 to a possible charge asymmetry of the kaon. This effect can be detector induced, because
 658 kaons are known to have a nuclear cross-section which is asymmetrically dependent on
 659 the sign of their charge. It is indispensable to determine the detector induced charge
 660 asymmetry of the kaon, as fitting without taking this effect into account would introduce
 661 a 'fake' CP violation. Instead of determining the single track detection asymmetry of a

662 kaon, it is found [40] that the combined two track asymmetry of a kaon-pion pair is much
 663 easier to access. Therefore the two track asymmetry is used, which is defined as

$$A^{det}(K^-\pi^+) = \frac{\epsilon^{det}(K^-\pi^+) - \epsilon^{det}(K^+\pi^-)}{\epsilon^{det}(K^-\pi^+) + \epsilon^{det}(K^+\pi^-)}. \quad (8.1)$$

664 $A^{det}(K^-\pi^+)$ can further be expressed, assuming no CP violation in Cabibbo-favoured
 665 charm modes, as [41]

$$\begin{aligned} A^{det}(K^-\pi^+) &= \frac{N(D^+ \rightarrow K^-\pi^+\pi^+) - N(D^- \rightarrow K^+\pi^-\pi^-)}{N(D^+ \rightarrow K^-\pi^+\pi^+) + N(D^- \rightarrow K^+\pi^-\pi^-)} \\ &\quad - \frac{N(D^+ \rightarrow K_s^0\pi^+) - N(D^- \rightarrow K_s^0\pi^-)}{N(D^+ \rightarrow K_s^0\pi^+) + N(D^- \rightarrow K_s^0\pi^-)} \\ &\quad - A(K^0), \end{aligned} \quad (8.2)$$

666 where possible CP violation in the $D^+ \rightarrow K_s^0\pi^+$ mode is predicted to be smaller than
 667 10^{-4} in the Standard Model [42]. Using Eq. 8.2, the two track $K^-\pi^+$ asymmetry is
 668 obtained from the difference in asymmetries in the $D^+ \rightarrow K^-\pi^+\pi^+$ and $D^+ \rightarrow K_s^0\pi^+$
 669 modes. $A(K^0)$ is the asymmetry in the neutral kaon system and has to be taken into
 670 account as a correction.

671 We use a dedicated LHCb tool to determine $A^{det}(K^-\pi^+)$ for all data taking periods
 672 used in this analysis. A detailed description can be found in [41]. The tool provides
 673 large calibration samples of $D^\pm \rightarrow K^\pm\pi^\pm\pi^\pm$ and $D^\pm \rightarrow K_s^0\pi^\pm$ decays, which are used to
 674 determine the asymmetry following Eq. 8.2. Several weighting steps are performed to
 675 match the kinematics of the calibration samples to our signal decay sample:

676 First, weights are assigned to the K^\pm and π^\pm of the $D^\pm \rightarrow K^\pm\pi^\pm\pi^\pm$ sample, using p ,
 677 η of the K^\pm and p_T , η of the π^\pm from our $B_s^0 \rightarrow D_s K\pi\pi$ signal decay. Then, weights
 678 are assigned to the D^\pm (p_T, η) and the π^\pm (p_T) of the $D^\pm \rightarrow K_s^0\pi^\pm$ sample to match
 679 the corresponding, weighted distributions of the $D^\pm \rightarrow K^\pm\pi^\pm\pi^\pm$ sample. In a last
 680 step, weights are assigned to match the bachelor pions ϕ distributions between the two
 681 calibration samples.

682 After the samples are weighted, fits are performed to the invariant
 683 $m(K^-\pi^+\pi^+)/m(K^+\pi^-\pi^-)$ and $m(K_s^0\pi^+)/m(K_s^0\pi^-)$ distributions to determine
 684 $A^{det}(K^-\pi^+)$. The PDFs used to describe the invariant mass distributions consist of
 685 gaussian functions for the signal component and exponentials describing the residual
 686 background. The detection asymmetry is determined separately for every year and
 687 (since it is a charge asymmetry effect) magnet polarity. Serving as an example for Run-I
 688 and Run-II, the fits used to determine $N(D^+ \rightarrow K^-\pi^+\pi^+)/N(D^- \rightarrow K^+\pi^-\pi^-)$ and
 689 $N(D^+ \rightarrow K_s^0\pi^+)/N(D^- \rightarrow K_s^0\pi^-)$ for 2011, magnet up data and 2015, magnet up data
 690 are shown in Fig. 8.1 and 8.2 respectively. The obtained values of $A^{det}(K^-\pi^+) + A(K^0)$
 691 for all years and polarities are shown in Table 8.3.

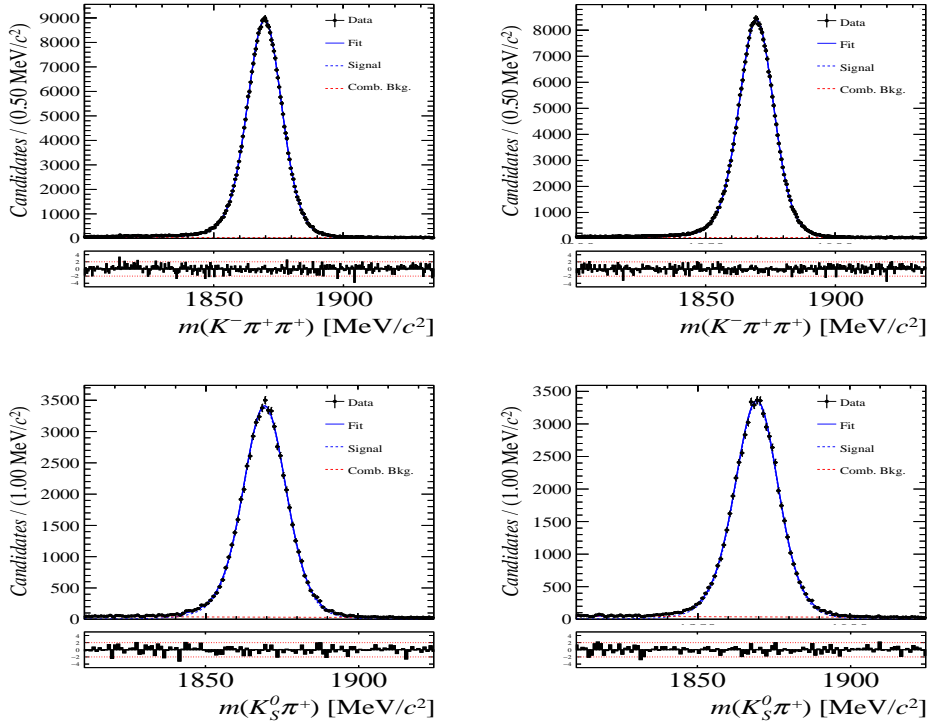


Figure 8.1: Distributions of the invariant mass of (top) $D^\pm \rightarrow K^\pm \pi^\pm \pi^\pm$ and (bottom) $D^\pm \rightarrow K_S^0 \pi^\pm$ candidates for Run-I data from the calibration samples. A fit described in the text is overlaid.

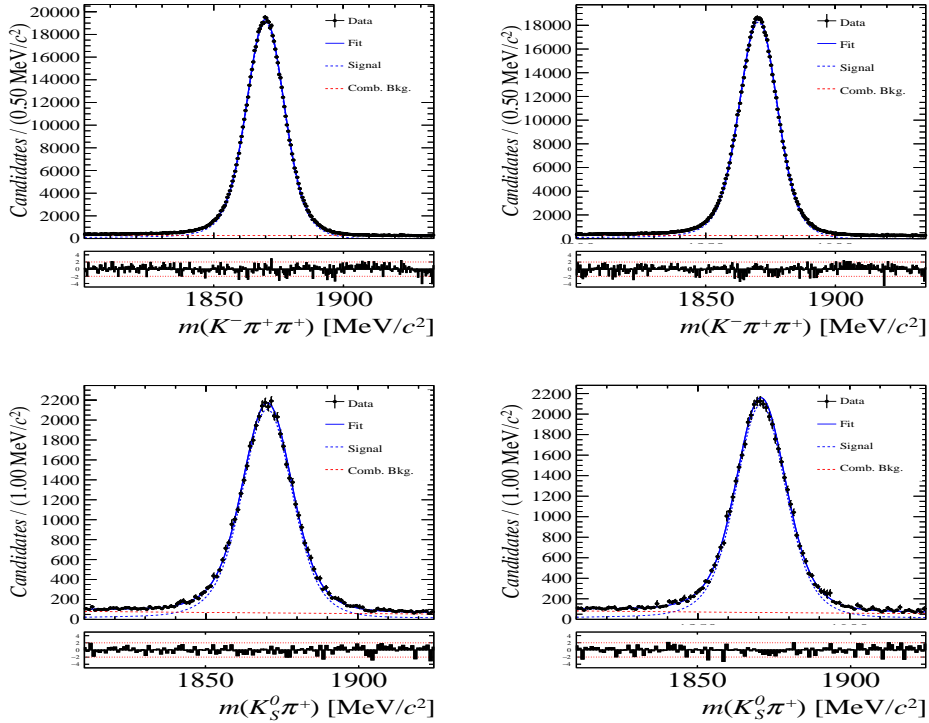


Figure 8.2: Distributions of the invariant mass of (top) $D^\pm \rightarrow K^\pm \pi^\pm \pi^\pm$ and (bottom) $D^\pm \rightarrow K_S^0 \pi^\pm$ candidates for Run-II data from the calibration samples. A fit described in the text is overlaid.

Data sample	$A^{det}(K^-\pi^+) + A(K^0)$ [%]
Run-I	
2011, mag. up	-2.01 \pm 0.32
2011, mag. down	-0.16 \pm 0.28
2011, average	-1.09 \pm 0.21
2012, mag. up	-0.90 \pm 0.20
2012, mag. down	-1.01 \pm 0.22
2012, average	-0.96 \pm 0.15
Run-II	
2015, mag. up	-1.36 \pm 0.36
2015, mag. down	-0.96 \pm 0.24
2015, average	-1.16 \pm 0.22
2016, mag. up	0.50 \pm 0.88
2016, mag. down	1.23 \pm 0.72
2016, average	0.87 \pm 0.57

Table 8.3: Summary of the $K^-\pi^+$ detection asymmetry obtained from the fits to the Run-I and Run-II calibration samples.

9 Time dependent fit

This section will cover the phasespace integrated, time dependent fit to $B_s^0 \rightarrow D_s h\pi\pi$ data, which is described by the PDF formulated in Eq. 2.6. For the phasespace integrated fit to $B_s^0 \rightarrow D_s K\pi\pi$ data, the sensitivity to the CKM phase γ will depend on the magnitude of the coherence factor κ , defined in Eq. 2.10, which is added as an additional fit parameter. In order to avoid any pollution of the final data samples by background events, both samples are weighted using the sWeights obtained by the fits to the invariant mass distributions, described in Sec. 4. This fit approach is commonly known as *sFit*. As additional input to the fit, the tagging information (Sec. 5), as well as the decay time acceptance (Sec. 6) and resolution (Sec. 7) is used and fixed to the values obtained by the dedicated studies. Taking all inputs into account, the final time dependent fit PDF is given by

$$\mathcal{P}\mathcal{D}\mathcal{F}(t, \vec{\lambda}) = \left(\epsilon(t) \cdot \int P(x, t, q_t, q_f) dx \right) \times \mathcal{R}(t - t'), \quad (9.1)$$

where $\int P(x, t, q_t, q_f) dx$ is the PDF given by Eq. 2.6, $\epsilon(t)$ is the efficiency due to the time acceptance effects and $\mathcal{R}(t - t')$ is the Gaussian time resolution function.

9.1 sFit to $B_s^0 \rightarrow D_s \pi\pi\pi$ data

The phasespace-integrated, time-dependent fit is performed to the full sWeighted sample of selected candidates from Run I and 2015+2016 Run II data, containing both possible magnet polarities and D_s final states. In the fit, the values of Γ_s and $\Delta\Gamma_s$ are fixed to the latest PDG report. All tagging parameters are fixed to the central values found in the tagging calibration, described in Sec. 5. Due to the fact that the $B_s^0 \rightarrow D_s \pi\pi\pi$ decay is flavour specific, the CP-coefficients can be fixed to $C = 1$ and $D_f = D_{\bar{f}} = S_f = S_{\bar{f}} = 0$, reducing Eq. 2.6 to

$$\int P(x, t, q_t, q_f) dx = [\cosh\left(\frac{\Delta\Gamma t}{2}\right) + q_t q_f C \cos(m_s t)] e^{-\Gamma t}. \quad (9.2)$$

Note that in this case, the dependence on the coherence factor κ is dropped and the same relation as found for $B_s^0 \rightarrow D_s \pi$ decays is recovered. Therefore, the only free fit parameter left is Δm_s . The data distribution with the overlaid fit is shown in Fig. xXx and the obtained value for the mixing frequency is

$$\Delta m_s = xx.xxx \pm 0.yyy. \quad (9.3)$$

9.2 sFit to $B_s^0 \rightarrow D_s K\pi\pi$ data

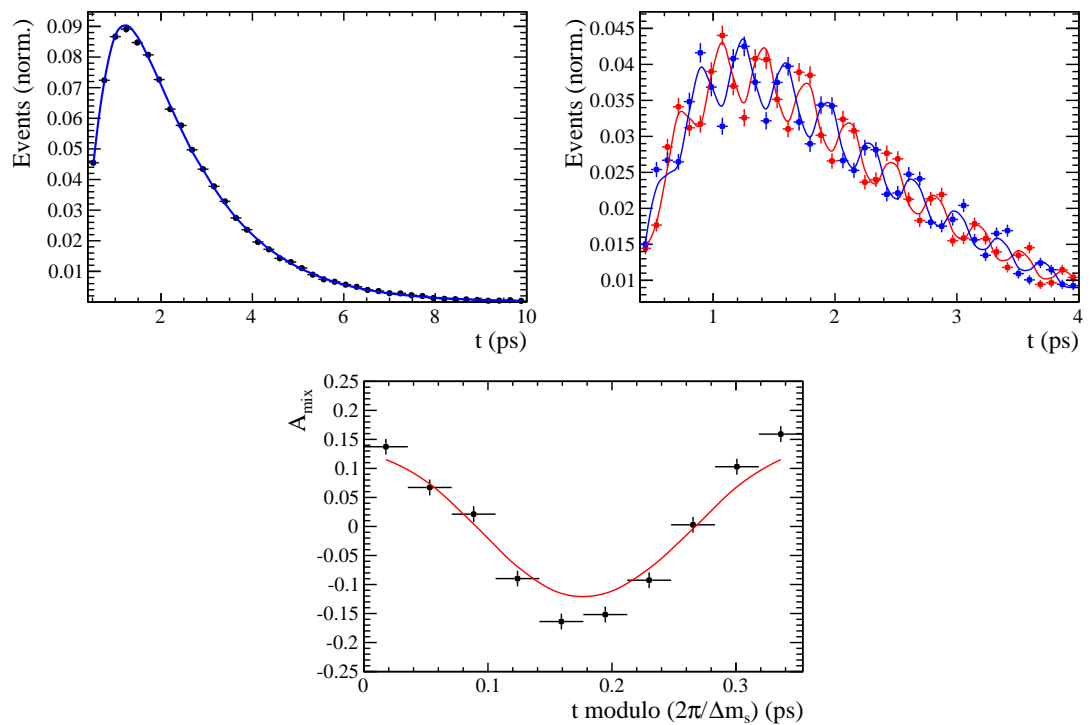


Figure 9.1

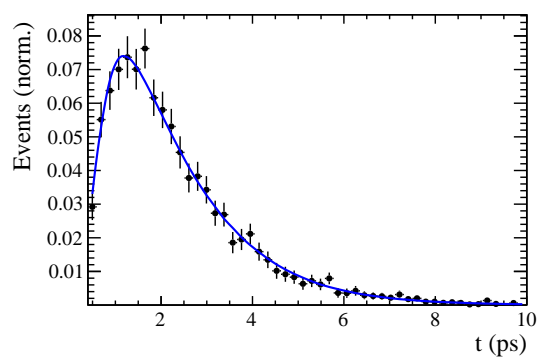


Figure 9.2

720 10 Time dependent amplitude fit

721 10.1 Signal Model Construction

722 The light meson spectrum comprises multiple resonances which are expected to contribute
 723 to $B_s \rightarrow D_s K\pi\pi$ decays as intermediate states. Apart from clear contributions coming
 724 from resonances such as $K_1(1270)$, $K_1(1400)$ $\rho(770)$ and $K^*(892)^0$, the remaining structure
 725 is impossible to infer due to the cornucopia of broad, overlapping and interfering resonances
 726 within the phase space boundary. The complete list of considered amplitudes can be
 727 found in Appendix E.

728 To build the amplitude model, one could successively add amplitudes on top of one
 729 another until a reasonable agreement between data and fit was achieved. However, this
 730 step-wise approach is not particularly suitable for amplitude analyses as discussed in
 731 Ref. [43]. Instead, we include the whole pool of amplitudes in the first instance and use
 732 the Least Absolute Shrinkage and Selection Operator [43, 44] (LASSO) approach to limit
 733 the model complexity. In this method, the event likelihood is extended by a penalty term

$$-2 \log \mathcal{L} \rightarrow -2 \log \mathcal{L} + \lambda \sum_i \sqrt{\int |a_i A_i(\mathbf{x})|^2 d\Phi_4}, \quad (10.1)$$

734 which shrinks the amplitude coefficients towards zero. The amount of shrinkage is
 735 controlled by the parameter λ , to be tuned on data. Higher values for λ encourage sparse
 736 models, *i.e.* models with only a few non-zero amplitude coefficients. The optimal value
 737 for λ is found by minimizing the Bayesian information criteria [45] (BIC),

$$BIC(\lambda) = -2 \log \mathcal{L} + r \log N_{\text{Sig}}, \quad (10.2)$$

738 where N_{Sig} is the number of signal events and r is the number of amplitudes with a decay
 739 fraction above a certain threshold. In this way, the optimal λ balances the fit quality
 740 ($-2 \log \mathcal{L}$) against the model complexity. The LASSO penalty term is only used to select
 741 the model. Afterwards, this term must be discarded in the final amplitude fit with the
 742 selected model, otherwise the parameter uncertainties would be biased.

743 The set of amplitudes is selected using the optimal value of $\lambda = 28$, and is henceforth
 744 called the LASSO model; Figure ??(a) shows the distribution of BIC values obtained by
 745 scanning over λ where we choose the decay fraction threshold to be 0.5%. In addition, we
 746 repeated the model selection procedure under multiple different conditions:

- 747 1. The fit fraction threshold for inclusion in the final model was varied within the
 748 interval [0.05, 5]%. The set of selected amplitudes is stable for thresholds between
 749 0.1% and 1%. Other choices result in marginally different models containing one
 750 component more or less.
 - 751 2. Instead of BIC, the Akaike information criteria ($AIC(\lambda) = -2 \log \mathcal{L} + 2r$ [46]) was
 752 used to optimize λ . For a given threshold, the AIC method tends to prefer lower
 753 λ values. However, the set of models obtained varying the threshold within the
 754 interval [0.05, 5]% is identical to the BIC method.
 - 755 3. The amplitudes selected under nominal conditions were excluded one-by-one from
 756 the set of all amplitudes considered.
- 757 From that we obtained a set of alternative models shown in Appendix ??.

758 **10.2 Results**

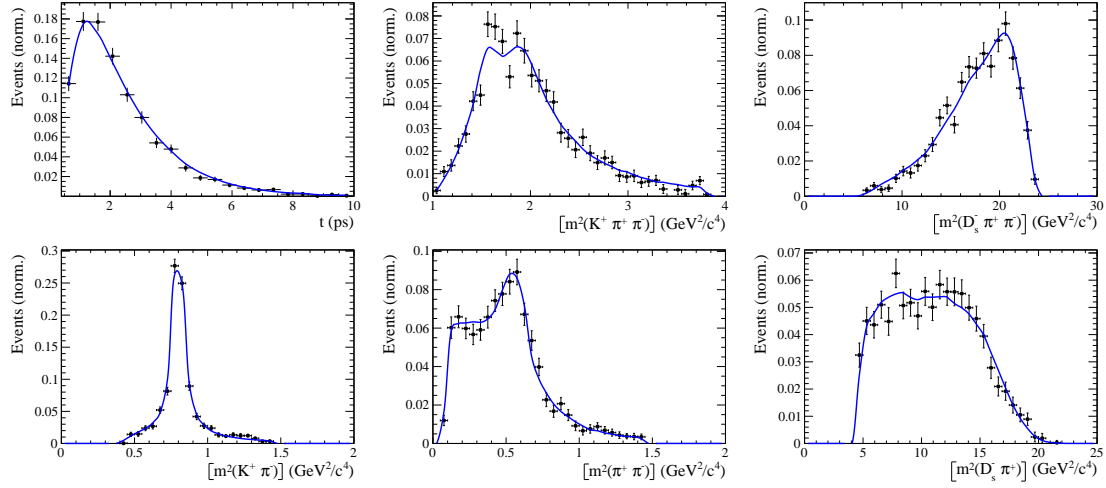


Figure 10.1

759 A Details of multivariate classifier

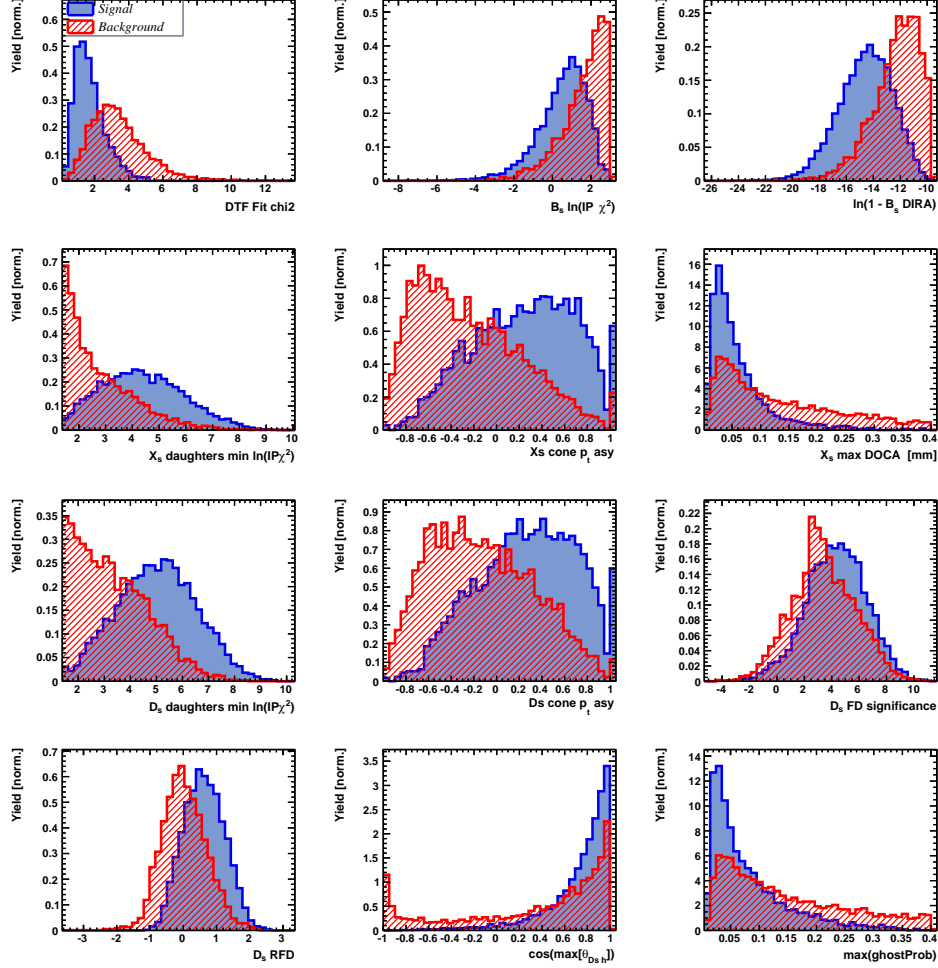


Figure A.1: Variables used to train the BDTG.

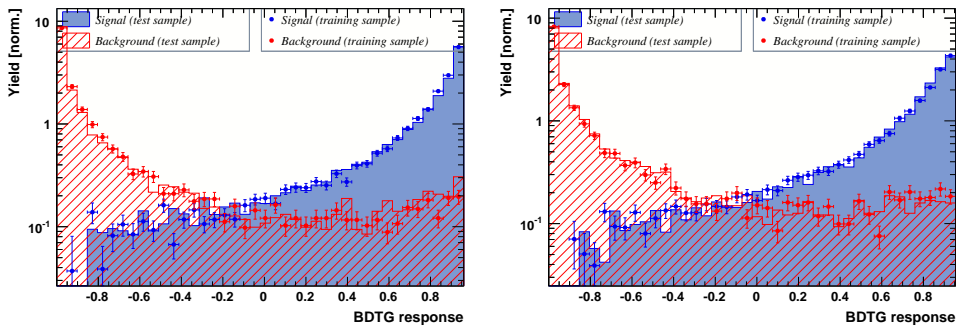


Figure A.2: Response of the classifier trained on the even (left) and odd (right) sample.

760 B Detailed mass fits

761 In this section, all fits to the mass distribution of $B_s^0 \rightarrow D_s\pi\pi\pi$ and $B_s^0 \rightarrow D_sK\pi\pi$
 762 candidates are shown. The fits are performed simultaneously in run period (Run-I, Run-
 763 II), D_s final state ($D_s \rightarrow KK\pi$ non-resonant, $D_s \rightarrow \phi\pi$, $D_s \rightarrow K^*K$, or $D_s \rightarrow \pi\pi\pi$) and
 764 L0 trigger category.

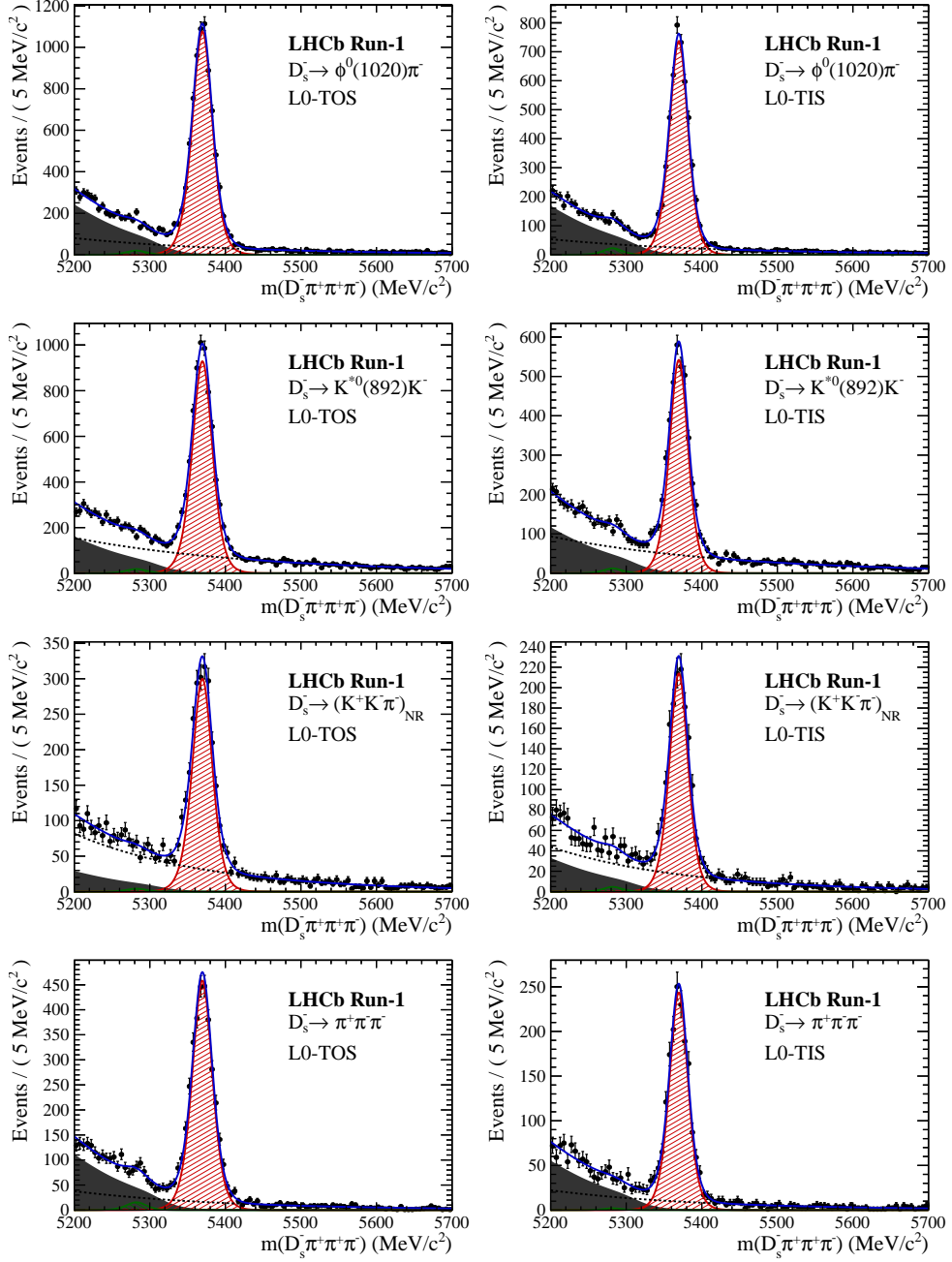


Figure B.1: Invariant mass distributions of $B_s^0 \rightarrow D_s\pi\pi\pi$ candidates for Run-I data.

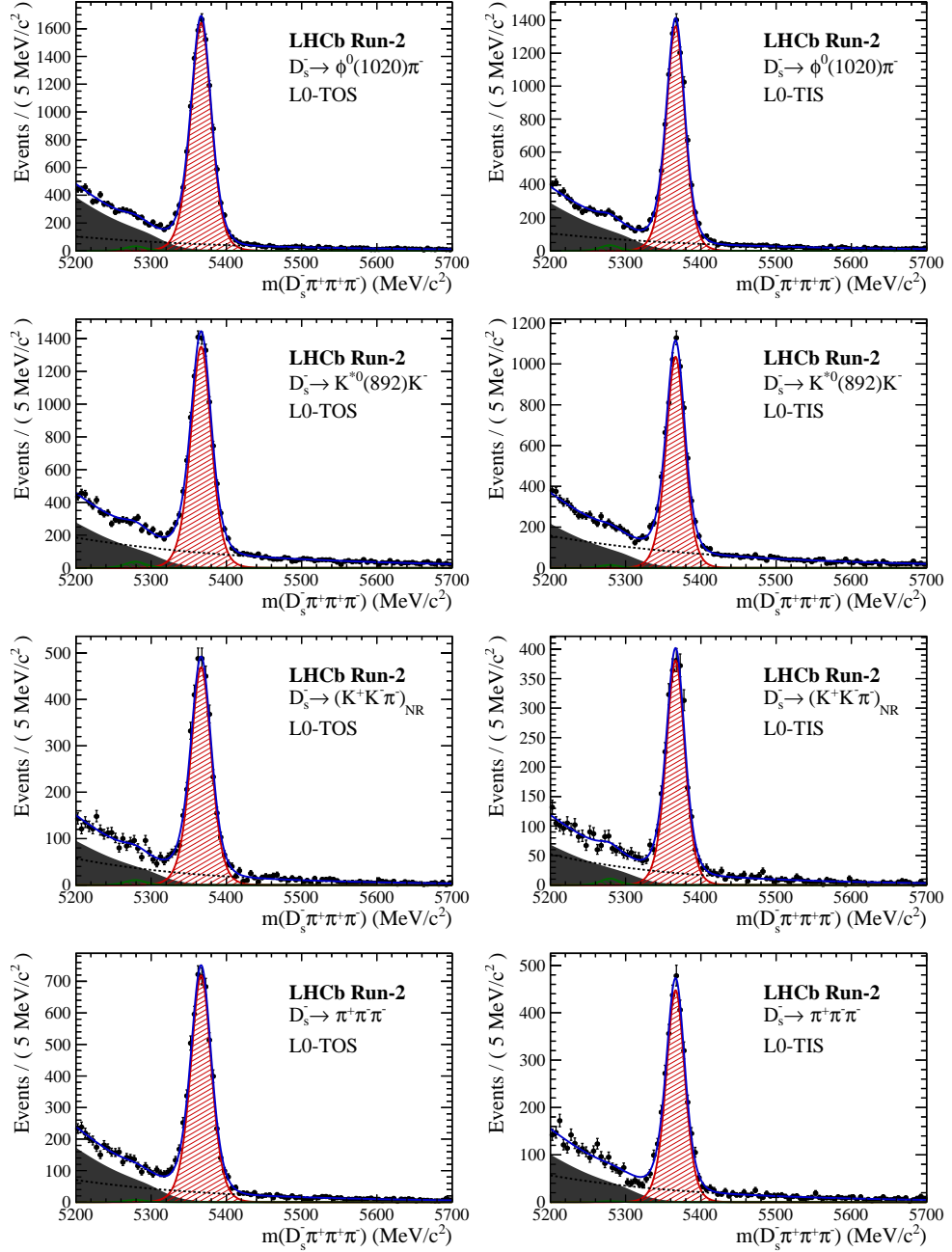


Figure B.2: Invariant mass distributions of $B_s^0 \rightarrow D_s\pi\pi\pi$ candidates for Run-II data.

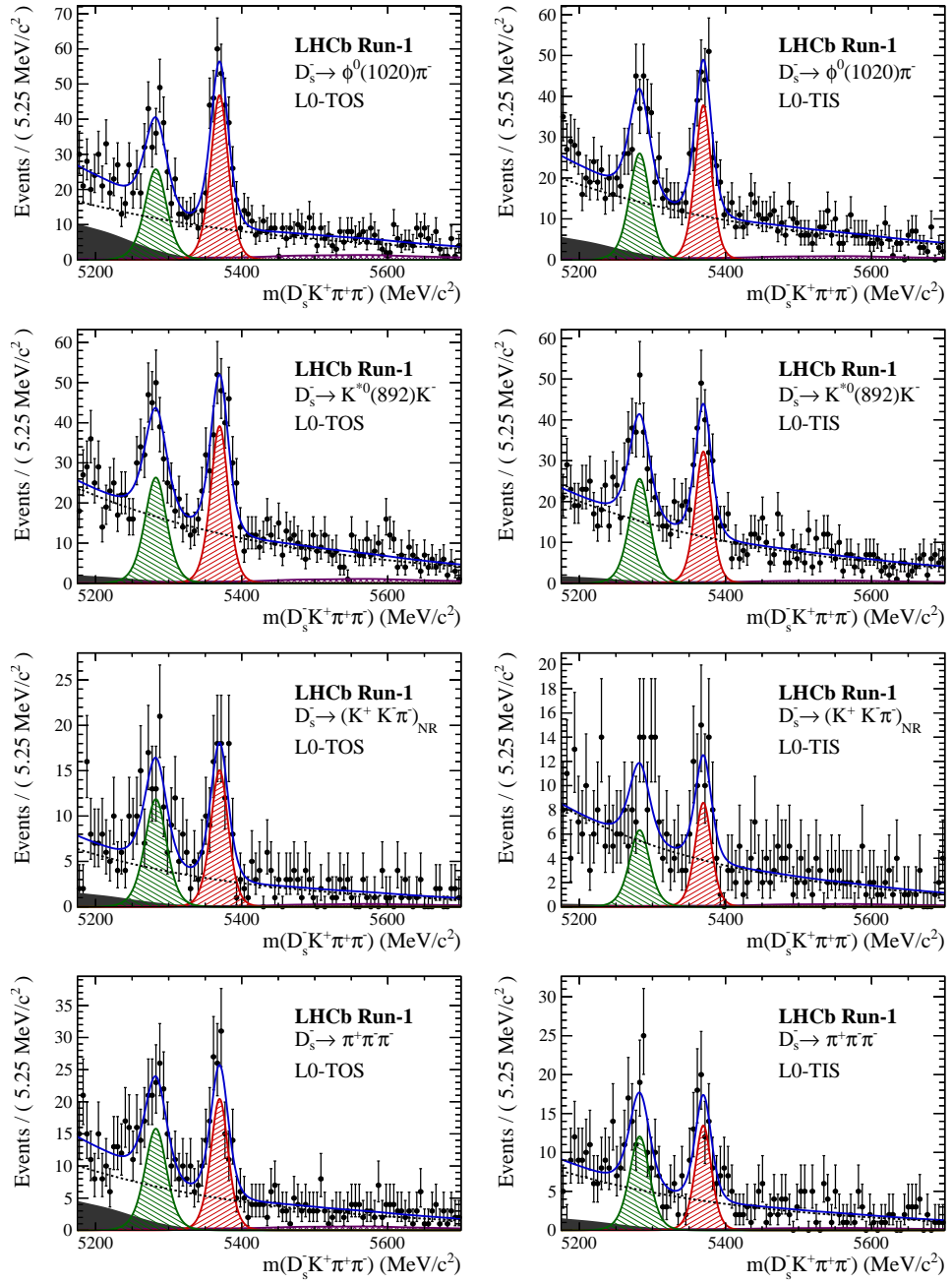


Figure B.3: Invariant mass distributions of $B_s^0 \rightarrow D_s K \pi \pi$ candidates for Run-I data.

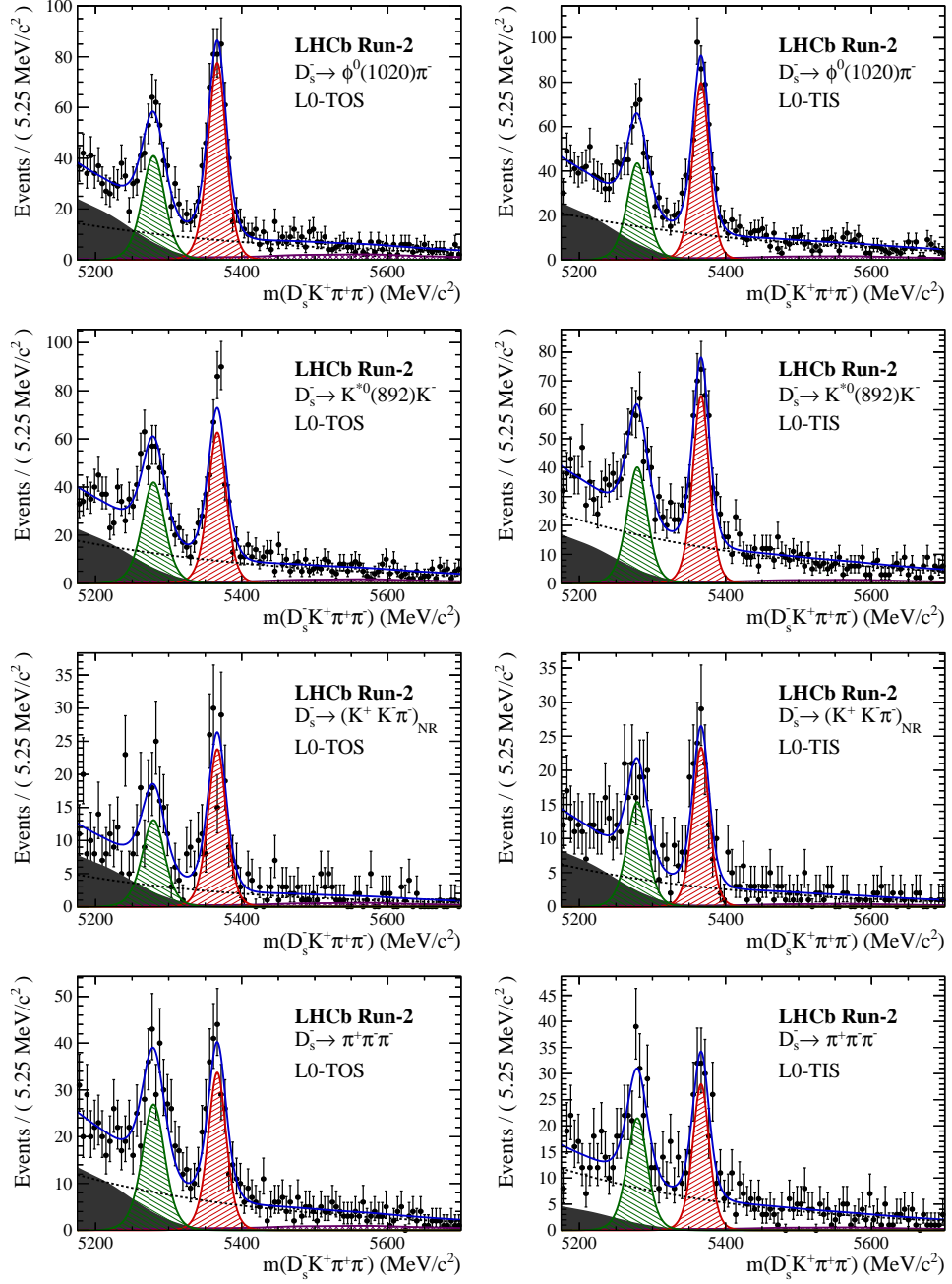


Figure B.4: Invariant mass distributions of $B_s^0 \rightarrow D_s K \pi \pi$ candidates for Run-II data.

765 C Decay-time Resolution fits

766 This section contains all fits to the distributions of the decay time difference Δt between
 767 the true and the reconstructed decay time of the truth-matched B_s^0 candidates on MC.
 768 The fits are performed in bins of the decay time error σ_t , where an adaptive binning
 769 scheme is used to ensure that approximately the same number of events are found in each
 770 bin.

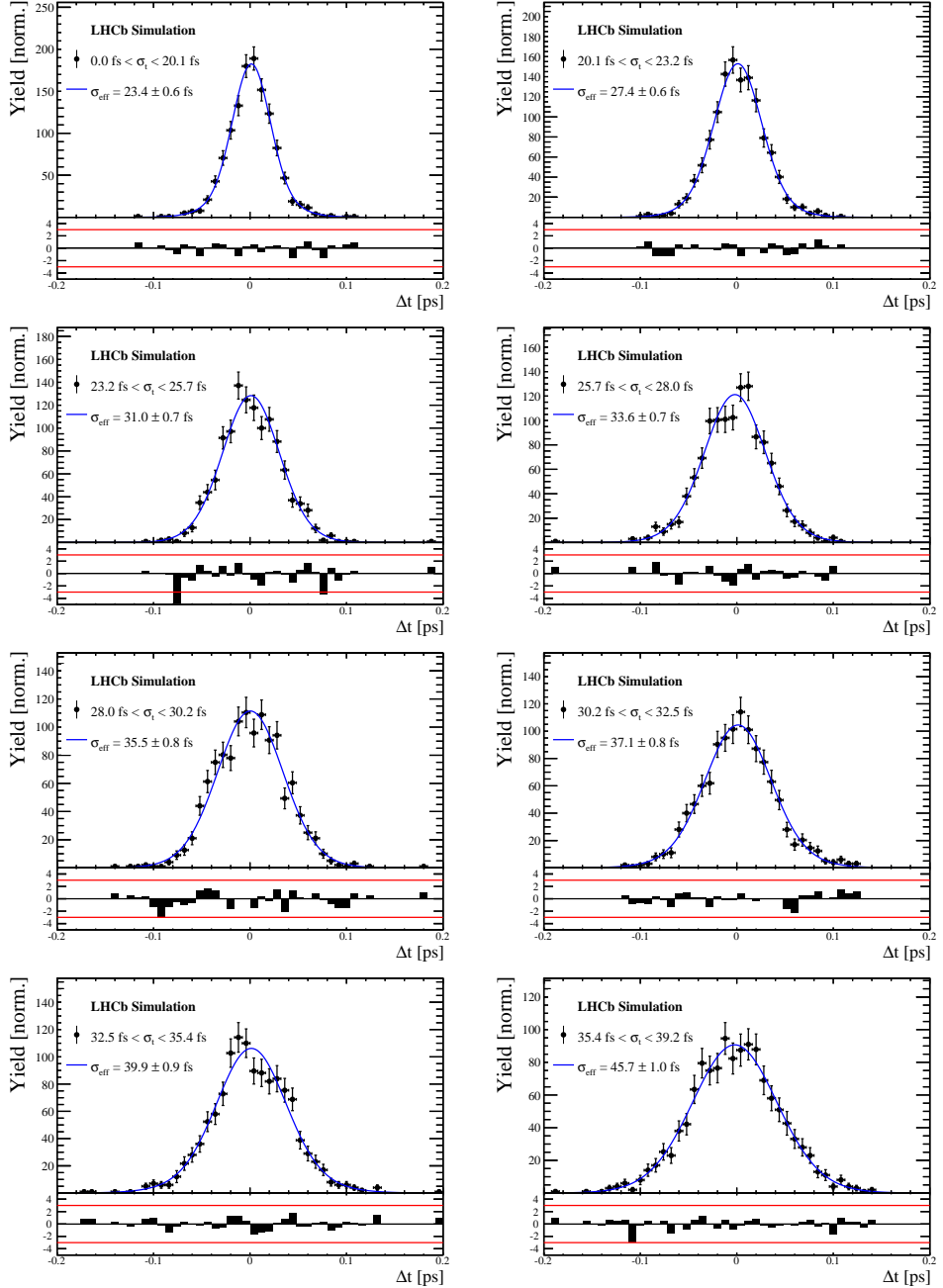


Figure C.1: Difference of the true and measured decay time of $B_s^0 \rightarrow D_s K\pi\pi$ MC candidates in bins of the per-event decay time error estimate..

σ_t Bin [fs]	σ_1 [fs]	σ_2 [fs]	f_1	D	σ_{eff} [fs]
0.0 - 20.1	19 ± 0.675	33.8 ± 1.77	0.75 ± 0	0.917 ± 0.00406	23.4 ± 0.599
20.1 - 23.2	23.4 ± 0.86	37.4 ± 1.95	0.75 ± 0	0.888 ± 0.00477	27.4 ± 0.621
23.2 - 25.7	28.1 ± 1.02	38.7 ± 2.32	0.75 ± 0	0.86 ± 0.00563	31 ± 0.671
25.7 - 28.0	30.1 ± 1.12	43.2 ± 2.56	0.75 ± 0	0.837 ± 0.00651	33.6 ± 0.734
28.0 - 30.2	32.4 ± 1.12	44.2 ± 2.59	0.75 ± 0	0.819 ± 0.00694	35.5 ± 0.756
30.2 - 32.5	32.6 ± 1.38	49.2 ± 3.04	0.75 ± 0	0.805 ± 0.00792	37.1 ± 0.841
32.5 - 35.4	34.4 ± 1.19	54.7 ± 2.85	0.75 ± 0	0.778 ± 0.0086	39.9 ± 0.879
35.4 - 39.2	41.9 ± 1.8	56.9 ± 4.18	0.75 ± 0	0.719 ± 0.00997	45.7 ± 0.962
39.2 - 44.7	42.2 ± 1.56	68.1 ± 4.01	0.75 ± 0	0.687 ± 0.0114	48.8 ± 1.08
44.7 - 120.0	55.5 ± 2.59	83 ± 14.7	0.75 ± 0	0.546 ± 0.0521	62 ± 4.89

Table 3.1: Measured time resolution for $B_s \rightarrow D_s K\pi\pi$ MC in bins of the per-event decay time error estimate.

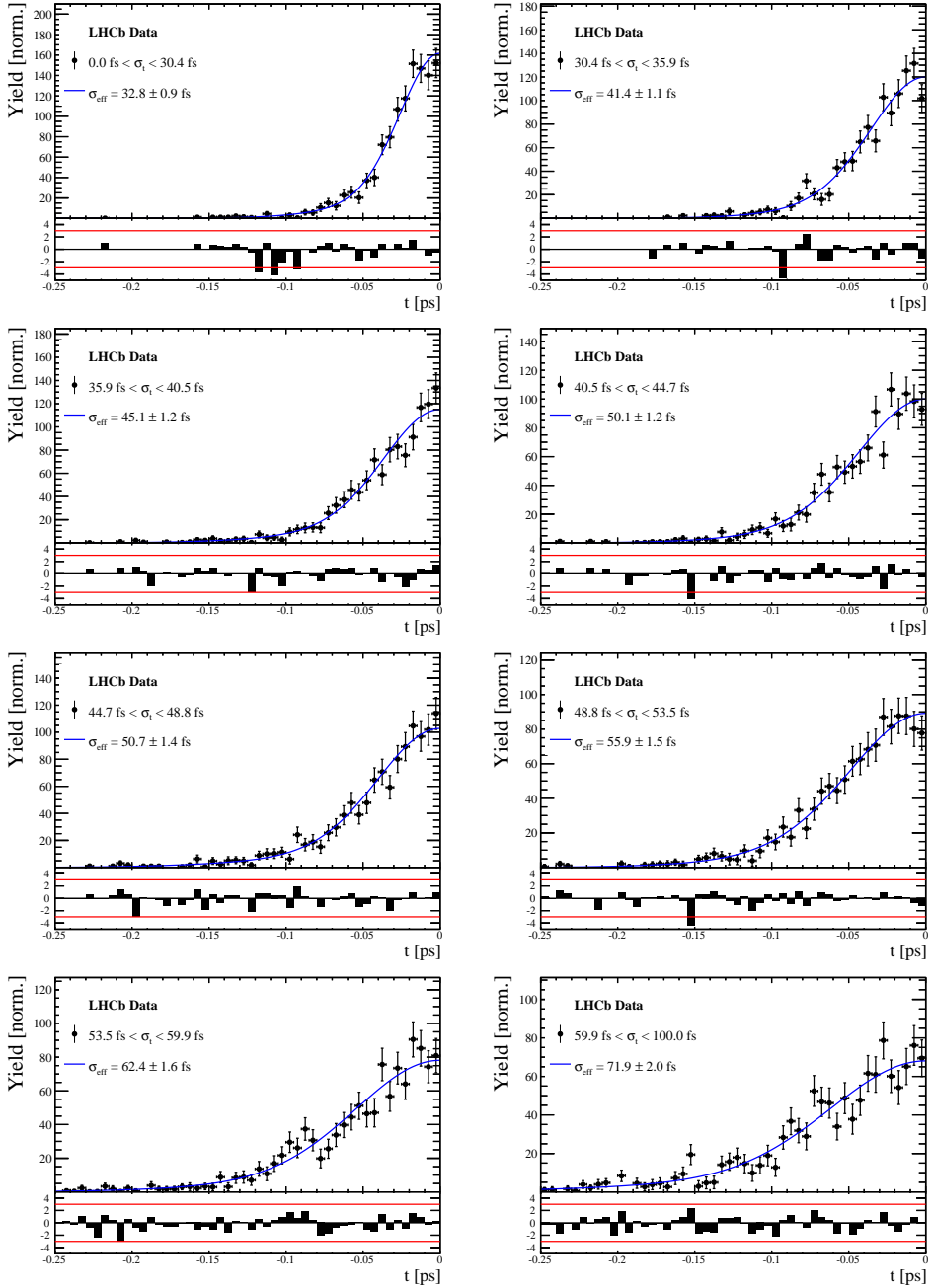


Figure C.2: Decay-time distribution for fake B_s candidates from promptly produced D_s candidates, combined with random prompt $K\pi\pi$ bachelor tracks, for bins in the per-event decay time error estimate.

σ_t Bin [fs]	σ_1 [fs]	σ_2 [fs]	f_1	D	σ_{eff} [fs]
0.0 - 30.4	25.4 ± 1.03	50.7 ± 2.77	0.75 ± 0	0.844 ± 0.00822	32.8 ± 0.942
30.4 - 35.9	34.5 ± 1.46	60.2 ± 3.48	0.75 ± 0	0.763 ± 0.0108	41.4 ± 1.08
35.9 - 40.5	35.6 ± 1.35	71.3 ± 3.84	0.75 ± 0	0.726 ± 0.0121	45.1 ± 1.18
40.5 - 44.7	42.3 ± 1.65	73.3 ± 4.21	0.75 ± 0	0.673 ± 0.0132	50.1 ± 1.24
44.7 - 48.8	39.6 ± 1.64	84.8 ± 5.07	0.75 ± 0	0.666 ± 0.0145	50.7 ± 1.36
48.8 - 53.5	47.6 ± 1.94	82.4 ± 5.48	0.75 ± 0	0.611 ± 0.0157	55.9 ± 1.46
53.5 - 59.9	53 ± 2.15	95.3 ± 6.84	0.75 ± 0	0.541 ± 0.0174	62.4 ± 1.63
59.9 - 100.0	60.5 ± 2.8	125 ± 14	0.75 ± 0	0.443 ± 0.0204	71.9 ± 2.03

Table 3.2: Measured time resolution for prompt- D_s data in bins of the per-event decay time error estimate.

771 D Spin Amplitudes

772 The spin factors used for $B \rightarrow P_1 P_2 P_3 P_4$ decays are given in Table 4.1.

Table 4.1: Spin factors for all topologies considered in this analysis. In the decay chains, S , P , V , A , T and PT stand for scalar, pseudoscalar, vector, axial vector, tensor and pseudotensor, respectively. If no angular momentum is specified, the lowest angular momentum state compatible with angular momentum conservation and, where appropriate, parity conservation, is used.

Number	Decay chain	Spin amplitude
1	$B \rightarrow (P P_1)$, $P \rightarrow (S P_2)$, $S \rightarrow (P_3 P_4)$	1
2	$B \rightarrow (P P_1)$, $P \rightarrow (V P_2)$, $V \rightarrow (P_3 P_4)$	$L_{(1)\alpha}(P) L_{(1)}^\alpha(V)$
3	$B \rightarrow (A P_1)$, $A \rightarrow (V P_2)$, $V \rightarrow (P_3 P_4)$	$L_{(1)\alpha}(B) P_{(1)}^{\alpha\beta}(A) L_{(1)\beta}(V)$
4	$B \rightarrow (A P_1)$, $A[D] \rightarrow (P_2 V)$, $V \rightarrow (P_3 P_4)$	$L_{(1)\alpha}(B) L_{(2)}^{\alpha\beta}(A) L_{(1)\beta}(V)$
5	$B \rightarrow (A P_1)$, $A \rightarrow (S P_2)$, $S \rightarrow (P_3 P_4)$	$L_{(1)\alpha}(B) L_{(1)}^\alpha(A)$
6	$B \rightarrow (A P_1)$, $A \rightarrow (T P_2)$, $T \rightarrow (P_3 P_4)$	$L_{(1)\alpha}(B) L_{(1)\beta}(A) L_{(2)}^{\alpha\beta}(T)$
7	$B \rightarrow (V_1 P_1)$, $V_1 \rightarrow (V_2 P_2)$, $V_2 \rightarrow (P_3 P_4)$	$L_{(1)\mu}(B) P_{(1)}^{\mu\alpha}(V_1) \epsilon_{\alpha\beta\gamma\delta} L_{(1)}^\beta(V_1) p_{V_1}^\gamma L_{(1)}^\delta(V_2)$
8	$B \rightarrow (PT P_1)$, $PT \rightarrow (V P_2)$, $V \rightarrow (P_3 P_4)$	$L_{(2)\alpha\beta}(B) P_{(2)}^{\alpha\beta\gamma\delta}(PT) L_{(1)\gamma}(PT) L_{(1)\delta}(V)$
9	$B \rightarrow (PT P_1)$, $PT \rightarrow (S P_2)$, $S \rightarrow (P_3 P_4)$	$L_{(2)\alpha\beta}(B) L_{(2)}(PT)^{\alpha\beta}$
10	$B \rightarrow (PT P_1)$, $PT \rightarrow (T P_2)$, $T \rightarrow (P_3 P_4)$	$L_{(2)\alpha\beta}(B) P_{(2)}^{\alpha\beta\gamma\delta}(PT) L_{(2)\gamma\delta}(T)$
11	$B \rightarrow (T P_1)$, $T \rightarrow (V P_2)$, $V \rightarrow (P_3 P_4)$	$L_{(2)\mu\nu}(B) P_{(2)}^{\mu\nu\rho\alpha}(T) \epsilon_{\alpha\beta\gamma\delta} L_{(2)\rho}^\beta(T) p_T^\gamma P_{(1)}^{\delta\sigma}(T) L_{(1)\sigma}(V)$
12	$B \rightarrow (T_1 P_1)$, $T_1 \rightarrow (T_2 P_2)$, $T_2 \rightarrow (P_3 P_4)$	$L_{(2)\mu\nu}(B) P_{(2)}^{\mu\nu\rho\alpha}(T_1) \epsilon_{\alpha\beta\gamma\delta} L_{(1)}^\beta(T_1) p_{T_1}^\gamma L_{(2)\rho}^\delta(T_2)$
13	$B \rightarrow (S_1 S_2)$, $S_1 \rightarrow (P_1 P_2)$, $S_2 \rightarrow (P_3 P_4)$	1
14	$B \rightarrow (V S)$, $V \rightarrow (P_1 P_2)$, $S \rightarrow (P_3 P_4)$	$L_{(1)\alpha}(B) L_{(1)}^\alpha(V)$
15	$B \rightarrow (V_1 V_2)$, $V_1 \rightarrow (P_1 P_2)$, $V_2 \rightarrow (P_3 P_4)$	$L_{(1)\alpha}(V_1) L_{(1)}^\alpha(V_2)$
16	$B[P] \rightarrow (V_1 V_2)$, $V_1 \rightarrow (P_1 P_2)$, $V_2 \rightarrow (P_3 P_4)$	$\epsilon_{\alpha\beta\gamma\delta} L_{(1)}^\alpha(B) L_{(1)}^\beta(V_1) L_{(1)}^\gamma(V_2) p_B^\delta$
17	$B[D] \rightarrow (V_1 V_2)$, $V_1 \rightarrow (P_1 P_2)$, $V_2 \rightarrow (P_3 P_4)$	$L_{(2)\alpha\beta}(B) L_{(1)}^\alpha(V_1) L_{(1)}^\beta(V_2)$
18	$B \rightarrow (T S)$, $T \rightarrow (P_1 P_2)$, $S \rightarrow (P_3 P_4)$	$L_{(2)\alpha\beta}(B) L_{(2)}^{\alpha\beta}(T)$
19	$B \rightarrow (V T)$, $T \rightarrow (P_1 P_2)$, $V \rightarrow (P_3 P_4)$	$L_{(1)\alpha}(B) L_{(2)}^{\alpha\beta}(T) L_{(1)\beta}(V)$
20	$B[D] \rightarrow (TV)$, $T \rightarrow (P_1 P_2)$, $V \rightarrow (P_3 P_4)$	$\epsilon_{\alpha\beta\delta\gamma} L_2^{\alpha\mu}(B) L_{2\mu}^\beta L_{(1)}^\gamma(V) p_B^\delta$
21	$B \rightarrow (T_1 T_2)$, $T_1 \rightarrow (P_1 P_2)$, $T_2 \rightarrow (P_3 P_4)$	$L_{(2)\alpha\beta}(T_1) L_{(2)}^{\alpha\beta}(T_2)$
22	$B[P] \rightarrow (T_1 T_2)$, $T_1 \rightarrow (P_1 P_2)$, $T_2 \rightarrow (P_3 P_4)$	$\epsilon_{\alpha\beta\gamma\delta} L_{(1)}^\alpha(B) L_{(2)}^{\beta\mu}(T_1) L_{(2)\mu}^\gamma(T_2) p_B^\delta$
23	$B[D] \rightarrow (T_1 T_2)$, $T_1 \rightarrow (P_1 P_2)$, $T_2 \rightarrow (P_3 P_4)$	$L_{(2)\alpha\beta}(B) L_{(2)}^{\alpha\gamma}(T_1) L_{(2)\gamma}^\beta(T_2)$

773 E Considered Decay Chains

774 The various decay channels considered in the model building are listed in Table 5.1.

Table 5.1: Decays considered in the LASSO model building.

Decay channel
$B_s \rightarrow D_s^- [K_1(1270)^+ [S, D] \rightarrow \pi^+ K^*(892)^0]$
$B_s \rightarrow D_s^- [K_1(1270)^+ \rightarrow \pi^+ K^*(1430)^0]$
$B_s \rightarrow D_s^- [K_1(1270)^+ [S, D] \rightarrow K^+ \rho(770)^0]$
$B_s \rightarrow D_s^- [K_1(1270)^+ [S, D] \rightarrow K^+ \omega(782)]$
$B_s \rightarrow D_s^- [K_1(1400)^+ [S, D] \rightarrow \pi^+ K^*(892)^0]$
$B_s \rightarrow D_s^- [K_1(1400)^+ [S, D] \rightarrow K^+ \rho(770)^0]$
$B_s \rightarrow D_s^- [K(1460)^+ \rightarrow \pi^+ \kappa]$
$B_s \rightarrow D_s^- [K(1460)^+ \rightarrow K^+ \sigma]$
$B_s \rightarrow D_s^- [K(1460)^+ \rightarrow \pi^+ K^*(892)^0]$
$B_s \rightarrow D_s^- [K(1460)^+ \rightarrow K^+ \rho(770)^0]$
$B_s \rightarrow D_s^- [K^*(1410)^+ \rightarrow \pi^+ K^*(892)^0]$
$B_s \rightarrow D_s^- [K^*(1410)^+ \rightarrow K^+ \rho(770)^0]$
$B_s \rightarrow D_s^- [K_2^*(1430)^+ \rightarrow \pi^+ K^*(892)^0]$
$B_s \rightarrow D_s^- [K_2^*(1430)^+ \rightarrow K^+ \rho(770)^0]$
$B_s \rightarrow D_s^- [K^*(1680)^+ \rightarrow \pi^+ K^*(892)^0]$
$B_s \rightarrow D_s^- [K^*(1680)^+ \rightarrow K^+ \rho(770)^0]$
$B_s \rightarrow D_s^- [K_2(1770)^+ \rightarrow \pi^+ K^*(892)^0]$
$B_s \rightarrow D_s^- [K_2(1770)^+ \rightarrow K^+ \rho(770)^0]$
$B_s \rightarrow \sigma^0 (D_s^- K^+)_S$
$B_s [S, P, D] \rightarrow \sigma^0 (D_s^- K^+)_V$
$B_s \rightarrow \rho(770)^0 (D_s^- K^+)_S$
$B_s [S, P, D] \rightarrow \rho(770)^0 (D_s^- K^+)_V$
$B_s \rightarrow K^*(892)^0 (D_s^- \pi^+)_S$
$B_s [S, P, D] \rightarrow K^*(892)^0 (D_s^- \pi^+)_V$
$B_s \rightarrow (D_s^- K^+)_S (\pi^+ \pi^-)_S$

775 F MC corrections

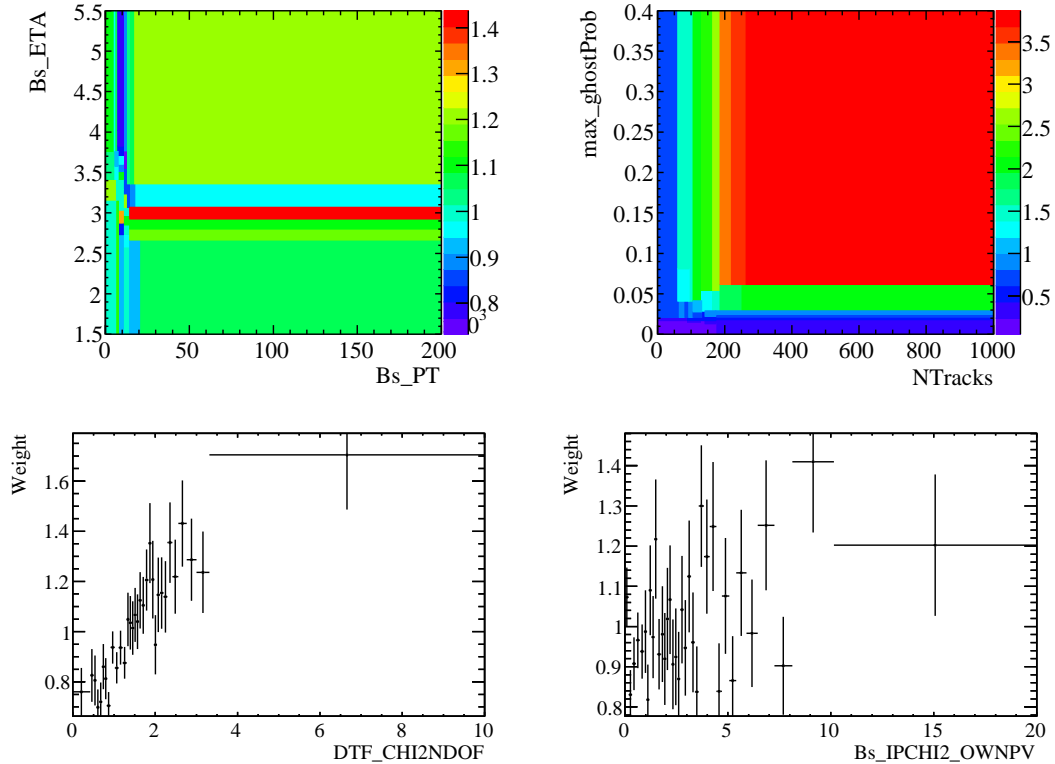


Figure C.1: Weights applied to correct for Data/MC differences.

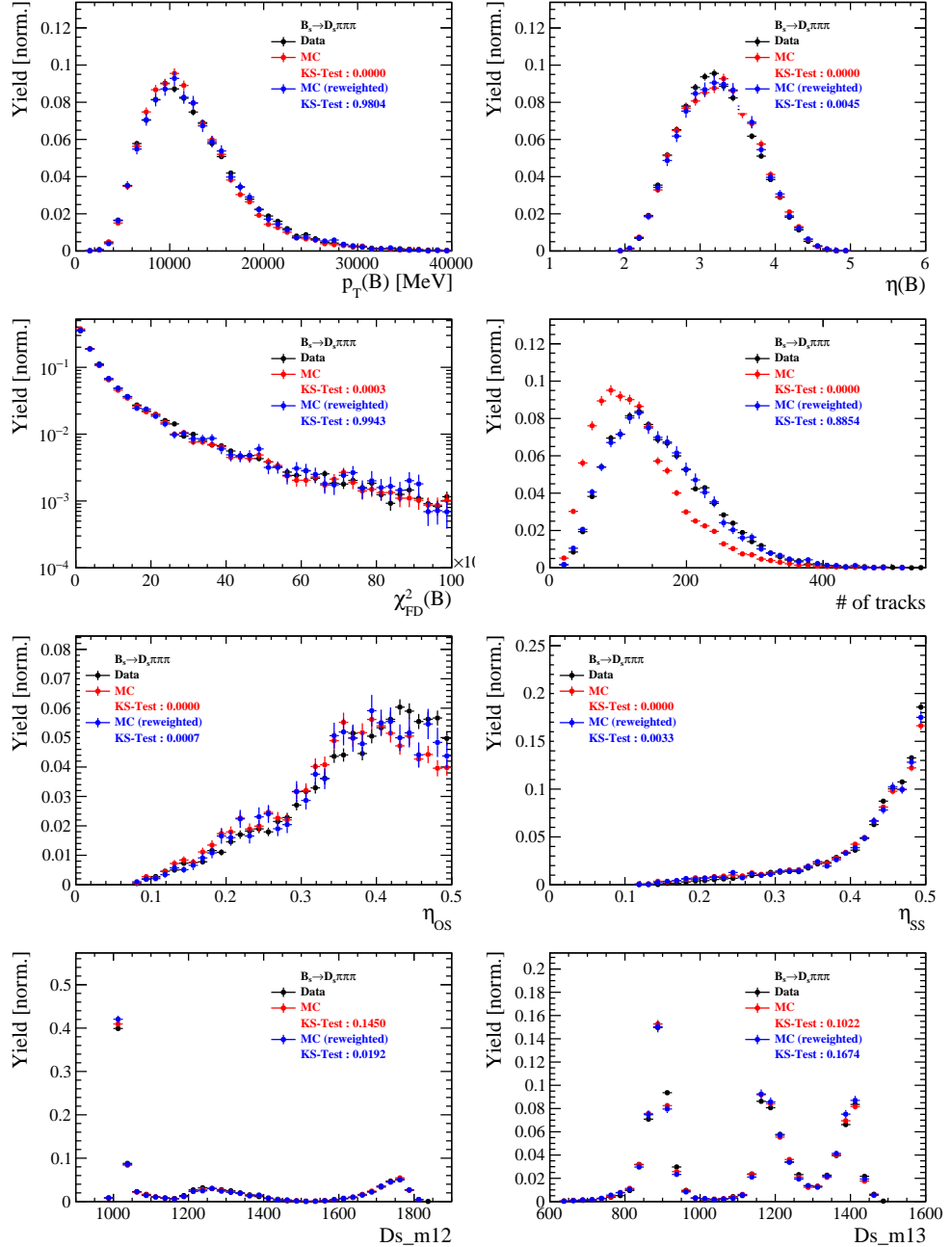


Figure C.2: Comparison of selected variables for $B_s \rightarrow D_s \pi\pi\pi$ decays.

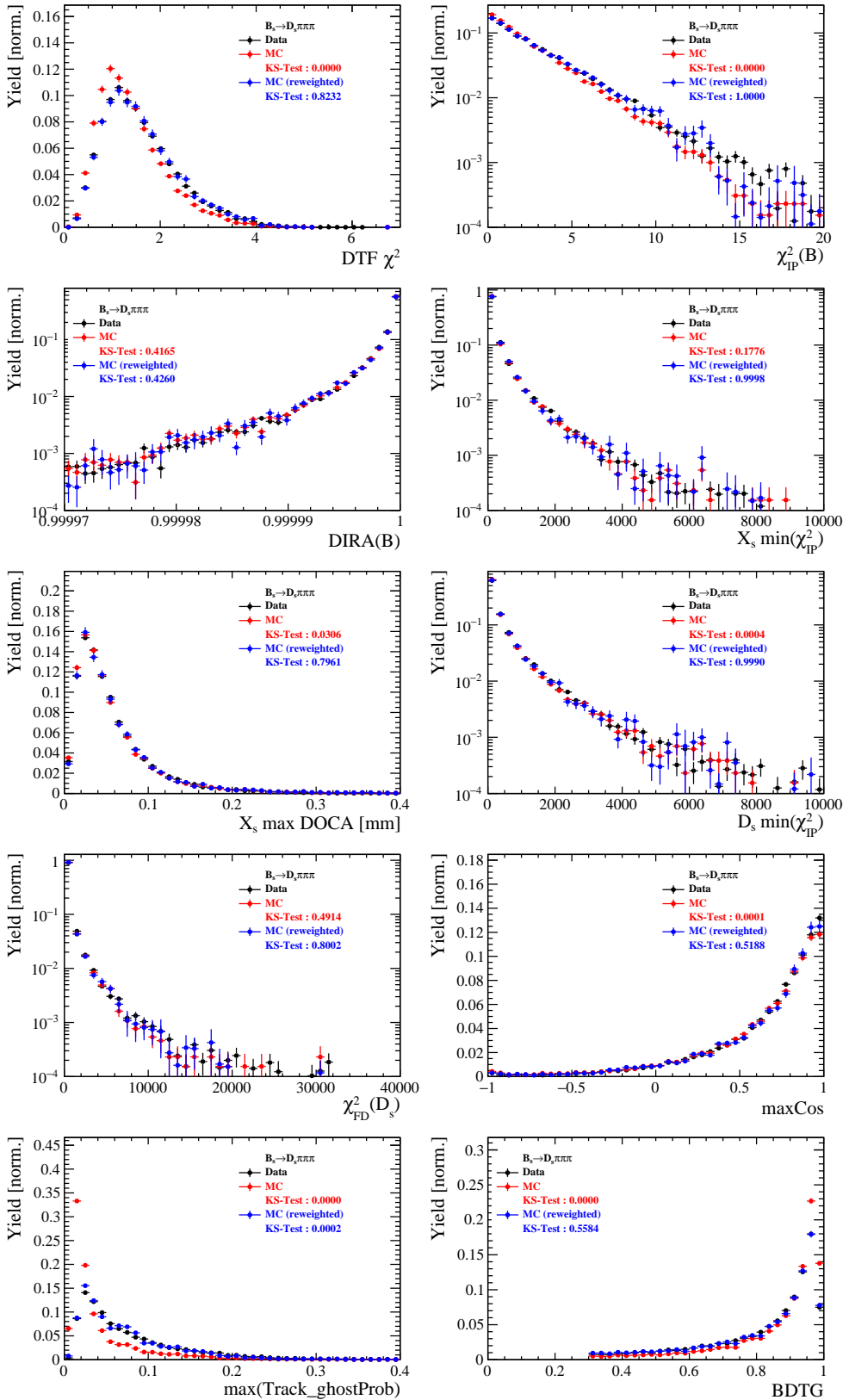


Figure C.3: Comparison of BDTG input variables and classifier response for $B_s \rightarrow D_s \pi\pi\pi$ decays.

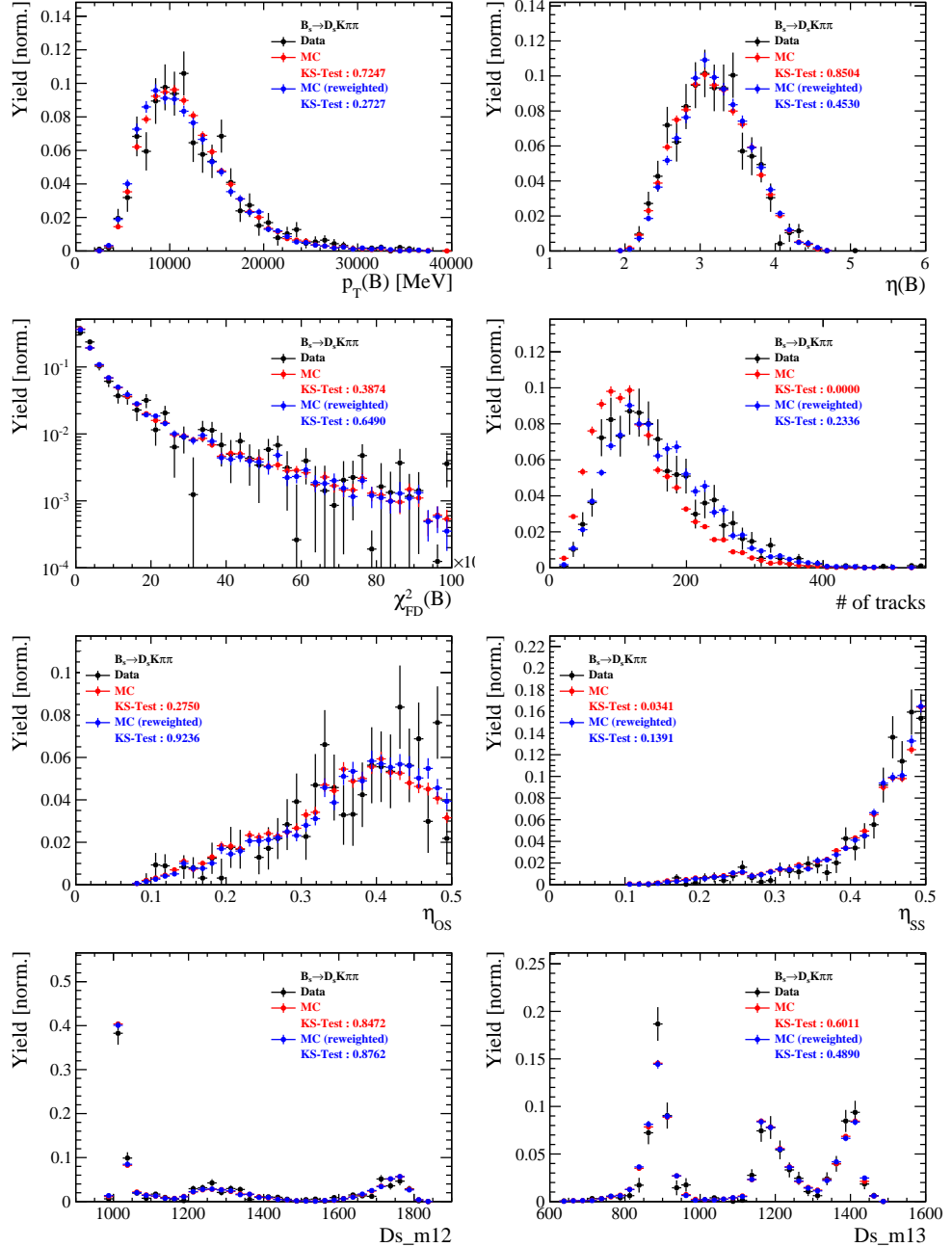


Figure C.4: Comparison of selected variables for $B_s \rightarrow D_s K\pi\pi$ decays.

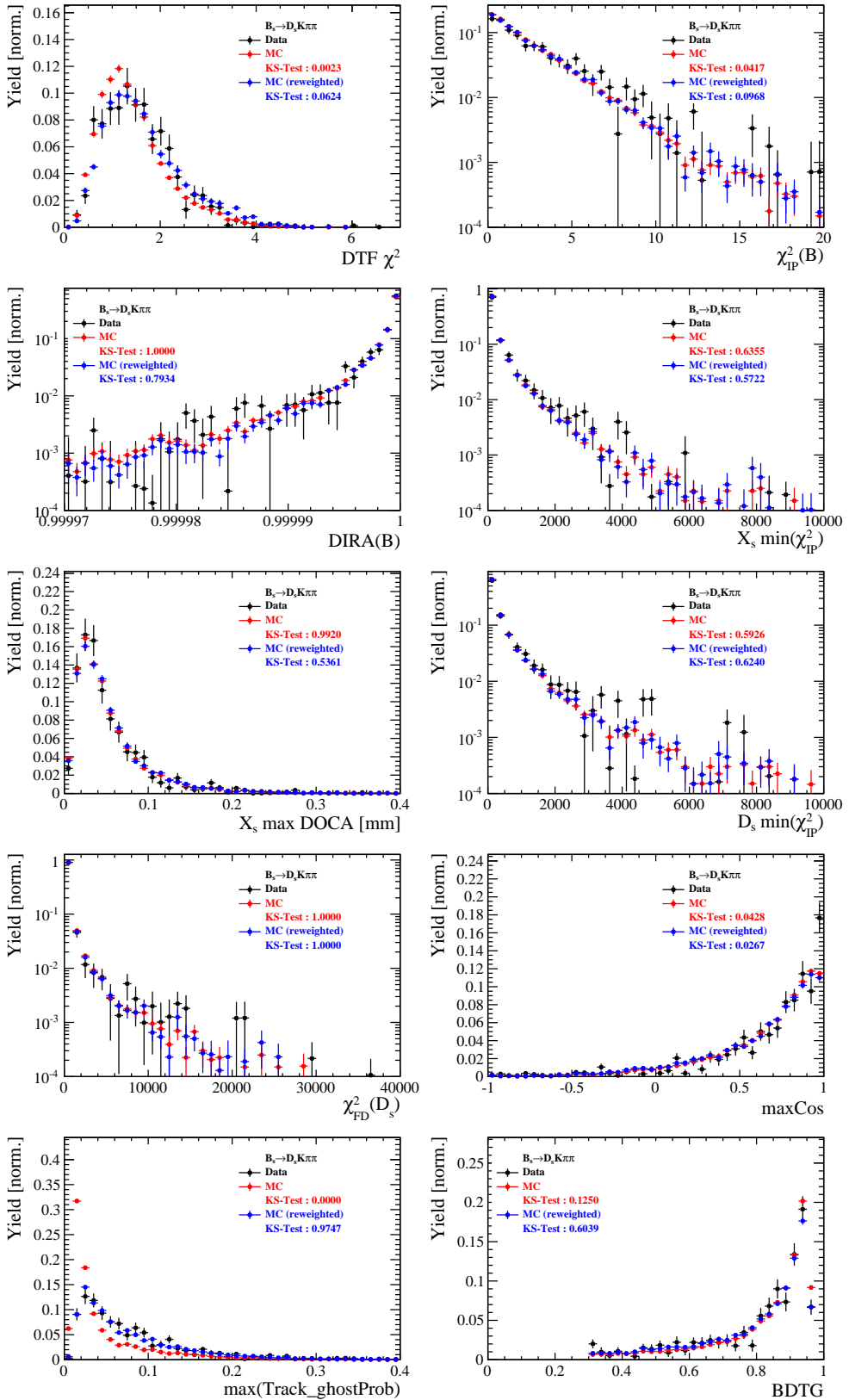


Figure C.5: Comparison of BDTG input variables and classifier response for $B_s \rightarrow D_s K\pi\pi$ decays.

776 **G Data distributions**

777 **G.1 Comparison of signal and calibration channel**

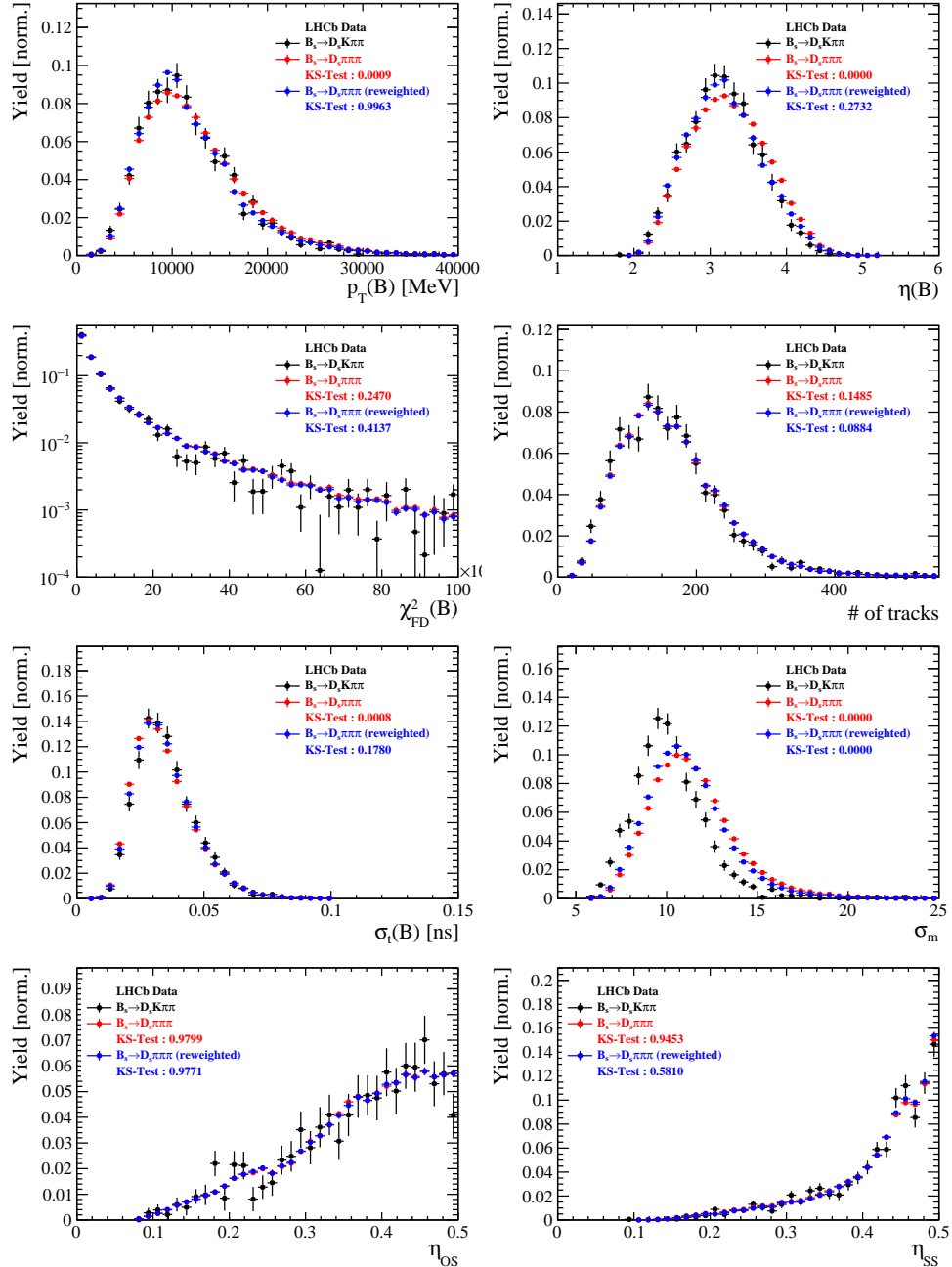


Figure C.1: Comparison of selected variables.

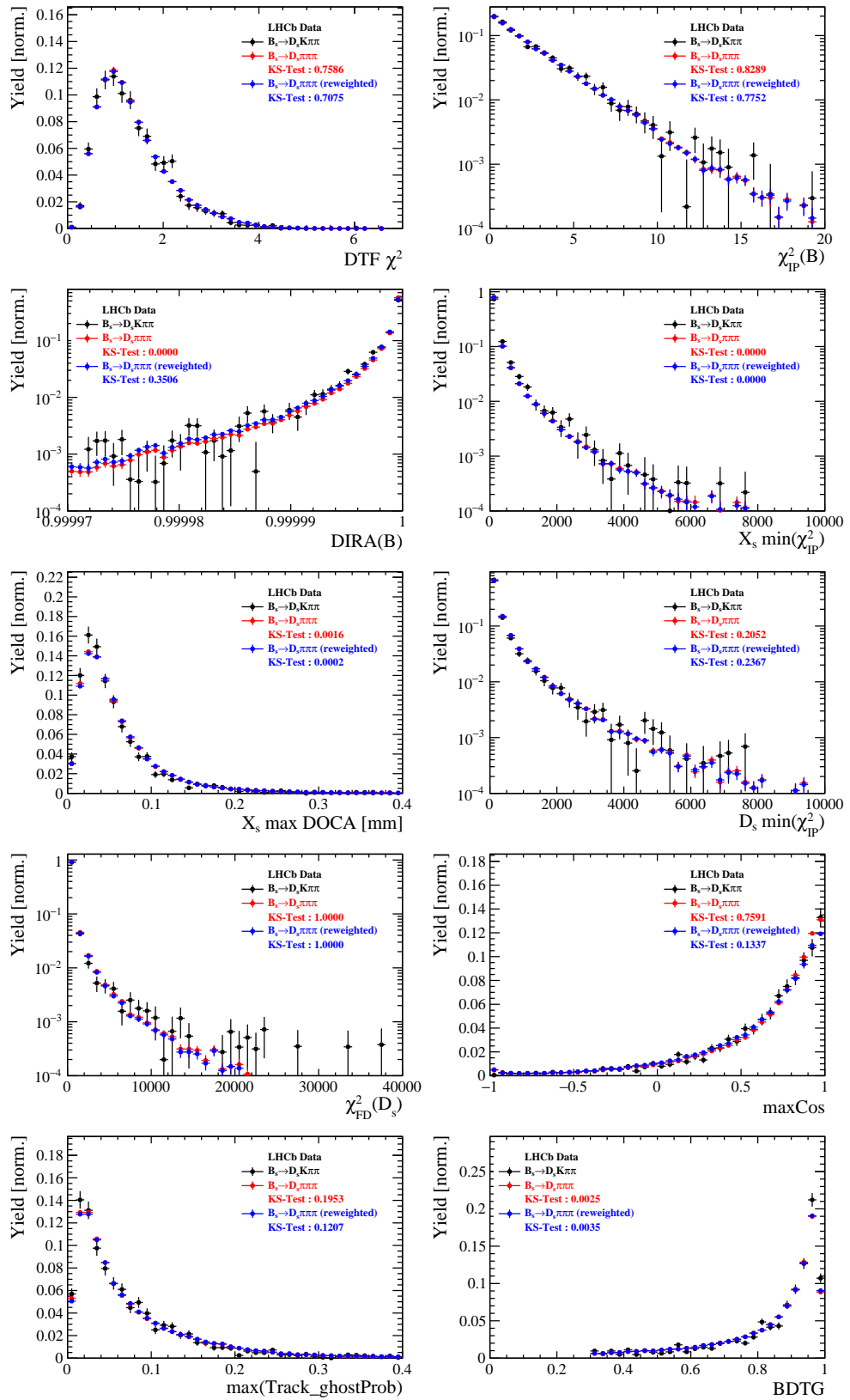


Figure C.2: Comparison of BDTG input variables and classifier response.

778 G.2 Comparison of Run-I and Run-II data

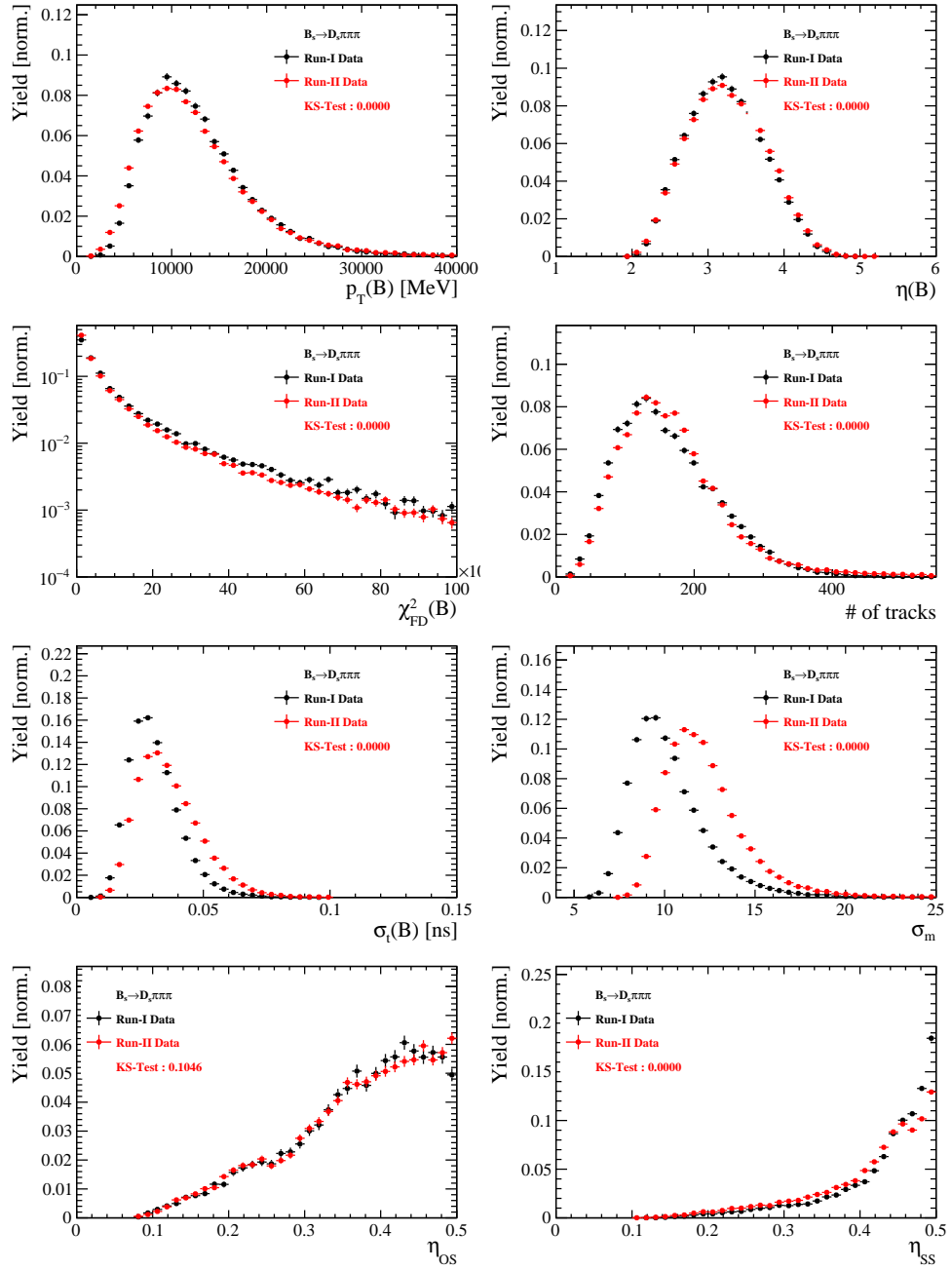


Figure C.3: Comparison of selected variables.

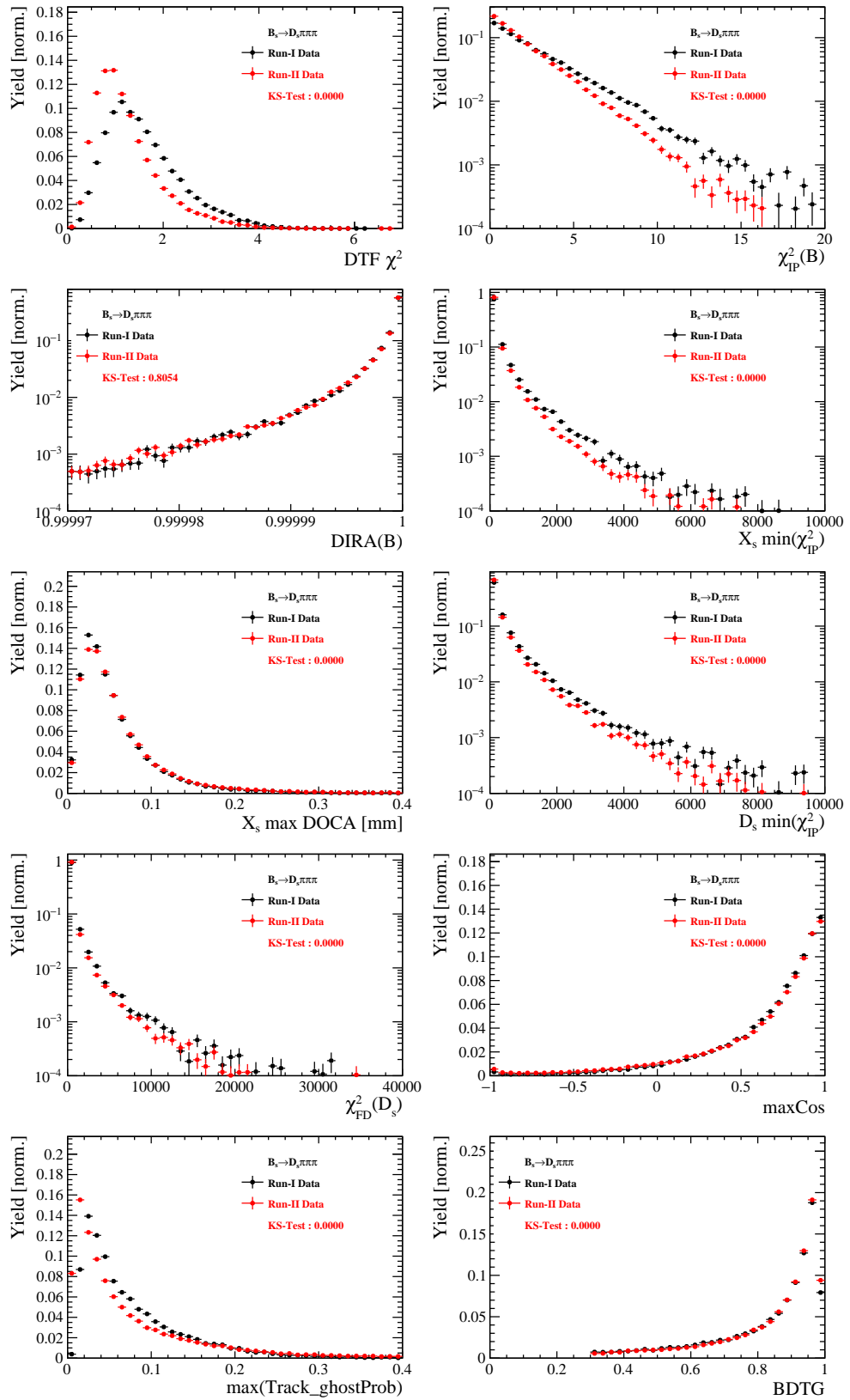


Figure C.4: Comparison of BDTG input variables and classifier response.

779 G.3 Comparison of D_s final states

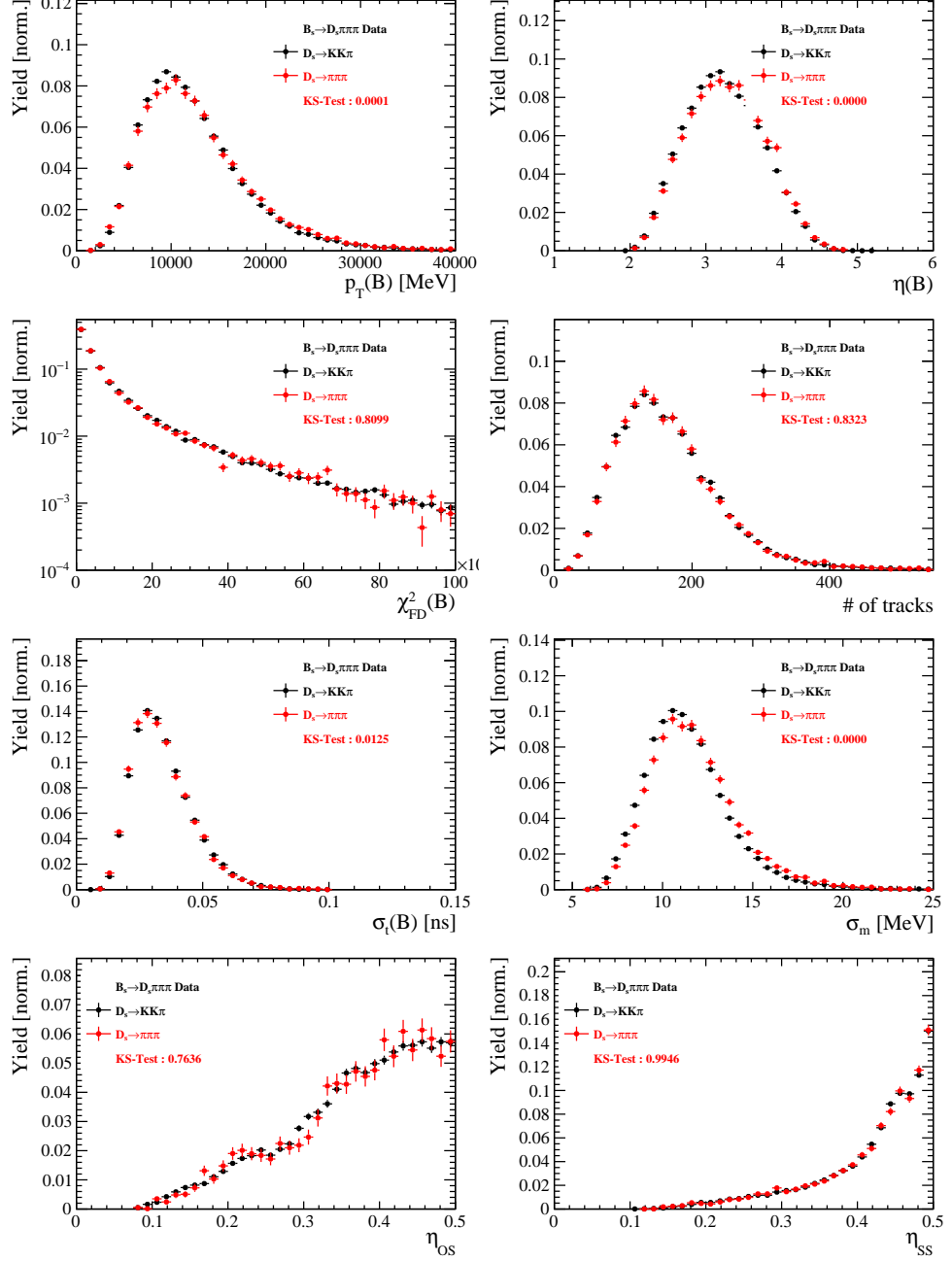


Figure C.5: Comparison of selected variables.

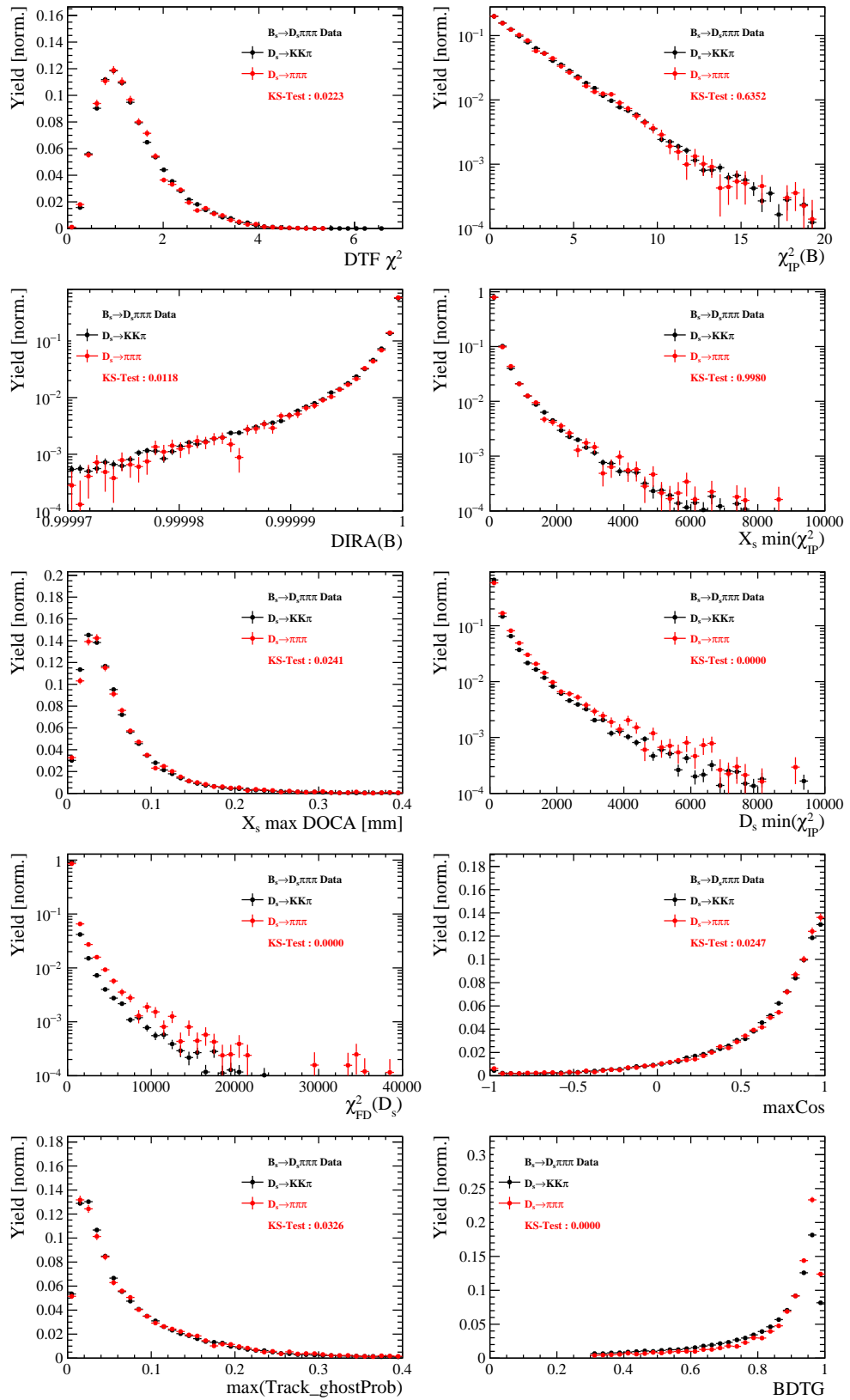


Figure C.6: Comparison of BDTG input variables and classifier response.

780 G.4 Comparison of trigger categories

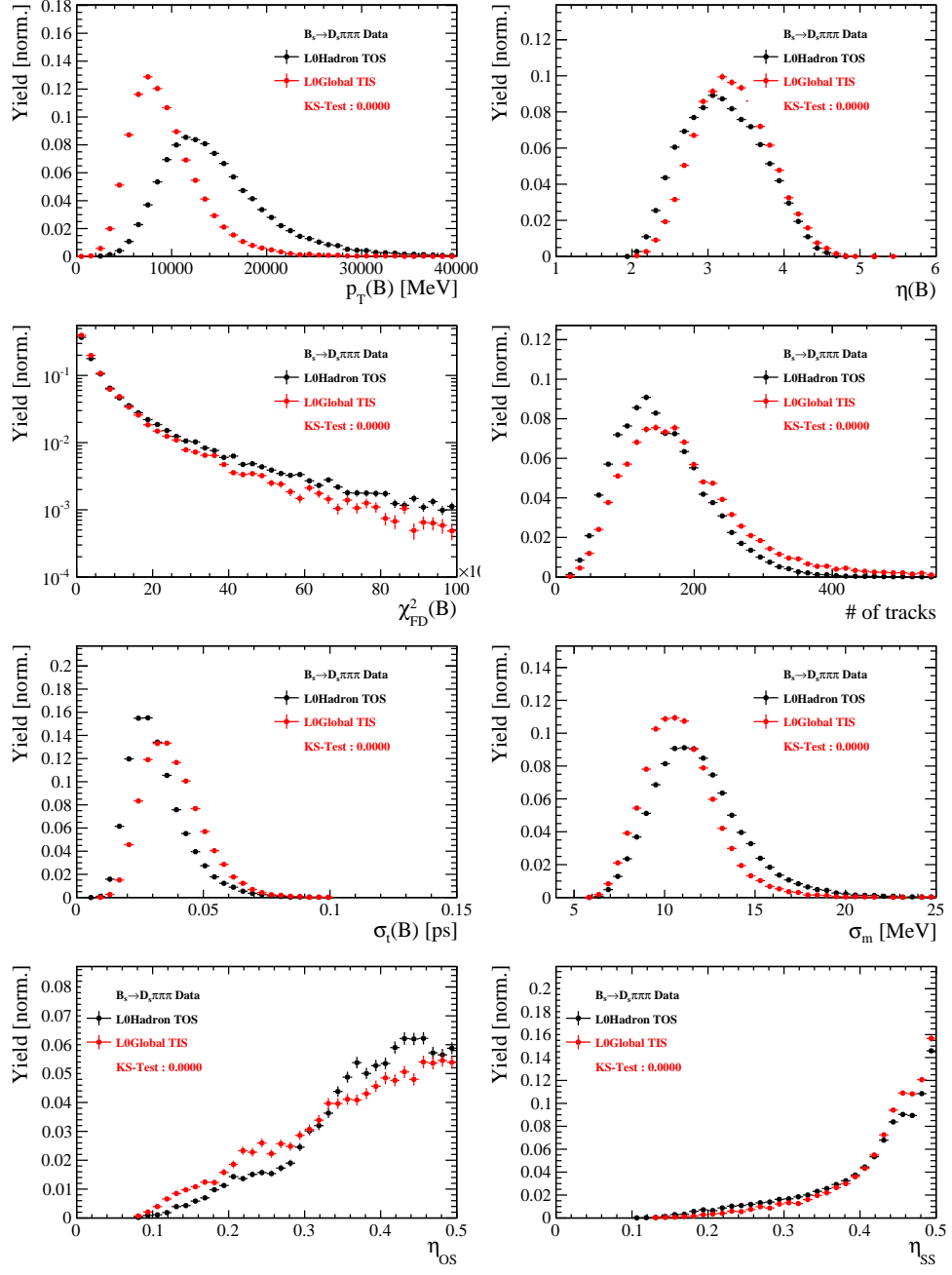


Figure C.7: Comparison of selected variables.

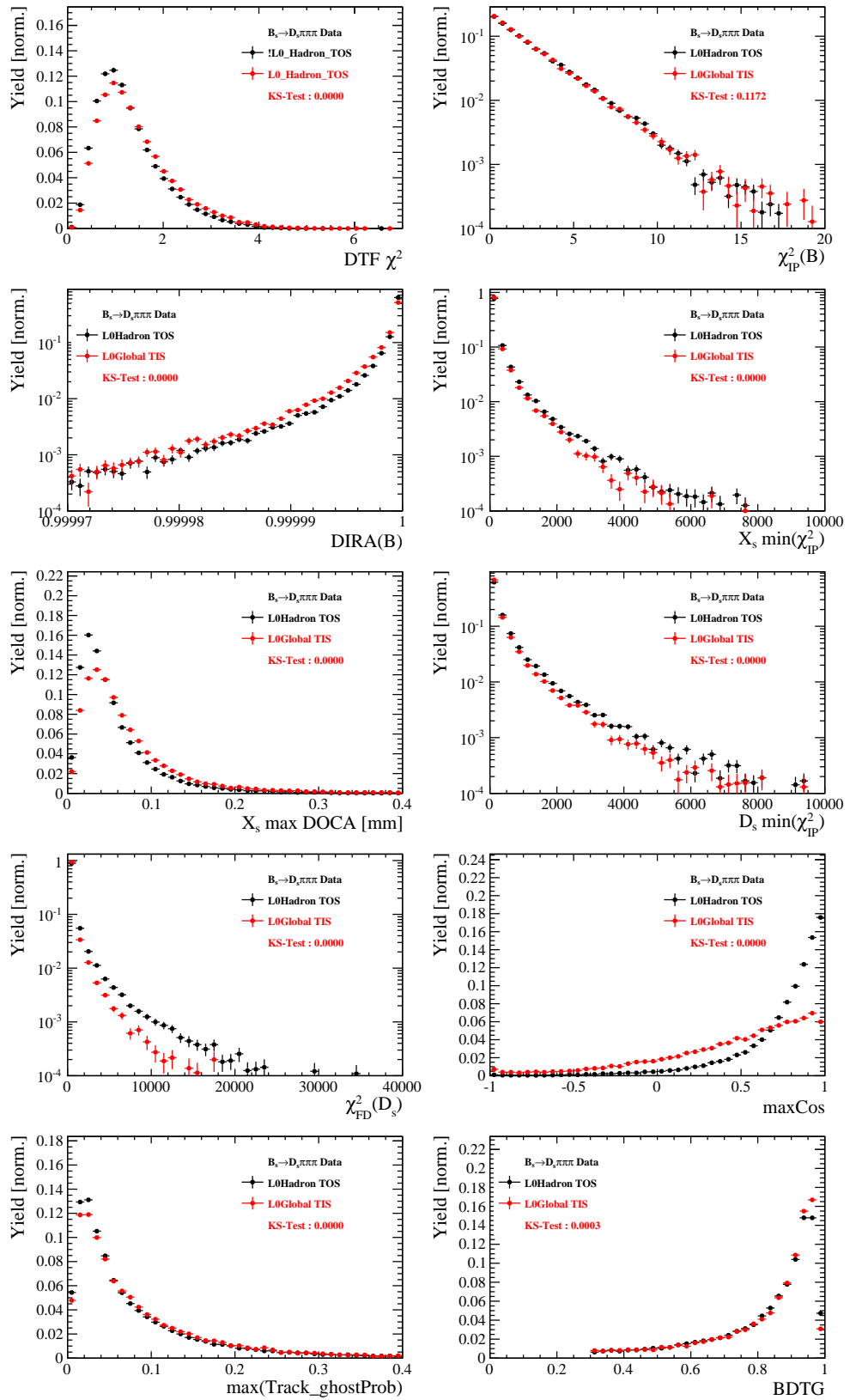


Figure C.8: Comparison of BDTG input variables and classifier response.

781 G.5 Comparison of B_s and B_d decays

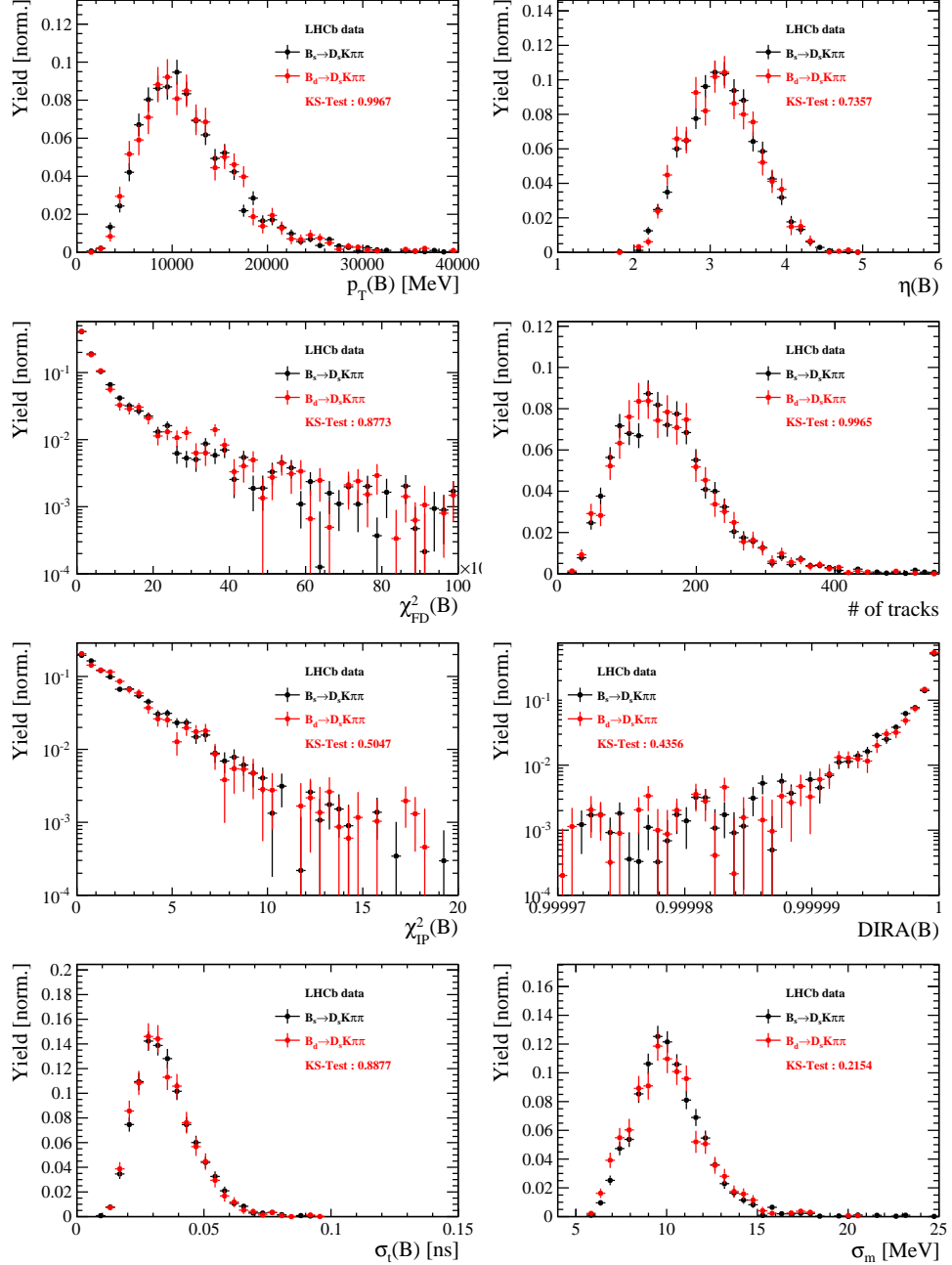


Figure C.9: Comparison of selected variables.

782 References

- 783 [1] R. Fleischer, *New strategies to obtain insights into CP violation through $B(s) \rightarrow D(s) \rightarrow K \pi$, $D(s)^* \rightarrow K \pi$, ... and $B(d) \rightarrow D \pi$, $D^* \pi$, ... decays*, Nucl. Phys. **B671** (2003) 459, [arXiv:hep-ph/0304027](#).
- 784 [2] K. De Bruyn *et al.*, *Exploring $B_s \rightarrow D_s^{(*)\pm} K^\mp$ Decays in the Presence of a Sizable Width Difference $\Delta\Gamma_s$* , Nucl. Phys. **B868** (2013) 351, [arXiv:1208.6463](#).
- 785 [3] S. Blusk, *First observations and measurements of the branching fractions for the decays $\bar{B}_s^0 \rightarrow D_s^+ K^- \pi^+ \pi^-$ and $\bar{B}^0 \rightarrow D_s^+ K^- \pi^+ \pi^-$* .
- 786 [4] LHCb, S. Blusk, *Measurement of the CP observables in $\bar{B}_s^0 \rightarrow D_s^+ K^-$ and first observation of $\bar{B}_{(s)}^0 \rightarrow D_s^+ K^- \pi^+ \pi^-$ and $\bar{B}_s^0 \rightarrow D_{s1}(2536)^+ \pi^-$* , 2012. [arXiv:1212.4180](#).
- 787 [5] M. E. Peskin and D. V. Schroeder, *An Introduction To Quantum Field Theory (Frontiers in Physics)*, Westview Press, 1995.
- 788 [6] E. Byckling and K. Kajantie, *Particle Kinematics*, John Wiley & Sons, 1973.
- 789 [7] S. Mandelstam, J. E. Paton, R. F. Peierls, and A. Q. Sarker, *Isobar approximation of production processes*, Annals of Physics **18** (1962), no. 2 198 .
- 790 [8] D. J. Herndon, P. Söding, and R. J. Cashmore, *Generalized isobar model formalism*, Phys. Rev. D **11** (1975) 3165.
- 791 [9] J. J. Brehm, *Unitarity and the isobar model: Two-body discontinuities*, Annals of Physics **108** (1977), no. 2 454 .
- 792 [10] F. von Hippel and C. Quigg, *Centrifugal-barrier effects in resonance partial decay widths, shapes, and production amplitudes*, Phys. Rev. D **5** (1972) 624.
- 793 [11] J. D. Jackson, *Remarks on the phenomenological analysis of resonances*, Il Nuovo Cimento Series 10 **34** (1964), no. 6 1644.
- 794 [12] Particle Data Group, C. Patrignani *et al.*, *Review of Particle Physics*, Chin. Phys. **C40** (2016), no. 10 100001.
- 795 [13] D. V. Bugg, *The mass of the σ pole*, Journal of Physics G Nuclear Physics **34** (2007) 151, [arXiv:hep-ph/0608081](#).
- 796 [14] G. J. Gounaris and J. J. Sakurai, *Finite-width corrections to the vector-meson-dominance prediction for $\rho \rightarrow e^+ e^-$* , Phys. Rev. Lett. **21** (1968) 244.
- 797 [15] S. M. Flatté, *Coupled-channel analysis of the $\pi\eta$ and KK systems near KK threshold*, Physics Letters B **63** (1976), no. 2 224 .
- 798 [16] BES Collaboration, M. Ablikim *et al.*, *Resonances in $J/\psi \rightarrow \phi \pi^+ \pi^-$ and $\phi K^+ K^-$* , Phys. Lett. **B607** (2005) 243, [arXiv:hep-ex/0411001](#).
- 799 [17] D. V. Bugg, *A study in depth of $f_0(1370)$* , Eur. Phys. J. **C52** (2007) 55, [arXiv:0706.1341](#).

- [18] LHCb Collaboration, R. Aaij *et al.*, *Analysis of the resonant components in $B_s \rightarrow J/\psi \pi^+ \pi^-$* , Phys. Rev. **D86** (2012) 052006, [arXiv:1204.5643](#).
- [19] C. Zemach, *Use of angular momentum tensors*, Phys. Rev. **140** (1965) B97.
- [20] W. Rarita and J. Schwinger, *On a theory of particles with half integral spin*, Phys. Rev. **60** (1941) 61.
- [21] S. U. Chung, *General formulation of covariant helicity-coupling amplitudes*, Phys. Rev. D **57** (1998) 431.
- [22] B. S. Zou and D. V. Bugg, *Covariant tensor formalism for partial wave analyses of ψ decay to mesons*, Eur. Phys. J. **A16** (2003) 537, [arXiv:hep-ph/0211457](#).
- [23] V. Filippini, A. Fontana, and A. Rotondi, *Covariant spin tensors in meson spectroscopy*, Phys. Rev. **D51** (1995) 2247.
- [24] J.-J. Zhu, *Explicit expressions of spin wave functions*, [arXiv:hep-ph/9906250](#).
- [25] P. d'Argent *et al.*, *Amplitude Analyses of $D^0 \rightarrow \pi^+ \pi^- \pi^+ \pi^-$ and $D^0 \rightarrow K^+ K^- \pi^+ \pi^-$ Decays*, JHEP **05** (2017) 143, [arXiv:1703.08505](#).
- [26] M. Williams, *Numerical Object Oriented Quantum Field Theory Calculations*, Comput. Phys. Commun. **180** (2009) 1847, [arXiv:0805.2956](#).
- [27] LHCb, R. Aaij *et al.*, *Studies of the resonance structure in $D^0 \rightarrow K^\mp \pi^\pm \pi^\pm \pi^\mp$ decays*, Submitted to: Eur. Phys. J. C (2017) [arXiv:1712.08609](#).
- [28] D. J. Lange, *The EvtGen particle decay simulation package*, Nucl. Instrum. Meth. **A462** (2001) 152.
- [29] *Gammacombo package*, 2014.
- [30] A. Hoecker *et al.*, *TMVA: Toolkit for Multivariate Data Analysis*, PoS **ACAT** (2007) 040, [arXiv:physics/0703039](#).
- [31] M. Pivk and F. R. Le Diberder, *sPlot: A statistical tool to unfold data distributions*, Nucl. Instrum. Meth. **A555** (2005) 356, [arXiv:physics/0402083](#).
- [32] N. L. Johnson, *Systems of frequency curves generated by methods of translation*, Biometrika **36** (1949), no. 1/2 149.
- [33] Particle Data Group, K. A. Olive *et al.*, *Review of Particle Physics*, Chin. Phys. **C38** (2014) 090001.
- [34] LHCb, R. Aaij *et al.*, *A new algorithm for identifying the flavour of B_s^0 mesons at LHCb*, JINST **11** (2016), no. 05 P05010, [arXiv:1602.07252](#).
- [35] LHCb collaboration, R. Aaij *et al.*, *Opposite-side flavour tagging of B mesons at the LHCb experiment*, Eur. Phys. J. **C72** (2012) 2022, [arXiv:1202.4979](#).

- [36] Heavy Flavor Averaging Group, Y. Amhis *et al.*, *Averages of b-hadron, c-hadron, and τ -lepton properties as of summer 2014*, arXiv:1412.7515, updated results and plots available at <http://www.slac.stanford.edu/xorg/hfag/>.
- [37] T. M. Karbach, G. Raven, and M. Schiller, *Decay time integrals in neutral meson mixing and their efficient evaluation*, arXiv:1407.0748.
- [38] LHCb collaboration, R. Aaij *et al.*, *LHCb detector performance*, Int. J. Mod. Phys. **A30** (2015) 1530022, arXiv:1412.6352.
- [39] LHCb, R. Aaij *et al.*, *Measurement of CP asymmetry in $B_s^0 \rightarrow D_s^\mp K^\pm$ decays*, Submitted to: JHEP (2017) arXiv:1712.07428.
- [40] H. Gordon, R. W. Lambert, J. van Tilburg, and M. Vesterinen, *A Measurement of the $K\pi$ Detection Asymmetry*, Tech. Rep. LHCb-INT-2012-027. CERN-LHCb-INT-2012-027, CERN, Geneva, Feb, 2013.
- [41] A. Davis *et al.*, *Measurement of the instrumental asymmetry for $K^-\pi^+$ -pairs at LHCb in Run 2*, Tech. Rep. LHCb-PUB-2018-004. CERN-LHCb-PUB-2018-004, CERN, Geneva, Mar, 2018.
- [42] I. I. Y. Bigi and H. Yamamoto, *Interference between Cabibbo allowed and doubly forbidden transitions in $D \rightarrow K(S), K(L) + \pi$'s decays*, Phys. Lett. **B349** (1995) 363, arXiv:hep-ph/9502238.
- [43] B. Guegan, J. Hardin, J. Stevens, and M. Williams, *Model selection for amplitude analysis*, JINST **10** (2015), no. 09 P09002, arXiv:1505.05133.
- [44] R. Tibshirani, *Regression shrinkage and selection via the Lasso*, Journal of the Royal Statistical Society, Series B **58** (1994) 267.
- [45] G. Schwarz, *Estimating the dimension of a model*, Ann. Statist. **6** (1978) 461.
- [46] H. Akaike, *A new look at the statistical model identification*, IEEE Transactions on Automatic Control **19** (1974) 716.